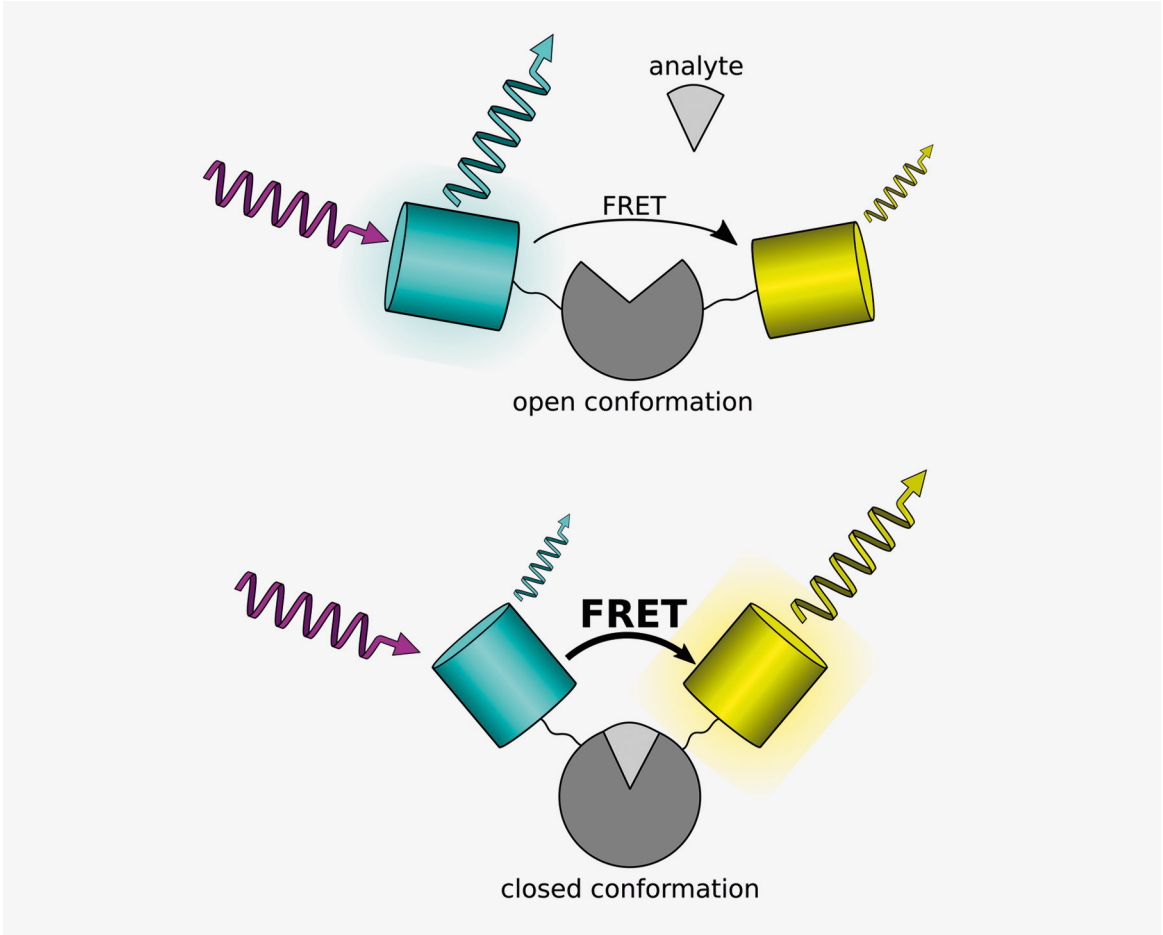

Single-Molecule Characterization of FRET-based Biosensors and Development of Two-Color Coincidence Detection

Henning Höfig

Schlüsseltechnologien / Key Technologies
Band / Volume 225
ISBN 978-3-95806-502-4

Mitglied der Helmholtz-Gemeinschaft

JÜLICH
Forschungszentrum

Single-Molecule Characterization of FRET-based Biosensors and Development of Two-Color Coincidence Detection

Von der Fakultät für Mathematik, Informatik und Naturwissenschaften der RWTH Aachen University zur Erlangung des akademischen Grades eins Doktors der Naturwissenschaften genehmigte Dissertation

vorgelegt von

Henning Höfig, M. Sc.
aus
Mönchengladbach

Berichter: Prof. Dr. Jörg Fitter
Prof. Dr. Dominik Wöll

Tag der mündlichen Prüfung: 12.05.2020

Forschungszentrum Jülich GmbH
Institut für Biologische Informationsprozesse
Zelluläre Strukturbiologie (IBI-6)

Single-Molecule Characterization of FRET-based Biosensors and Development of Two-Color Coincidence Detection

Henning Höfig

Schriften des Forschungszentrums Jülich
Reihe Schlüsseltechnologien / Key Technologies Band / Volume 225

ISSN 1866-1807 ISBN 978-3-95806-502-4

Bibliografische Information der Deutschen Nationalbibliothek.
Die Deutsche Nationalbibliothek verzeichnet diese Publikation in der
Deutschen Nationalbibliografie; detaillierte Bibliografische Daten
sind im Internet über http://dnb.d-nb.de abrufbar.

Herausgeber und Vertrieb:	Forschungszentrum Jülich GmbH Zentralbibliothek, Verlag 52425 Jülich Tel.: +49 2461 61-5368 Fax: +49 2461 61-6103 zb-publikation@fz-juelich.de www.fz-juelich.de/zb
Umschlaggestaltung:	Grafische Medien, Forschungszentrum Jülich GmbH
Druck:	Grafische Medien, Forschungszentrum Jülich GmbH
Copyright:	Forschungszentrum Jülich 2020

Schriften des Forschungszentrums Jülich
Reihe Schlüsseltechnologien / Key Technologies, Band / Volume 225

D 82 (Diss. RWTH Aachen University, 2020)

ISSN 1866-1807
ISBN 978-3-95806-502-4

Vollständig frei verfügbar über das Publikationsportal des Forschungszentrums Jülich (JuSER)
unter www.fz-juelich.de/zb/openaccess.

Eidesstattliche Erklärung

Ich, Henning Höfig, erkläre hiermit, dass diese Dissertation und die darin dargelegten Inhalte meine eigenen sind und selbstständig, als Ergebnis meiner eigenen originären Forschung, generiert wurden.

Hiermit erkläre ich an Eides statt:

1. Diese Arbeit wurde vollständig oder größtenteils in der Phase als Doktorand dieser Fakultät und Universität angefertigt;
2. Sofern irgendein Bestandteil dieser Dissertation zuvor für einen akademischen Abschluss oder eine andere Qualifikation an dieser oder einer anderen Institution verwendet wurde, wurde dies klar angezeigt;
3. Wenn immer andere eigene- oder Veröffentlichungen Dritter herangezogen wurden, wurden diese klar benannt;
4. Wenn aus anderen eigenen- oder Veröffentlichungen Dritter zitiert wurde, wurde stets die Quelle hierfür angegeben. Diese Dissertation ist vollständig meine eigene Arbeit, mit der Ausnahme solcher Zitate;
5. Alle wesentlichen Quellen von Unterstützung wurden benannt;
6. Wenn immer ein Teil dieser Dissertation auf der Zusammenarbeit mit anderen basiert, wurde von mir klar gekennzeichnet, was von anderen und was von mir selbst erarbeitet wurde;
7. Teile dieser Arbeit wurden zuvor veröffentlicht. Eine Publikationsliste ist dieser Dissertation beigefügt.

Datum: _____

Unterschrift: _____

List of Publications

Parts of this thesis were published in

- N. Kempf, C. Remes, R. Ledesch, T. Züchner, H. Höfig, I. Ritter, A. Katranidis, and J. Fitter. A Novel Method to Evaluate Ribosomal Performance in Cell-Free Protein Synthesis Systems. *Scientific Reports* **7**, 46753 (2017)

- H. Höfig, J. Otten, V. Steffen, M. Pohl, A. Boersma, and J. Fitter. Genetically Encoded Förster Resonance Energy Transfer-Based Biosensors Studied on the Single-Molecule Level. *ACS Sensors* **3**, 1462–1470 (2018)

- H. Höfig*, M. Cerminara*, I. Ritter, A. Schöne, M. Pohl, V. Steffen, J. Walter, I. Vergara Dal Pont, A. Katranidis, and J. Fitter. Single-Molecule Studies on a FRET Biosensor: Lessons from a Comparison of Fluorescent Protein Equipped versus Dye-Labeled Species. *Molecules* **23**, 3105 (2018), *equal contribution

- N. O. Junker, F. Vaghefikia, A. Albarghash, H. Höfig, D. Kempe, J. Walter, J. Otten, M. Pohl, A. Katranidis, S. Wiegand, and J. Fitter. Impact of Molecular Crowding on Translational Mobility and Conformational Properties of Biological Macromolecules. *The Journal of Physical Chemistry B* **123**, 4477–4486 (2019)

- H. Höfig, O. Yukhnovets, C. Remes, N. Kempf, A. Katranidis, D. Kempe, and J. Fitter. Brightness-Gated Two-Color Coincidence Detection Unravels Two Distinct Mechanisms in Bacterial Protein Translation Initiation. *Communications Biology* **2**, 459 (2019)

Abstract

Biomolecules often exhibit heterogeneous properties, e. g. they can exist in different conformational states. Ensemble measurements provide only averaged values and, hence, cannot resolve the underlying heterogeneity. In contrast, single-molecule techniques are based on a molecule-by-molecule analysis which allows to reveal the heterogeneity. In this work, two single-molecule methods based on the confocal detection of fluorescent biomolecules are presented.

First, genetically-encoded FRET-based biosensors are investigated that utilize Förster resonance energy transfer (FRET) between two fluorescent proteins as the sensor signal. FRET-based biosensors have great potential for applications in biotechnology or diagnostics. Yet, the development of highly-sensitive sensor constructs is complicated by the complexity of the sensor design and the limited information content of the ensemble characterization. This work presents the experimental requirements for the single-molecule detection of FRET-based biosensors followed by a comprehensive single-molecule study of a set of FRET-based biosensors for the determination of glucose concentrations. The single-molecule characterization allows to dissect different parameters that contribute to the sensor performance and, hence, facilitates a more targeted sensor design. Furthermore, the effect of macromolecular crowding on the glucose sensor and two specific crowding sensor constructs is investigated on the single-molecule level. In order to elucidate the role of the fluorescent proteins for the sensor performance, a dye-labeled analogue of the glucose biosensor is investigated on the single-molecule level. The small changes of the FRET signal upon glucose addition in comparison to the biosensor equipped with fluorescent proteins indicate the importance of the relative fluorophore orientation for the FRET signal, that is unique for the employed fluorescent proteins.

The second part of this thesis deals with two-color coincidence detection (TCCD) which enables to investigate the binding of two biomolecules that exhibit fluorescence of two different colors. Existing methods underestimate the coincidence due to an imperfect overlap of the confocal volumes of the different colors. The introduction of a brightness gating (BTCCD) for the single-molecule fluorescence intensity facilitates the selection of molecule trajectories that transverse both confocal volumes and, hence, enables quantitative analyses. The capability of the brightness gating is demonstrated by reproducing the coincidence of various, dual-labeled reference samples. After a rigorous testing of the limits of BTCCD, it is applied to FRET-based biosensors to reveal the donor-only and acceptor-only fractions. Finally, BTCCD is used to characterize protein synthesis in a cell-free protein synthesis system and to reveal a previously unrecognized mode of protein translation initiation in bacteria. The ability of BTCCD to provide quantitative results in combination with the versatility of fluorescence assays turns BTCCD into a helpful tool for further studies of the interaction of biomolecules.

Zusammenfassung

Biomoleküle zeigen oft heterogene Eigenschaften wie z. B. verschiedene Konformationszustände. Ensemblemessungen können die zugrunde liegende Heterogenität nicht auflösen, da sie nur gemittelte Werte liefern können. Im Gegensatz dazu, erlauben Einzelmolekülmessungen diese Heterogenität offenzulegen, da sie auf der Analyse von Molekül für Molekül basieren. In der vorliegenden Arbeit werden zwei Anwendungen von Einzelmolekülmessungen, die auf der Konfokaldetektion von fluoreszenzmarkierten Biomolekülen basieren, vorgestellt.

Zunächst werden genetisch kodierbare FRET-basierte Biosensoren untersucht, die als Sensorsignal den Förster-Resonanzenergietransfer (FRET) zwischen zwei Fluoreszenzproteinen ausnutzen. FRET-basierte Biosensoren zeigen ein großes Anwendungspotential in der Biotechnologie oder Diagnostik. Die Entwicklung hoch sensitiver Sensorkonstrukte wird jedoch durch das komplexe Sensordesign, sowie den begrenzten Informationsgehalt von Ensemblemessungen erschwert. In dieser Arbeit werden zunächst die experimentellen Voraussetzungen für eine Einzelmoleküldetektion von FRET-basierten Biosensoren diskutiert. Im Anschluss wird eine umfangreiche Einzelmolekülstudie einer Gruppe von Biosensoren für die Bestimmung von Glukosekonzentrationen vorgestellt. Dabei erlauben die Einzelmolekülinformationen eine detaillierte Unterscheidung verschiedener Parameter, die zusammen die Leistungsfähigkeit des jeweiligen Sensors festlegen. Diese Informationen ermöglichen nun ein zielgerichteteres Sensordesign. Des Weiteren wird der Effekt von makromolekularem Crowding auf den Glukosesensor sowie zwei spezifische Crowdingsensorkonstrukte auf dem Einzelmolekülniveau untersucht. Abschließend wird eine Einzelmolekülanalyse einer farbstoffmarkierten Nachbildung des Glukosesensors durchgeführt. Die geringe FRET-Änderung bei Glukosezugabe im Vergleich zum Sensor mit Fluoreszenzproteinen weist auf die Relevanz der relativen Fluorophororientierung bei der Entstehung des FRET-Signals hin, die nur bei Fluoreszenzproteinen auftritt.

Der zweite Teil der Arbeit behandelt die Zweifarben-Koinzidenzdetektion (TCCD). Diese ermöglicht die Untersuchung der Bindung zweier Biomoleküle, die Fluoreszenz unterschiedlicher Farbe aufweisen. Bestehende Methoden unterschätzen die Koinzidenz, da die Konfokalvolumina für die Detektion beider Farben unvollständig überlappen. Die Einführung einer Helligkeitsschwelle (BTCCD) für die Fluoreszenzintensität ermöglicht es, ausschließlich Molekültrajektorien auszuwählen, die beide Konfokalvolumina durchlaufen, was eine quantitative Koinzidenzanalyse erlaubt. Das Potential von BTCCD wird anhand der korrekten Reproduktion der Koinzidenz mehrerer, vollständig doppelt markierter Referenzproben dargelegt. Nach einer gründlichen Untersuchung der experimentellen Grenzen von BTCCD, wird die Methode zur Bestimmung der Anteile an Biosensoren, die ausschließlich einen fluoreszierenden Donor oder Akzeptor besitzen, angewendet. BTCCD wird schließlich zur Charakterisierung eines Systems zur zellfreien Proteinsynthese verwendet, sowie zum Nachweis eines zuvor unbeobachteten Initiierungsmodus der Proteintranslation in Bakterien. Die Möglichkeit der quantitativen Koinzidenzdetektion mit BTCCD sowie die Vielseitigkeit von Fluoreszenzassays machen BTCCD zu

einem hilfreichen Werkzeug für zukünftige Studien zur Untersuchen der Wechselwirkung von Biomolekülen.

Contents

List of Figures

List of Tables

List of Acronyms

APD avalanche photodiode
AV accessible volume
BTCCD brightness-gated two-color coincidence detection
CFP cyan fluorescent protein
CFPS cell-free protein synthesis
dsDNA double-stranded DNA
FCCS fluorescence cross correlation spectroscopy
FCS fluorescence correlation spectroscopy
FP fluorescent protein
FRET Förster resonance energy transfer
GFP green fluorescent protein
IPL inter-photon lag
MB molecular brightness
MglB glucose/galactose-binding protein
MDF molecular detection function
NA numerical aperture
PEG polythylene glycol
PIE pulsed interleaved excitation
SAXS small-angle X-ray scattering
SB signal-to-background ratio
smFRET single-molecule Förster resonance energy transfer
TCCD two-color coincidence detection
TCSPC time-correlated single photon counting
TTTR time tagged time-resolved
YFP yellow fluorescent protein

1 Introduction

The field of biophysics aims to gain insight into biological objects, systems, or processes by means of a quantitative description of them. The cell is the fundamental biological element and, consequently, the study of cellular objects and their interactions is crucial for the understanding of life. However, this study is complicated by the multiplicity and heterogeneity of biomolecules that exist in the cell. The typical size of biomolecules ranges from a few nanometers up to tens of nanometers.

As humans we are limited by our eyes when we want to observe tiny objects. The theoretical maximum angular resolution of the eye is 1 arc minute, however, the average human eye has an angular resolution of 4 arc minutes [1]. Taking the distance of best vision of 25 cm [2], the spatial resolution of the eye is around 0.25 mm. If we want to observe smaller object, we depend on suitable optical tools. Antoni van Leeuwenhoek (1632-1723) was one of the first who could observe that life takes also place on the microscopic level. Van Leeuwenhoek was very talented in manufacturing high-quality lenses that he used to build single-lens microscopes which offered outstanding magnifications at that time. Using his microscopes, he could observe microorganisms, like bacteria, or spermatozoa. His findings are considered to mark the birth of microbiology [3].

Nowadays, optical microscopy is no longer limited by the quality of the instrumentation but by the wave characteristics of light. Abbe's diffraction limit restricts the resolution to $d \approx \lambda/2$. The advent of super-resolution has revolutionized optical microscopy and pushed the resolution limit by a factor of ~10 [4, 5] which enables the observation of subcellular structures in astonishing details [6, 7]. There is no doubt that cellular imaging will further contribute to our understanding of biology but in some cases it is beneficial to reduce the complexity of the system under study. Cells contain a multiplicity of constituents ranging from single ions, water molecules, and numerous biomolecules to large macromolecular machineries like ribosomes and cellular organelles like the cell nucleus in eukaryotes. Distinguishing cause and effect in such a complex system is obviously not easy. One way to reduce the complexity is to built a minimal cell in a bottom-up synthetic biology approach [8, 9]. The idea behind this approach is that while trying to build a synthetic cell, one will learn which constituents are essential and how they interact. A different approach to understand the cell is to pick only a manageable amount of constituents from a real cell, e. g. a single protein or the ribosome, and investigate them outside of the cellular environment (*in vitro*). This has the advantage that the system is well-defined, relatively easy to handle and external parameters can be much better controlled and varied.

Yet, biomolecules show often heterogeneous behavior, e. g. they might be present in different (conformational) states. Observing a large ensemble of molecules will only provide average values of a certain quantity whereas the underlying distribution will be unknown. The possibility to observe single molecules can resolve this issue but not many experi-

mental techniques have the sensitivity to detect single molecules. For the investigation of biomolecules, there are mainly two methods with single-molecule sensitivity available: force-based methods like optical/magnetic tweezers and atomic force microscopy (AFM) [10, 11], and fluorescence-based techniques [12]. The value of both techniques was honored with the Nobel prize[1]. This thesis focuses on fluorescence spectroscopy due to its applicability and versatility for the investigation of biological macromolecules.

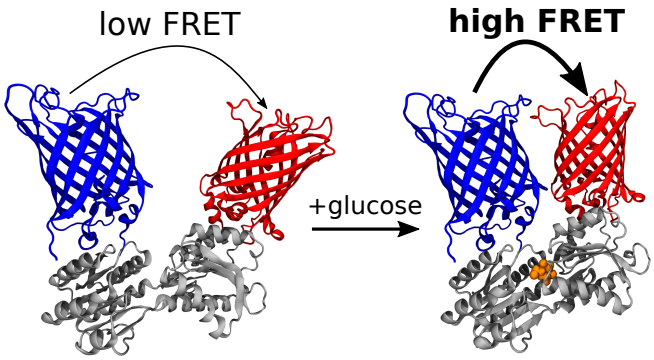

Figure 1.1: Example of FRET-based biosensor for glucose detection. Upon binding of glucose (orange), the sensing domain (gray) undergoes a conformational change. The sensor signal is the extent of Förster resonance energy transfer (FRET) between two fluorescent proteins (blue and red). Highly sensitive sensors show large differences of FRET upon glucose addition. Modified from [13].

If two fluorophores are located in close proximity, Förster resonance energy transfer (FRET) can occur between both fluorophores. The energy transfer depends strongly on the inter-fluorophore distance and allows distance measurements on the nanometer scale by doing optical spectroscopy. FRET was extensively employed on the single-molecule level which allows accurate characterization of structural and dynamical properties of biomolecules with angstrom resolution [14–18]. Besides the utilization for distance measurements, one can also employ FRET to build molecular probes that change the amount of energy transfer as a response to a (biological) stimulus. The discovery of fluorescent proteins [19] enabled to make such FRET-based biosensor even genetically encodable [20, 21]. A huge number of genetically-encoded FRET-based biosensor has been created, for example sensors that probe the redox environment [22], protein stability [23], concentration of cellular messenger molecules such as cAMP [24], calcium ions concentration [25], or glucose concentration (see Fig. 1.1). Although the motivation for making the biosensors genetically encodable was the possibility to perform live cell measurements [26, 27], it turned out that these biosensors

[1]The Nobel prize in physics 2018 was awarded to Ashkin for the optical tweezers and the Nobel prize in chemistry 2014 to Betzig, Hell and Moerner for the development of super-resolved fluorescence microscopy which was closely related to single-molecule spectroscopy.

showed remarkably high sensitivity, i. e. a large change of the energy transfer. The reason for that can be found in the nature of FRET being a dipole-dipole interaction in which the relative orientation of the dipole moments determines the coupling. In structural studies using FRET, small organic dyes in combination with flexible linkers are used which allow a fast rotational diffusion of the dyes. As a consequence, an average value for the relative orientation of the dipole moments can be used and FRET depends only on the inter-dye distance. Fluorescent proteins are rather bulky and the attachment to a sensing protein leads commonly to a restricted mobility. There have been approaches that also use long linkers for the fluorescent protein attachment in order to obtain the pure distance dependency of FRET [28]. However, this approach is not generally transferable to other biosensors and the most sensitive sensors are expected to utilize both, distance and orientation, to achieve the high FRET changes [29]. The major problem of developing highly-sensitive biosensors or increasing the sensitivity of existing ones is the lack of knowledge how the sensor design affects FRET. Although there are semirational ideas behind, sensor development is still mainly based on a trial-and-error approach [30]. The ensemble characterization of a sensor allows indeed to evaluate its performance but the limited information of ensemble measurements impede to verify the ideas that guided the sensor development.

This work reports about the implementation of single-molecule detection of genetically-encoded FRET-based biosensor. The species selectivity of single-molecule detection allows to sort out and quantify the donor-only fraction of sensor molecules. Donor-only sensors are missing a fluorescent acceptor and are thus not able to exhibit FRET which reduces the sensor signal in an ensemble measurement. Second, single-molecule characterization allows to observe the distribution of the FRET signal and can hence reveal if all sensor molecules contribute equally to the FRET change or if heterogeneity is present. The single-molecule characterization was applied to a set of glucose sensors that exhibit different linker for the attachment of the fluorescent protein to the glucose binding protein. Further, the glucose sensor and a FRET-based biosensor for the characterization of macromolecular crowding were both investigated on the single-molecules level in crowded environments. Crowding denotes the fact that the cell is filled with a high content of biological macromolecules [31, 32]. Yet, the consequences of crowding on cellular processes are poorly understood which demonstrates the need to develop tools that enable to characterize crowding *in vivo*. Single-molecule characterization has the potential to elucidate the working principles of genetically-encoded FRET-based biosensor and a better understanding of the working principles would allow a more targeted design of the sensors. The development of highly-sensitive sensors will facilitate their application in biotechnology, medicine and basic research in biology.

The ability to interact with each other is a crucial property of biomolecules because it is usually associated with a biological function, e. g. cellular signaling or assembly of higher order molecular complexes. The interaction of biomolecules, e. g. binding, can be investigated by labeling each interaction partner with a fluorophore of different color. The simultaneous occurrence of fluorescence of both colors is indicative for the presence of a complex. Existing methods like fluorescence cross correlation spectroscopy [33] or two-color coincidence detection (TCCD) [34] underestimate the fraction of dual-labeled molecules because the confocal volumes of both colors show an incomplete overlap (see Fig. 1.2). The second half of this thesis presents an improvement of TCCD that allows quantitative analysis. The

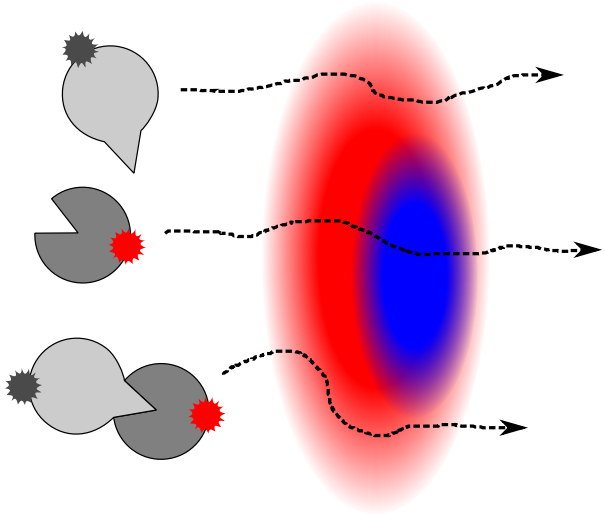

Figure 1.2: Principle of two-color coincidence detection (TCCD). The interaction of two differently labeled molecules (blue and red tags) can be probed in a single-molecule experiment as a coincidence of both fluorescence signals while the molecules diffuse through the confocal volumes. The detection probability for each color depends on the molecule trajectory due to an imperfect overlap of the confocal volumes for detection of blue and red fluorescence.

single-molecule resolution of TCCD was used to upgrade it with a simple algorithm that utilizes a brightness-gating to select only molecules that transverse both confocal volumes. The capability of this brightness-gated two-color coincidence detection (BTCCD) approach was demonstrated with various reference samples which differ in size and number of labels per molecules. After testing the limits of BTCCD and the potential bias by chance coincidences, BTCCD was applied to two biological systems. First, BTCCD was used to quantify the donor-only and acceptor-only fractions of FRET-based biosensors. Finally, the properties of ribosomes, the molecular machinery for protein synthesis, were analyzed in a cell-free protein synthesis (CFPS) system utilizing BTCCD. CFPS systems allow protein synthesis *in vitro* with a minimal set of constituents and are therefore well-suited to study protein synthesis and also cotranslational protein folding [35]. BTCCD was first used to quantify the performance of ribosomes in a CFPS system and finally revealed that a previously unnoted initiation mode of protein synthesis can potentially occur.

2 Materials and Instrumentation

2.1 Samples

2.1.1 Fluorescent Dyes

- Atto 425 NHS-Ester (ATTO-TEC, Siegen, Germany)
- Alexa Fluor® 488 NHS-Ester (ThermoFisher, Waltham, USA)
- Alexa Fluor® 647 NHS-Ester (ThermoFisher, Waltham, USA)

All dyes were dissolved in PBS buffer and stored at room temperature.

2.1.2 Fluorescent Beads

TetraSpeck Beads

Fluorescent TetraSpeck™ microspheres (ThermoFisher, Waltham, USA) with a diameter of 0.1 μm were dissolved in PBS buffer and stored at 4 °C.

Nano-Beads

The nano-bead sample was purchased from GATTAquant (Hiltpoltstein, Germany). It was custom designed based on the "GATTA-bead" which is an extremely small bead with a diameter of 23 nm produced by DNA origami technology. The nano-bead is homogeneously labeled with 5-10 dye copies of each Alexa 488 and Alexa 647. The nano-beads were dissolved in DNA buffer and stored at −20 °C.

2.1.3 DNA Oligonucleotides

The single-stranded DNA (ssDNA) oligonucleotide sequence was identical for all samples: 5'-GGA CTA GTC TAG GCG AAC GTT TAA GGC GAT CTC TGT TTA CAA CTC CGA-3'. It was dual-labeled with different dye combinations:

- 5'-modified with Alexa 488, 3'-modified with Atto 647N (IBA, Göttingen, Germany)
- 5'-modified with Alexa 488, 3'-modified with Alexa 647 (IBA, Göttingen, Germany)

The individual samples were obtained by hybridizing the respective labeled strand with the complementary unlabeled strand (Eurofins, Ebersberg, Germany) according to the protocol given in [36]. The hybridization was done with a 20 % excess of unlabeled oligonucleotide in order to ensure full hybridization of the labeled strand.

The ssDNA stocks were dissolved in TE-buffer and stored at −20 °C. The hybridized double-stranded DNA (dsDNA) was stored in DNA buffer and also stored at −20 °C.

2.1.4 FRET-Based Biosensors

The sequences and production details can be found in reference [37] for the glucose sensor constructs and in reference [38] for the crowding sensor constructs. The glucose sensors were provided by Julia Otten (Forschungszentrum Jülich) and the crowding sensor by Arnold Boersma (University of Groningen). The glucose sensor was stored in MOPS buffer and the crowding sensor in a crowding sensor buffer. All biosensor samples were aliquoted and stored in liquid nitrogen. The aliquot was unfrozen just before use and stored in a dark box on ice. After 24 h the aliquot was disposed.

2.1.5 Dye-Labeled Glucose Binding Protein MglB

The dye-labeling of the glucose binding protein MglB was realized by expression of the double-cystein mutant Q42C K137C in *E. coli* cells at ICS-5, Forschungszentrum Jülich. Details about the cloning, expression, and purification can be found in reference [13]. The purified MglB protein was labeled with maleimide-functionalized dyes Alexa 488 and Alexa 647 using a dye-to-protein excess of 1.5 and 5, respectively. More details about the labeling and subsequent purification are also given in reference [13].

2.1.6 Cell-Free Protein Synthesis System

The cell-free protein synthesis (CFPS) was based on the commercial PURE system [39] without ribosomes ('PURExpress Δ ribosomes', New England Biolabs, Ipswich, USA). In the case of the experiments that investigated stalling efficiency and activity, the ribosomes were unspecifically labeled with a 20-fold excess of Cy5-NHS-ester functionalized dye (GE Healthcare Life Science, Little Chalfont, UK). The experiments that investigated translation initiation utilized site-specific labeling of the 50S subunit by means of a Cy5-modified RNA oligonucleotide that binds to a ribosomal RNA loop [40]. The respective ribosomes and the plasmid that encoded for the fast maturating green fluorescent protein (GFP) variant Emerald (GFPem) [41] were added to the CFPS system. The C-terminus of GFPem is extended by 47 residues to enable a complete leaving of the ribosomal exit tunnel followed by a modified version of the arrest peptide SecM [42]. The syntheses were performed by Cristina Remes, Noémie Kempf, and Alexandros Katranidis. Further details about the biochemical procedures are given in reference [43].

2.2 Buffers

All buffers were prepared with ultrapure water (TKA, Niederelbert, Germany). If not stated otherwise, the chemicals were purchased in the highest purity available from Carl Roth (Karlsruhe, Germany). Magnesium chloride was added from a 1 M aqueous solution (VWR, Darmstadt, Germany). The pH was measured with a pH meter ("SevenCompact", Mettler Toledo,

Columbus, USA) that was calibrated prior to use with reference solutions of pH 4.01, 7.01, and 10.01 (Hanna Instruments, Vöhringen, Germany). After adjustment of pH with HCl or NaOH, the buffer was filtrated by vacuum soaking through a nylon membrane with 0.22 μm pore size (GVS, Sanford, USA). The following buffers were used:

TE buffer

- 10 mM TRIS (tris(hydroxymethyl)aminomethane)
- 1 mM EDTA (ethylenediaminetetraacetic acid)
- pH 7.5

PBS buffer

- 50 mM potassium phosphate
- 150 mM NaCl
- pH 7.2

DNA buffer

- 20 mM TRIS (tris(hydroxymethyl)aminomethane)
- 100 mM NaCl
- 10 mM $MgCl_2$
- pH 7.5

MOPS (glucose) buffer

- 20 mM MOPS (3-(N-morpholino)propanesulfonic acid)
- pH 7.3

For glucose-containing buffers, D(+)-glucose was added to reach a concentration of 125 mM. Lower concentrations were obtained by diluting with pure buffer whereas the highest dilution factor was ~ 1:1000. If lower concentrations were needed, a new stock solution with respective lower glucose concentrations was prepared.

Crowding sensor buffer

- 10 mM potassium phosphate
- 100 mM NaCl
- pH 7.4

Preparation of crowded solutions

Crowder solutions were obtained by dissolving PEG with molecular mass of 6,000 Da or 35,000 Da ("BioUltra" grade, Merck, Darmstadt, Germany) or Ficoll® with molecular mass of 70,000 Da (GE Healthcare, Uppsala, Sweden) in concentrations up to 20 w/w% in the respective buffer. The solutions were gently shaken for 1h on a vortex shaker. The complete dissolving of the crowding agents was checked by eye as the absence of turbidity.

Protein buffer

- 50 mM MOPS (3-(N-morpholino)propanesulfonic acid)
- 50 mM NaCl
- pH 7.4

2.2.1 Photoprotection Additives

Dye-Labeled Glucose Binding Protein

The 'protein buffer' was enriched with a photo-protection cocktail consisting of 1 mM Trolox (6-hydroxy-2,5,7,8-tetramethylchromane-2-carboxylic acid) and 10 mM cysteamine. The buffer was enriched with 0.001 % Tween®20 to prevent sticking to the glass surface.

Cell-Free Protein Synthesis System

The ribosomes were labeled and stored in a Tris-polymix buffer [40]. The oxygen scavenging system based on PCA (protocatechuic acid) and PCD (protocatechuate 3,4-dioxygenase) [44] was used for the photo-protection cocktail that contained 10 mM PCD, 2.5 mM PCA, and 1 mM Trolox.

2.3 Cover Slip Preparation

The cover slip treatment varied depending on the sample that was used. Distilled water and ultrapure solvents were used for washing the slides ("no. 1.5H", Marienfeld, Lauda-Königshofen, Germany).

- Blow cover slides with ultrapure nitrogen.

  ⟶ ready for use with free dyes

- Put droplet of isopropanol on slide, gently wipe with precision wipe, rinse with water, put droplet of acetone on slide, gently wipe, rinse with water, dry with ultrapure nitrogen.
- Put into plasma cleaner ("PDC-32G", Harrick Plasma, Ithaca, USA) for 10 min. on medium power.

  ⟶ ready for use with DNA samples

- Pipette 70 μl of Sigmacote® (Merck, Darmstadt, Germany) on cover slide, spread with pipette tip and let it dry out.
- Remove excess of Sigmacote® by subsequently, gently rinsing with isopropanol, water, acetone, water, and drying with ultrapure nitrogen.

  ⟶ ready for use with FRET-based biosensors

The experiments with ribosomes require cover slides passivated by PEG coating. The protocol for the preparation of PEG coated slides can be found in ref. [45].

2.4 List of Confocal Microscope Components

The majority of the measurements presented in this thesis were conducted on the confocal microscope "MicoTime200" (PicoQuant, Berlin, Germany). In the following, only a list of the major parts is given. The general setup of a confocal microscope is presented in Section 3.2.1. Two lasers can be used together at a time. The 481/633 nm combination is used for samples labeled with blue dyes such as Alexa 488 and red dyes, e. g. Alexa 647 or Atto 647N. The extension of the microscope with new 437/509nm nm lasers and the corresponding optical elements for the detection of FRET-based biosensors is further discussed in Section 4.9.1.

- lasers:

  437nm, "LDH-D-C-440", clean-up filter: "439/8" (Semrock, Rochester, USA)

  481nm, "LDH-D-C-485", clean-up filter: "475/28" (Semrock, Rochester, USA)

  509nm, "LDH-D-C-510", clean-up filter: "510/10" (Semrock, Rochester, USA)

  633nm, "LDH-D-C-640", clean-up filter: "z636/10x" (Chroma Technology, Vermont, USA)

- dichroic mirror (laser combining unit):

  437nm: "458-Di02" (Semrock, Rochester, USA)

  481nm: "T495lpxr" (Chroma Technology, Vermont, USA)

  509nm: "525-Di01" (Semrock, Rochester, USA)

- major dual-band dichroic mirror (main optical unit):

  437/509nm: “Di01-R442/514/561” (Semrock, Rochester, USA)

  481/633nm: “XF2401” (Omega Optical, Brattleboro, USA)

- objective:

  “UPLSAPO”, 60x, NA 1.2, water immersion (Olympus Deutschland, Hamburg, Germany), correction collar setting 0.17

- pinhole:

  diameter of 75 μm

- analyzing optical elements:

  FCS: 50/50 beam splitter (Olympus Deutschland, Hamburg, Germany)

  437/509nm: dichroic mirror “T505lpxr” (Chroma Technology, Vermont, USA)

  481/633nm: dichroic mirror “620dcxr” (Chroma Technology, Vermont, USA)

- emission band-pass filters:

  437/509nm: CFP emission filter: “ET480/40m” (Chroma Technology, Vermont, USA)

  437/509nm: YFP emission filter: “ET560/80m” (Chroma Technology, Vermont, USA)

  481/633nm: blue emission filter: “FF01 530/55” (Semrock, Rochester, USA)

  481/633nm: red emission filter: “ET658/80m” (Semrock, Rochester, USA)

- detectors:

  detector 1: single-photon avalanche diodes “τ-SPAD” (PicoQuant, Berlin, Germany)

  detector 2: single-photon counting module “COUNT-T100” (Laser Components, Olching, Germany)

- electronics:

  laser driver “PDL-828 Sepia II” (PicoQuant, Berlin, Germany)

  time-correlated single-photon counting module “PicoHarp300” (PicoQuant, Berlin, Germany)

2.5 Spectrometers

- absorption spectrometer “UV-2600”, Shimadzu (Kyoto, Japan)

  cuvette: 104F-QS, 10x4 mm (Hellma, Mühlheim, Germany)

- fluorescence spectrometer “QuantaMaster40” (PTI, Birmingham, USA)

  cuvette: 105-253-QS, 10x2 mm (Hellma, Mühlheim, Germany)

2.6 Software

- control of confocal microscope, FCS analysis: “SymPhoTime 64”, version 2.4 (PicoQuant, Berlin, Germany)
- smFRET, BTCCD, and further data analysis: self-written routines in “MATLAB R2015b” (Mathworks, Natick, USA)
- data fitting: “FMINUIT” package for MATLAB [46]
- AV calculation: modified C-code provided by S. Poblete [36]
- molecular modeling and representation: “VMD” [47]
- data processing, data fitting, and data representation: “OriginPro 9.0.0G” (OriginLab, Northampton, USA)

3 Theory and Methods

3.1 Fluorescence

Fluorescence has nowadays become one of the key techniques in the life sciences. Besides tremendous improvements of the instrumentation, the reason for this advancement can be probably found in the three "s" of fluorescence: specificity, selectivity, and most important sensitivity [48]. The scope of the following Section 3.1.1 is to elucidate this properties by briefly summarizing the principles of fluorescence while Section 3.1.2 illustrates the situation of energy transfer between fluorophores. Finally, Section 3.1.3 introduces fluorescent proteins, a special class of fluorescent biomolecules and the main constituents of FRET-based biosensors.

3.1.1 Principles

The emission of light of specific wavelength after a substance absorbed light of a shorter but also specific wavelength is named photoluminescence. Depending on the energy levels that are involved, photoluminescence is divided into fluorescence and phosphorescence [49]. Only fluorescence is of practical relevance for the investigation of biomolecules because most biomolecules do not show remarkable phosphorescence. Yet, which materials do actually show fluorescence and which material properties lead to the appearance of fluorescence?

The occurrence of fluorescence is based on the interaction of delocalized electrons with light, usually in the visible spectral range. These delocalized electrons can be found e. g. in molecules that have conjugated π-bonds. A single bond is only formed by σ-bonds but double and triple bonds use additionally π-bonds. Hence, a repeating sequence of single and double bonds leads to a delocalized molecular orbital for the electrons. This bond configuration has also been termed "resonant" because the bonds cannot be associated to one atom pair but "switch" continuously. A simple example is a benzene ring that consists of six carbon atoms and three conjugated π-bonds [50]. The absorption of a light quanta with matching energy will lead to a transition of the delocalized electron system from the HOMO, the singlet ground state S_0, into the LUMO, the first excited singlet state S_1.
Conjugated π-bonds are common in organic compounds, e. g. in polyenes (linear carbon chains) or polyaromatic compounds (ring structures). Hence, fluorescence is also a common phenomenon in several (bio)molecules.

Next, one has to think about an adequate framework to describe fluorescence. Since we consider the interaction of light quanta with electrons, only a quantum mechanical description is sufficient to fully describe the system, which is beyond the scope of this thesis. However, simplified models are often sufficient and can already provide useful insights. For example, one can treat the delocalized π–electron as completely free in the molecular orbital

and also as non-interacting [51]. The resulting "particle in a box" problem can be solved straightforward. As a results one can calculate the electrons' energy levels. The model also explains that red fluorophores are usually larger than blue fluorophores because the delocalized electron system is spatially more extended. A further description of fluorescence can be done by a semi-classical model in which the fluorophore is treated as an oscillating electric dipole interacting with electromagnetic waves [52]. This model reasonably describes e. g. the impact of the fluorophore's dielectric environment on the emission properties or the distance dependence of the energy transfer between two fluorophores in the near-field.

In the following, the characteristics of fluorescence are consequently presented in a phenomenological fashion. A full quantum mechanical description is omitted. Instead, the fluorophores are treated predominantly as electric dipoles but having in mind that the interpretation needs to be quantum mechanical, i. e. single photons are absorbed/emitted.
The phenomenons are described for common fluorophores. Exceptions are rare but do exist in rather special systems.

Jablonski Diagram

An extremely helpful tool to visualize the different characteristics of fluorescence is to draw the involved energy levels of the electron system. Such an energy level diagram is referred to as a Jablonski diagram and is depicted in Figure 3.1. At room temperature the electron system is in the lowest vibrational state of the electronic ground state, the singlet state S_0. The thermal energy is usually not sufficient to excite higher vibrational modes. After the absorption of a photon with suitable energy, the electron system is transferred to an excited electronic singlet state ($S_1, S_2, ...$). Since each electronic state splits off in multiple vibrational states, the excitation can occur in each of these vibrational states. The electron system is predominantly excited in higher vibrational states because theses states are more compatible with the current nuclear coordinates (Franck-Condon principle). If the system is excited to an electronic state higher than S_1, it relaxes to a higher vibrational state of S_1 by internal conversion on time scales of $10^{-14} - 10^{-10}$ s [51]. From there, the system can undergo a vibrational relaxation to the the vibrational ground state of S_1 on similar time scales of $10^{-12} - 10^{-10}$ s [51]. The energy difference is dissipated as heat. From S_1 the system can relax to S_0 accompanied with the emission of a fluorescence photon or it decays radiationless again by internal conversion. Alternative to the $S_1 \longrightarrow S_0$ transition, the electron can do a spin flip which results in a triplet state T_1. The process is termed intersystem crossing and is in principle quantum mechanically forbidden which results in smaller transition rates of $10^5 - 10^8\ s^{-1}$ [51]. If the transition back to S_0 is associated with a photon emission, the process is called phosphorescence. Yet, the yield of phosphorescence is very low because the forbidden spin flip results in low rates ($10^{-2} - 10^3\ s^{-1}$) that compete with the reverse intersystem crossing $T_1 \longrightarrow S_0$.
In the following, each process is shortly summarized.

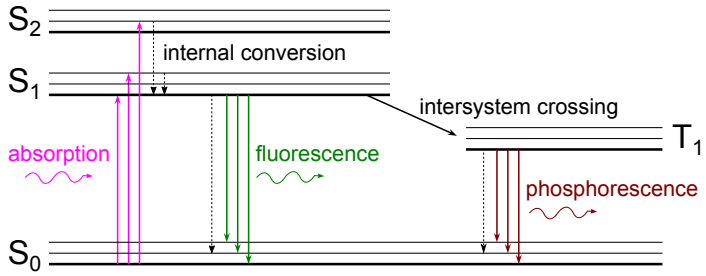

Figure 3.1: Jablonski diagram depicting the energy levels of the electron system.

Absorption

The absorption of light by a substance is the prerequisite for the occurrence of fluorescence. The ability to absorb a photon of certain energy depends on the nature of the wave functions of the ground state and the excited state ψ_G and ψ_E, respectively. The absorption process is described by the transition dipole moment [51]

$$\mu_{GE} = \int \psi_G \, \mu \, \psi_E \, dv \,, \tag{3.1}$$

where μ is the dipole operator and dv denotes the volume element.
The dipole strength

$$D_{GE} = |\mu_{GE}|^2 \tag{3.2}$$

characterizes the absolute amount of the transition.

The transition time for the absorption process is ~ 10^{-15} s [53]. Vibrations occur on much slower time scales and, hence, the nuclear coordinates can be considered as static during absorption. The excited electron system is even more delocalized which results in an increase of the bond length. As a consequence, the electron system is excited to higher vibrational states because they provide a larger overlap with the wave function of S_0 (Franck-Condon principle).

Experimentally, one can measure the absorption by the intensity reduction of light that travels through a solution of absorbing molecules. If one sends light of intensity I_0 through a cuvette of path length l that is aligned along x, it will steadily decrease in intensity. Further, the absorption strength will depend linearly on the concentration of absorbers c. Hence, the fractional intensity decrease in a small path element dx is [51]

$$\frac{dI}{I} = -\alpha \, c \, dx \,, \tag{3.3}$$

where α is the proportionality constant.
Integration yields

$$I = I_0 \, e^{-\alpha \, c \, l} \,, \tag{3.4}$$

which is known as the Lambert-Beer law but commonly rather used with base 10:

$$I = I_0\, 10^{-\epsilon\, c\, d} = I_0\, 10^{-OD}, \tag{3.5}$$

where $\epsilon = 0.434\,\alpha$ is the molar absorption coefficient given in $M^{-1}cm^{-1}$, c in M, and l in cm. OD is referred to as optical density or also absorbance.
The wavelength dependency of the molar absorption coefficient ϵ is denoted an absorption spectrum and can be measured with a double-beam absorption spectrometer where the incident beam of monochromatic light is equally split. The reference beam is sent to a cuvette that is identical to the sample cuvette but which contains only the solvent. The measured transmitted intensity of the reference cuvette serves as I_0 in Equation 3.5. This setup avoids inaccuracies due to scattering at the cuvette interfaces. The wavelength dependency of the optical density is obtained by measuring I while scanning the wavelength of the incident light. A typical absorption spectrum is shown in Figure 3.2. One can see that it does not show distinct peaks but a rather broad spectrum. This originates from the manifold of vibrational and rotational levels that can be excited, which results in this quasi-continuum.

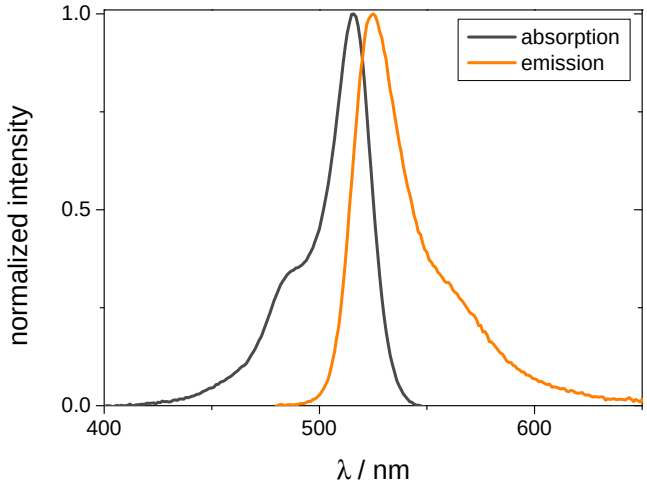

Figure 3.2: Absorption and fluorescence emission spectra of yellow fluorescent protein variant Venus.

In practice, the absorbance is often used to calculate the concentration of the absorbers if the path length l and the molar absorption coefficient at the maximum ϵ_{max} is known. The knowledge of the shape of the absorption spectrum is also needed to select an adequate excitation wavelength for further measurements and to calculate emission-absorption spectral overlaps that are relevant for energy transfer between fluorophores (see Sec. 3.1.2).

Emission

A fluorescence photon can be emitted when the electron system relaxes from S_1 to S_0. Typical time scales for fluorescence are ~ 10^{-7} – 10^{-9} s which is slow compared to the time scale of vibrational relaxation to S_1. Hence, fluorescence will usually occur when the electron system relaxes from the vibrational ground state of S_1. As a consequence, the emission spectrum is independent of the excitation wavelength known as Kasha's rule [54]. If the electron system is excited to higher vibrational states of S_1 or even to S_2, the excess energy is simply dissipated as heat.

The emission spectrum is approximately a mirror image of the absorption spectrum (see Fig. 3.2) because (1) absorption and fluorescence emission take predominantly place from the vibrational ground states of S_0 and S_1, respectively, and (2) the density of vibrational states is similar for S_0 and S_1. As a consequence, fluorescence is shifted to larger wavelengths compared to the absorbed light, known as the Stokes shift. The Stokes shift is one of the key benefits of fluorescence because it allows in practice to spectrally separate the excitation light from the emission light. This results in a low background which is a requirement for single-molecule sensitivity.

Quantum Yield

The fluorescence quantum yield is defined as

$$\Phi = \frac{N_f}{N_{abs}}, \tag{3.6}$$

where N_f and N_{abs} are the numbers of fluorescence and absorbed photons, respectively. Hence, the quantum yield quantifies how efficient absorbed photons are converted into fluorescence photons. An alternative definition of the quantum yield uses the rate of the radiative (fluorescence) transition k_f which compete with the sum of all non-radiative rates k_{nr} that lead to a $S_1 \longrightarrow S_0$ transition:

$$\Phi = \frac{k_f}{k_f + k_{nr}}. \tag{3.7}$$

Typical quantum yields spread, depending on the fluorophore, between a few 10 % up to almost 100 % [49].

Lifetime

The time delay between the absorption of a photon and the occurrence of the fluorescence photon is called fluorescence lifetime. As already discussed, the time scales of internal conversion and vibrational relaxation are fast compared to the time scale for fluorescence. Hence, the fluorescence lifetime is dominated by the time the electron system resides in S_1 before it decays to S_0. Besides the emission spectrum, the fluorescence lifetime is very sensitive to changes of the local environment of the fluorophore.

The fluorescence lifetime can be either measured in the frequency or in the intensity domain. In the frequency domain, the fluorophore is excited with light that is periodically varied

in intensity, e. g. following a sine. The emission intensity is also a sine but shows a reduced amplitude and a phase shift with respect to the excitation which can be use to extract the fluorescence lifetime [55]. However, the direct measurement of the decay in the intensity domain by time-correlated single photon counting (see Sec. 3.2.3) is nowadays the method of choice because it can also be employed to single-molecule measurements. The intensity decay of emitted fluorescence upon excitation with a short laser pulse can be described by

$$I(t) = I_0 \cdot e^{-t/\tau}, \tag{3.8}$$

where I_0 is the initial fluorescence intensity directly after the excitation and τ is the fluorescence lifetime, the time after which the intensity dropped to $1/e$ of the initial value.

One has to be aware that the fluorescence lifetime sets an upper limit for the study of dynamical properties [56]. This can be easily understood because an interaction needs to take place or change its magnitude during the lifetime to cause a change of the fluorescence properties. In single-molecule detection one can practically extend this time limit to the observation time of single molecules.

Anisotropy

Fluorescent molecules that are freely diffusing in solution are randomly oriented. Yet, if a fluorophore is excited by polarized light, e. g. emitted by a laser, dipole moments are preferentially excited that are aligned parallel to the polarization of the excitation light which is called photo selection. This causes also the emission light to be polarized. This polarization drops over time because the molecules, and hence also the dipole moments, re-orient by rotations. In a time-resolved experiment one often uses, instead of polarization, the anisotropy defined by

$$r(t) = \frac{I_\parallel - I_\perp}{I_\parallel + 2I_\perp}, \tag{3.9}$$

where $I_\parallel$ and $I_\perp$ are the intensity decays measured parallel and perpendicular with respect to the excitation polarization, respectively.
For a spherical molecule the anisotropy decay can be described by a mono-exponential model

$$r(t) = r_0 \cdot e^{-t/\phi_r}, \tag{3.10}$$

where r_0 is the fundamental anisotropy and ϕ_r is the rotational correlation time.
r_0 is determined by the photo selection and the relative orientation of the absorption and emission dipole moment. The maximum of $r_0 = 0.4$ is reached for a collinear alignment of them. ϕ_r is the characteristic time scale for rotation of the fluorophore and can be used to investigate the rotational mobility of the molecule, also to calculate the size and shape of the rotating object [57].

Photostability

Photostability is a crucial parameter, particularly for single-molecule measurements. The higher the photostability, the more often a fluorophore can undergo the absorption-emission

cycle. For fixed rate constants, the photostability is, hence, determining the total observation time of a single fluorophore. Typical values for capable dyes are 10^5 – 10^7 photons/molecule [58], whereas fluorescent proteins can only reach 10^4 – 10^5 photons/molecule [59].

Photodestruction describes the loss of the ability of the electron system to absorb light and emit fluorescence. Photodestruction can either be caused by ionization due to reabsorption of a photon while the electron system is still in the S_1 or T_1 state, or by reaction with free radicals, e. g. oxygen, which is also more likely to appear if the electron system is in an excited state. Common photoprotection additives persue therefore a dual strategy. First, an oxygen scavenger is used to reduce the molecular oxygen in solution and, second, a triplet quencher is added which depopulates the triplet state [60]. As a side effect, the depopulation of the triplet state leads also to a more stable and brighter fluorescence signal.

3.1.2 Förster Resonance Energy Transfer (FRET)

If a fluorophore is placed in the vicinity of a second, excited fluorophore, the excited state energy can be transferred from one fluorophore to the other. In this process, the excited fluorophore is named donor as it donates the energy. The other fluorophore that accepts the energy is consequently called acceptor. As a second prerequisite for energy transfer, the donor's emission spectrum needs to have a considerable spectral overlap with the acceptor' absorption spectrum. Only in this case, the energies match or in other words: they are in resonance. The energy transfer is, however, not related to emission of a photon and a subsequent re-absorption but it is a radiationless dipole-dipole coupling in the near field. The energy transfer process is called FRET because Theodor Förster developed the framework to quantitatively describe the process in 1948 [61].

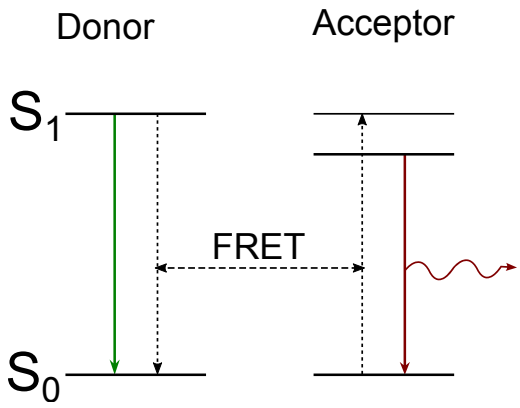

Figure 3.3: Simplified Jablonski diagram in the presence of FRET.

The transfer efficiency E characterizes which fraction of the excited donors transfer their energy. The distance dependency of the transfer efficiency is given by

$$E(R) = \frac{1}{1 + \left(R/R_0\right)^6}, \tag{3.11}$$

where R is the distance between donor and acceptor and R_0 is the so-called Förster radius, i. e. the distance at which the transfer efficiency is 50 %.
The remarkably strong distance dependency with the 6th power originates from the fact that the electric field of a dipole drops $\propto R^{-3}$. The probability to excite the acceptor depends on the power which is in turn proportional to the square of the electric field which results in the R^{-6} dependency for FRET. Another consequence of Equation 3.11 is that E(R) is most sensitive to distance changes around R_0. Beyond $R_0 \pm 0.5R_0$ the distance dependency is lost because the transfer efficiency is practically 0 and 1, respectively.
The Förster radius is given by

$$R_0[\text{Å}] = 0.211 \left(\kappa^2 n^{-4} \phi_D J(\lambda)\right)^{1/6}. \tag{3.12}$$

It depends on the relative orientation of the donor's and acceptor's dipole moments which is combined in the orientation factor κ, on the refractive index n of the surrounding medium, on the donor quantum yield ϕ_D, and on the overlap integral $J(\lambda)$ of donor emission and acceptor absorption spectra given in $[M^{-1}cm^{-1}nm^4]$.
The orientation factor is given by

$$\kappa^2 = (cos\theta_T - 3\, cos\theta_D\, cos\theta_A)^2 = (sin\theta_D sin\theta_A cos\phi - 2\, cos\theta_D\, cos\theta_A)^2, \tag{3.13}$$

where the angles are given in Figure 3.4.
The range of κ^2 reaches from 4 for a collinear arrangement over 1 for a parallel orientation to 0 for a perpendicular orientation. The Förster radius changes accordingly which in turn changes the transfer efficiency. Hence, it is also possible to observe a change in FRET which is related at least partially to a change of κ^2. In order to judge the impact of orientation on a FRET experiment, one has to compare the donor's excited state lifetime to the time scale for reorientations, i. e. the rotational correlation time (see Eq. 3.10). If all possible orientations are sampled one can calculated a mean value for κ^2 (isotropic averaging) that depends on the time regime. If the donor and/or the acceptor rotate much faster than the donor lifetime, one can apply a dynamic averaging. In contrast, if the rotation is much slower than the donor lifetime, one can do a static averaging over all orientations. In theses cases the average orientation factors are

$$< \kappa^2 >_{dyn} = 2/3 \qquad < \kappa^2 >_{stat} = 0.476, \tag{3.14}$$

where the indices denote dynamic and static averaging, respectively [62].
In two situations it is not possible to specify an average value for κ^2. First, if the rotational correlation time is on a similar time scale as the donor's fluorescence lifetime and, second, if the rotation is restricted irrespective of the time regime. Possible reasons for a restricted

rotation are too short linkers for external dye labeling or the usage of bulky fluorophores such as fluorescent proteins. Both cases can lead to a steric hindrance of rotations. In general, one can also state that the more the rotation is restricted the more the orientations matter.

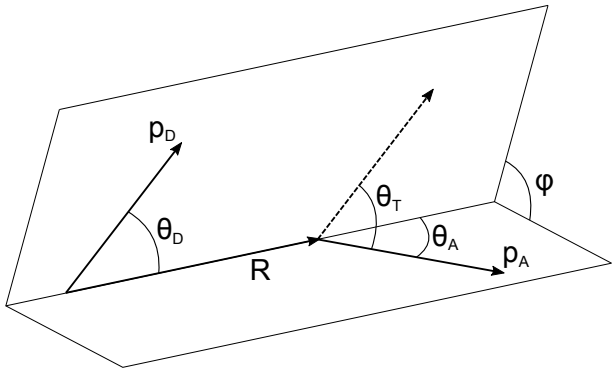

Figure 3.4: Orientational dependency of FRET.

Experimentally, there are two ways to measure FRET: intensity based and lifetime based. Using intensities, one can either consider the reduction of the donor intensity I_D with respect to the donor intensity in absence of the acceptor I_{D0}, where

$$E = 1 - \frac{I_D}{I_{D0}}, \tag{3.15}$$

or one can utilize the donor intensity I_D and acceptor intensity I_A upon donor excitation:

$$E = \frac{I_A}{I_A + \gamma I_D}, \tag{3.16}$$

where

$$\gamma = \frac{g_A}{g_D}\frac{\Phi_A}{\Phi_D} \tag{3.17}$$

is the ratio of donor and acceptor detection efficiencies g_D, g_A and quantum yields Φ_D, Φ_A, respectively.
The lifetime approach relates the donor lifetimes in presence τ_D and in absence of the acceptor τ_{D0} according to

$$E = 1 - \frac{\tau_D}{\tau_{D0}}. \tag{3.18}$$

In summary, if small organic dyes in combination with long linkers are used as a FRET pair, their rotation is free and fast and the dynamic averaging can be applied. By eliminating the orientation dependency, FRET turns into a spectroscopic ruler [63] with angstrom precision. In combination with single-molecule detection, FRET has proven to be an extremely helpful tool for structural and dynamical studies of biomolecules [17].

One step further one can exploit the orientation dependency of FRET instead of ignoring it. If donor and acceptor fluorophores have a restricted orientational mobility, reorientations will lead to a change in FRET. This enables to increase differences in FRET in a system that is not able to perform large scale structural changes.

3.1.3 Fluorescent Proteins

One can generally distinguish fluorescence in intrinsic and extrinsic. A biomolecule of interest can be labeled with an extrinsic, fluorescent probe. This probe acts as a reporter about the properties of the biomolecule it is attached to. The fluorescent probe can be equipped with various reactive groups which results either in a unspecific labeling of the target molecule or the probe can be specifically attached at a certain position. For single-molecule studies, this external dye-labeling of the biomolecule is often necessary due to the superiority of dyes in terms of brightness and photostability.

If the unmodified biomolecule shows fluorescence by itself, this can be regarded as intrinsic fluorescence. Common examples are the amino acids tryptophan and tyrosine. Another class of biomolecules that are intrinsically fluorescent are fluorescent proteins.
The history of fluorescent proteins began with the discovery of the green fluorescent protein (GFP) in the jelly fish *Aequorea victoria* by Shimomura et al. in 1962 [64]. Interestingly, GFP was mainly a protein that complicated the purification of aequorin, the protein Shimomura et al. were actually interested in. In the next 30 years GFP did not attract much of researchers' attention. This changed all of a sudden when the GFP gene was first cloned in 1992 [65]. The labeling of a target protein could now be genetically encoded. The detection of the green fluorescence of GFP with optical microscopy enabled imaging and tracking of the target molecule in live cells. A whole avalanche of applications was triggered including the development of different color variants ranging from blue to red, and the construction of genetically encoded FRET-based biosensors. Consequently, the Nobel prize in chemistry was awarded in 2008 for the discovery and developments of GFP [66].

The term "fluorescent protein" is used for the whole family of derivatives of GFP. The field of fluorescent proteins and their applications is very broad and diverse [19]. Therefore, only the main feature, i. e. the relation between the structure and the occurrence of fluorescence is discussed in the following. In Figure 3.5 a yellow fluorescent protein variant is depicted as a representative for fluorescent proteins in general. It shows the typical barrel structure built by 11 β-sheets. The special characteristic of fluorescent proteins is the ability to form a chromophore without external cofactors. For the wild type GFP this is based on a multi-step reaction between three neighboring amino acids that form the chromophore [67]. Only if these reactions succeed, GFP becomes fluorescent. This process of chromophore formation is named maturation and its efficiency depends on various external parameters [68]. The different color variants were achieved by mutation of the amino acids involved in chromophore maturation or by mutation of neighboring amino acids which will change the local environment and therefore also the fluorescence properties [69]. One property of the chromophore is crucial and preserved throughout all variants: It is buried inside the β-barrel. This shields it at least partially against external changes of the environment. Moreover, it leads to a fixed orientation of the fluorophore relative to the fluorescent protein.

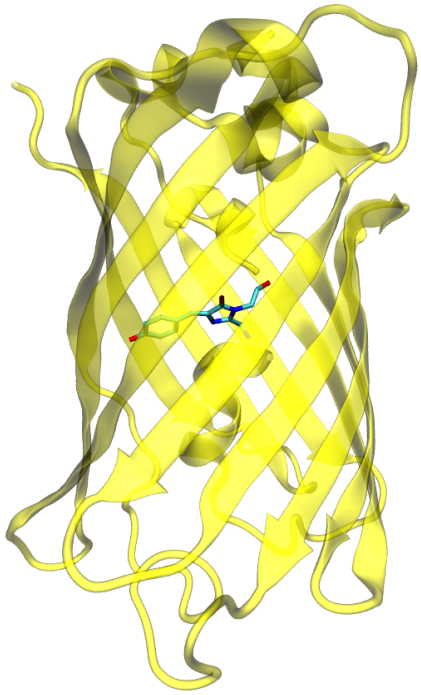

Figure 3.5: Yellow fluorescent protein variant Venus (pdb entry: 1myw) displayed in secondary structure representation. Chromophore is located inside the β-barrel structure and displayed in stick representation.

3.2 Confocal Microscopy

The original motivation for confocal microscopy was based on the limited axial resolution of conventional widefield fluorescence microscopy. In widefield microscopy, a large area of the sample is homogeneously illuminated by the excitation light. Assuming that the intensity of the excitation light is not remarkably decreased by the sample, fluorescence is excited throughout the sample. As a consequence, the out-of-focus fluorescence light led to blurred images in widefield microscopy [70]. The simple solution to increase the image contrast was to only allow in-focus light to reach the detector by placing a pinhole in the focus of the image plane. The resulting scanning confocal images impress with sharp, detailed images in comparison to the widefield image of the same sample.

However, the three-dimensional spatial confinement of detection can also be exploited to perform spectroscopy of fluorescent molecules that are freely diffusing in an aqueous solution. The size of the corresponding confocal volume is on the order of $1\,\mathrm{fl} = 10^{-15}\,\mathrm{l}$ which allows, depending on the sample concentration, the observation a few molecules down to single molecules.

This section will first cover the principles of confocal microscopy in Section 3.2.1 before the optical and electronic detection are subject of Section 3.2.2 and 3.2.3, respectively. Section 3.2.4 deals with the alternation of lasers in dual-excitation experiments. Fluorescence correlation spectroscopy, a powerful analysis tool in diffusion-based confocal microscopy, is introduced in Section 3.2.5. Finally, the benefits and the implementation of single-molecule detection are topic of the next Section 3.3.

3.2.1 Setup

A schematic sketch of a confocal microscope is shown in Figure 3.6. The light sources in confocal microscopy are usually lasers because they provide monochromatic light of sufficient intensity and a radial symmetric intensity distribution (see Sec. 3.2.2). If desired, multiple lasers of different wavelengths can be brought on the same optical axis with the help of dichroic mirrors.
In the following, the light propagation is considered by means of geometrical optics and assuming perfect optical elements (no aberrations). The excitation light is reflected by the major dichroic mirror and reaches the back focal plane of the objective. The objective focuses the beam into an aqueous droplet that contains the fluorescent sample molecules and is placed on a cover slip. The fluorophores partially absorb the light and eventually re-emit fluorescence light. Assuming a low anisotropy of the fluorescence emission, the spatial distribution of emission is isotropic and, hence, the same objective can be used to collect the light. Using this so-called epi mode minimizes also the amount of backscattered light in the detection path. The half angle θ of the cone of light collection is determined by the numerical aperture (NA) of the objective and the refractive index n of the immersion medium by:

$$sin(\theta) = \frac{NA}{n} \tag{3.19}$$

For single-molecule detection, it is essential to collect as much of the fluorescence emission of a single emitter as possible in order to reach a sufficient signal-to-background ratio (see Sec. 3.3.2). From Equation 3.19 it can be seen that large θ require a high NA that is solely provided by water or oil immersion objectives.
The objective transforms the collected light from the focal point back into parallel light in the image space. The collected light, consisting of fluorescence and scattered light, hits again the major dichroic mirror which transmits only the fluorescence because it is Stokes-shifted. A tube lens focuses the beam onto the pinhole. Light that did not arise from the focus of the objective is blocked by the pinhole because it is not parallel after passing the objective and, hence, it is not focused by the lens onto the pinhole. The light that passed the pinhole is made parallel again by a second lens and sent to an optical element dedicated to the actual analysis that should be performed. If two fluorophores are used simultaneously, this is typically another dichroic mirror that separates their emission. The detector choice depends on the requirements of the actual application. For single-molecule investigations, the detection efficiency is crucial. Here, avalanche photodiodes (APDs) are the detectors of choice as they offer high quantum yields up to 90 % [71] in combination with a reasonable temporal resolution around ~ 400 ps [72].
Specifications about the confocal microscope system used in this work can be found in Section 2.4.

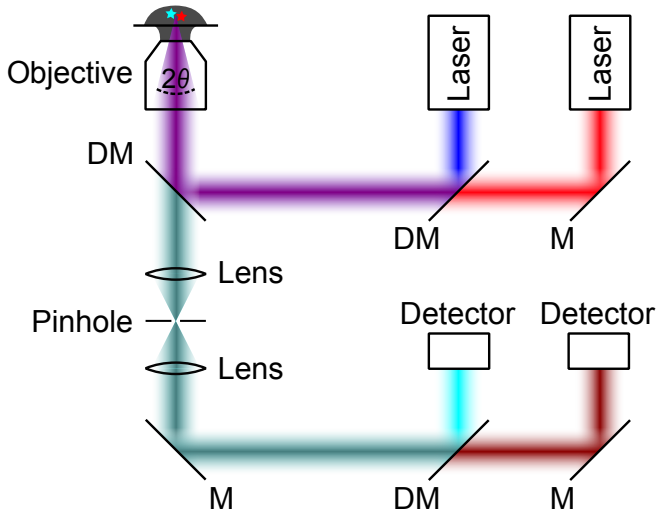

Figure 3.6: Schematic of a confocal microscope, (D)M= (dichroic) mirror.

3.2.2 Gaussian Beam Optics and the Molecular Detection Function

In the previous section, the excitation beam was treated as a plane wave. A more realistic description is to approximate the laser beam profile as a Gaussian beam. Consequently, the intensity distribution of a focused Gaussian beam is needed to describe the spatial excitation probability of fluorescent molecules within the sample droplet. If the Gaussian beam travels along the z-direction, its field vector in the paraxial representation is given by [73]

$$\mathbf{E}(r,z) = \mathbf{E_0}\,\frac{w_0}{w(z)}\,exp\left(-\frac{r^2}{w^2(z)}\right)\,exp\left(i\left[kz-\eta(z)+k\frac{r^2}{2R(z)}\right]\right), \tag{3.20}$$

where $\mathbf{E_0}$ is a constant field vector in the transverse plane, k is the magnitude of the wave vector, and $r = \sqrt{x^2+y^2}$. The phase correction $\eta(z)$ and the wavefront radius $R(z)$ are not further considered.
The beam radius specifies the radial distance from the optical axis at which the field amplitude drops to 1/e and is given by [73]

$$w(z) = w_0\sqrt{1+\frac{z^2}{z_0^2}}, \tag{3.21}$$

where w_0 is the beam waist and z_0 is called Rayleigh range.
The Rayleigh range is given by [73]

$$z_0 = \frac{k w_0^2}{2} = \frac{\pi n w_0^2}{\lambda_{exc}}, \tag{3.22}$$

where λ_{exc} is the excitation wavelength and n the refractive index of the sample medium.
Equation 3.21 is plotted in Figure 3.7. One can see that the minimal beam radius is given by the beam waist w_0 at $z = 0$. The beam stays approximately collimated within the Rayleigh range. For $z = z_0$, the beam diameter increases by a factor of $\sqrt{2}$.
The profile of the focused Gaussian beam is Lorentzian along z and Gaussian perpendicular to z [74,75]:

$$I(r,z) = I_0\left(\frac{w_0}{w(z)}\right)^2 exp\left(-2\frac{r^2}{w^2(z)}\right) \tag{3.23}$$

Now it might appear inappropriate to describe the strong focusing of high NA objectives within the paraxial approximation, which assumes that the transversal wave vector components are small compared to the component along the optical axes. However, the back aperture of the objective is usually underfilled in single-molecule experiments by using a laser beam that has a smaller diameter than the diameter of the back aperture. This results in a reduced effective NA and is done to elongate and increase the excitation volume which enables longer observation times [70]. The underfilling results at the same time in a less sharp focused beam and, hence, in an almost Gaussian beam at the focus [73,76]. Other approaches that describe the focusing of Gaussian beams with high NA objectives beyond the paraxial approximation are presented in references [75,77].
Finally, the probability that a fluorophore at a certain position gets excited is proportional to

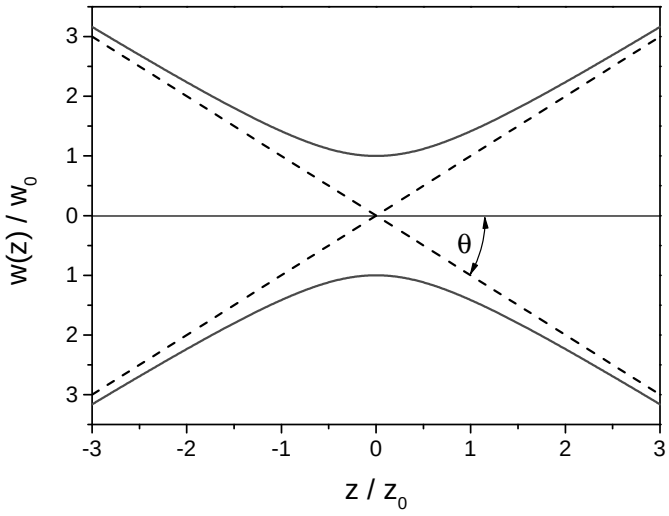

Figure 3.7: Radius of Gaussian beam in paraxial approximation (see Eq. 3.21).

the excitation intensity distribution, assuming that the fluorophore is not optically saturated [77].

So far the probability to excite the fluorophore was considered. For a full description of the detection process, the probability to collect the fluorescence of a sample molecule that resides at a certain position needs to be accounted. This so-called collection efficiency function (CEF) can be either calculated with full wave optics or, sufficiently well, with a semi-geometrical approximation [78].
The product of excitation and collection probability is called molecular detection function (MDF). It can be well approximated by a spheroid with Gaussian intensity distribution:

$$I(r,z) \;=\; I_0\, exp\left(-2\frac{z^2}{z_0^2}\right)\; exp\left(-2\frac{r^2}{r_0^2}\right) \tag{3.24}$$

In practice, the MDF can be obtained either indirectly by measuring the diffusion of a well-known molecule (see Sec. 3.2.5) or directly by imaging the point spread function (PSF) of a fluorescent object that is smaller than the diffraction limit, e. g. a fluorescent bead [79]. For simplicity, the MDF will be called confocal volume throughout this thesis.

3.2.3 Time-Correlated Single Photon Counting (TCSPC)

After the discussion of the optical excitation and detection in confocal microscopy which led to the definition of the MDF in the previous section, the photons finally need to be detected. The detector converts the information about the photon incidence into an electrical signal. Photomultiplier tubes are a good choice if a high temporal resolution is needed, however, they have intermediate quantum efficiencies of 20 – 45 % depending on the cathode material and the spectral region [80]. For single-molecule detection, avalanche photodiodes (APDs) are preferential as they offer high detection efficiencies up to 80 % [72] at the price of an intermediate temporal resolution. When a photon hits the APD, it generates a short breakthrough voltage pulse which is converted by a constant fraction discriminator (CFD) into a standardized rectangular signal. This signal is fed into a time-to-amplitude converter (TAC) together with the sync signal of the laser. The sync signal triggers the start of a linear voltage ramp that is stopped by the CFD signal. Consequently, the voltage is proportional to the delay between the laser pulse and the occurrence of the photon. Finally, the voltage is digitalized by a analog-to-digital converter and further processed by the electronics. This detection scheme is called time-correlated single photon counting (TCSPC) [72, 80].

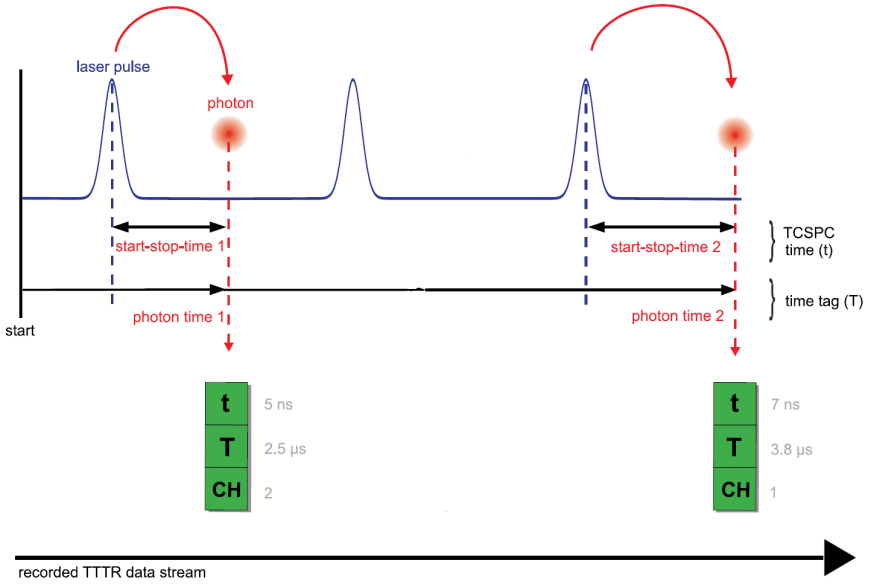

Figure 3.8: Principle of time tagged time-resolved data format. Three informations are saved for each photon: microtime t, macrotime T, and channel number. Adapted from [72].

An important characteristics of the instrumentation is the dead time. It characterizes the time that the system is 'blind' after a photon was detected. After the recording of a photon, the voltage at the APD needs to recover and the capacitor of the TAC needs to discharge before the system is ready to detect the next photon. The dead time causes a non-linearity of the detected count rate with respect to the rate of incident photons. The relation stays fairly linear for count rates below 10 % of the inverse dead time [80]. The dead time of the employed setup is < 95 ns. Another artifact of the dead time occurs if more than one photon arrive during the same excitation cycle. Only the first photon can be detected which causes a systematic deviation of the detected delay times towards shorter times. This is known as 'pulse pile-up' and can be prevented by having a photon detected only during 1 – 5% of the excitation cycles [72, 81]. If not stated otherwise, the laser repetition frequency was 20 MHz which results in a maximum detection count rate of 200 kHz.

It might now be of interest not only to detect the delay between the laser pulse and the photon occurrence but also the delay between the successive photons themselves. Therefore, an additional time tag is saved for each photon which is obtained by simply counting the sync signals (laser pulses). This time tag allows now to relate the photons to an absolute time scale. The TCSPC electronics generates a continuous stream of three informations for every photon in the TTTR data format (see Fig. 3.8). Besides the two temporal informations, also a channel number for the detector which registered the photon is saved. Depending on the optical elements in the detection path, the channel number thus encodes e. g. polarization or wavelength. Note, that both detection times are separated by several orders of magnitude: the TCSPC time is on the order of ns and the time tag is between $\mu s - ms$. The TCSPC time will be referred to as microtime and the time tag as macrotime in the following.

The manifoldness of analyses that can be performed based on only this three information for every photon is impressive. There are analysis that use either the micro or macro time alone, like TCSPC histogram fitting or fluorescence correlation spectroscopy (FCS), respectively. The full potential of the TTTR data format is however exploited when micro and macro times are combined e. g. in single-molecule sub-ensemble analyses [82].

3.2.4 Pulsed Interleaved Excitation (PIE)

In an experiment with dual-color labeled molecules, two lasers are used alternately for excitation. If the laser are alternated after each excitation, the scheme is called pulsed interleaved excitation [83]. In PIE, the microtimes are first used to divide the full TCSPC range into a window for each laser (see Fig. 3.9). The laser with the shorter wavelength emits a pulse in the first window and, accordingly, the second laser is used in the second time window. If the single lasers were operated at a frequency of 20 MHz, the effective repetition rate in the PIE mode is only 10 MHz. Hence, each laser is operated at the twofold power which results in the same average power as for 20 MHz. The combination of two time windows and two detection channels results in four different signals. If the channels are named 'donor' and 'acceptor' for simplicity, their signals in the first time window are denoted I_D and I_A, respectively. The acceptor signal in the second time window is denoted I_A^{Aexc}. The donor signal in the second time window I_D^{Aexc} can be neglected. The PIE scheme is used in single-molecule Förster resonance energy transfer (smFRET) to separately probe the presence of the acceptor

(see Sec. 3.3.3). In brightness-gated two-color coincidence detection, PIE is essential to obtain the individual bursts for both fluorophores (see Sec. 5.4).

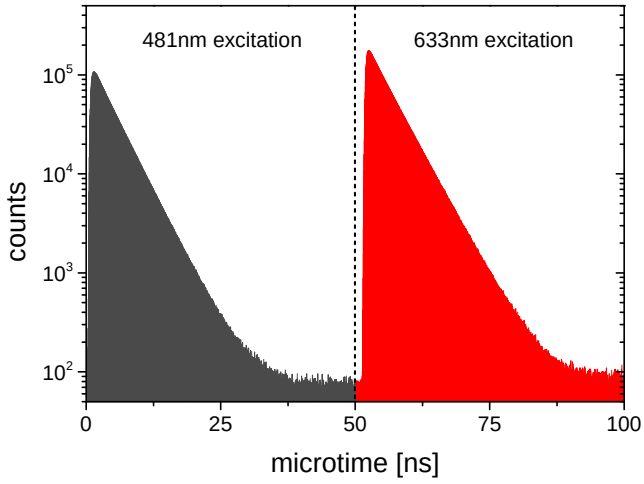

Figure 3.9: Principle of pulsed interleaved excitation (PIE).

3.2.5 Fluorescence Correlation Spectroscopy (FCS)

In the previous section it was mentioned that the TTTR data format allows a manifoldness of analyses. One of these analyses is fluorescence correlation spectroscopy (FCS), a powerful analysis tool to study translational diffusion and photophysical properties.

In FCS, fluorescence intensity fluctuations are analyzed which allows to characterize the underlying physical processes that caused the fluctuations. The fluctuations are analyzed by means of a correlation analysis of the fluorescence intensity time trace $F(t)$. The normalized autocorrelation function is given by [84]

$$G(\tau) = \frac{\langle F(t)\, F(t+\tau)\rangle}{\langle F(t)\rangle^2} = \frac{\langle \delta F(t)\, \delta F(t+\tau)\rangle}{\langle F(t)\rangle^2} + 1\,, \tag{3.25}$$

with $\delta F(t) = F(t) - \langle F(t)\rangle$ and the angle brackets denote averaging.
Equation 3.25 specifies how self-similar the signal $F(t)$ is after a lag time τ.
For freely-diffusing molecules, the diffusion into and out of the confocal volume is obviously one source of intensity fluctuations. The corresponding autocorrelation function is given by

$$G_{diff}(\tau) = \frac{1}{\langle N\rangle} \frac{1}{(1 + \tau/\tau_{diff})} \frac{1}{\sqrt{1 + \tau/\kappa^2 \tau_{diff}}}\,, \tag{3.26}$$

where $\langle N \rangle$ is the average number of fluorescent molecules in the confocal volume, τ_{diff} is the characteristic diffusion time, and $\kappa = z_0/r_0$ is the aspect ratio between axial and lateral extension of the confocal volume (see Eq. 3.24).
The autocorrelation function in Equation 3.26 assumes a constant fluorescence emission rate for each molecule [85]. However, the transition to the triplet state leads to short periods of absence of fluorescence. This flickering appears generally on much shorter time scales which allows to separate the diffusion and triplet blinking in the autocorrelation function [84]:

$$G(\tau) = G_{trip}(\tau) \cdot G_{diff}(\tau) = \left(1 + \frac{T}{1-T}\, e^{-t/\tau_{trip}}\right) \cdot G_{diff}(\tau), \tag{3.27}$$

where T is the fraction of molecules in the triplet state and τ_{trip} is the characteristic time for the blinking.
As can be seen from Equation 3.26, the autocorrelation for vanishing lag times is antiproportional to the number of molecules

$$G_{diff}(\tau \longrightarrow 0) = \frac{1}{\langle N \rangle}, \tag{3.28}$$

which allows to calculate the concentration of the sample molecules if the absolute size of the confocal volume is known.

One way to calibrate the size of the confocal volume is to analyze an autocorrelation function of a reference sample with a known diffusion coefficient, e. g. a freely diffusing dye. The knowledge of the diffusion coefficient D_{ref} allows to predict the diffusion time according to [84]

$$\tau_{diff} = \frac{r_0^2}{4\, D_{ref}}. \tag{3.29}$$

Consequently, the geometrical properties r_0 and z_0 are obtained by fitting the autocorrelation to Equation 3.26 or 3.27. The confocal volume is often described by the derived quantities $\kappa = z_0/r_0$ and the size of the effective confocal volume

$$V_{eff} = \pi^{2/3}\, r_0^2\, z_0. \tag{3.30}$$

FCS was used within this thesis mainly for two purposes. First, the diffusion properties of a sample can be checked by considering the diffusion coefficient given by Equation 3.29. Usually, an expected value for the diffusion coefficient is known. If the measured diffusion is faster, the sample is likely fragmented or free labels are present. In contrast, a slower diffusion than expected, indicates a (partial) aggregation of the sample. The second purpose of FCS is to obtain $\langle N \rangle$ which allows to calculate normalized quantities, like the molecular brightness (see Eq. 3.31), and which is needed to calculate an appropriate dilution factor for a subsequent single-molecule measurement.

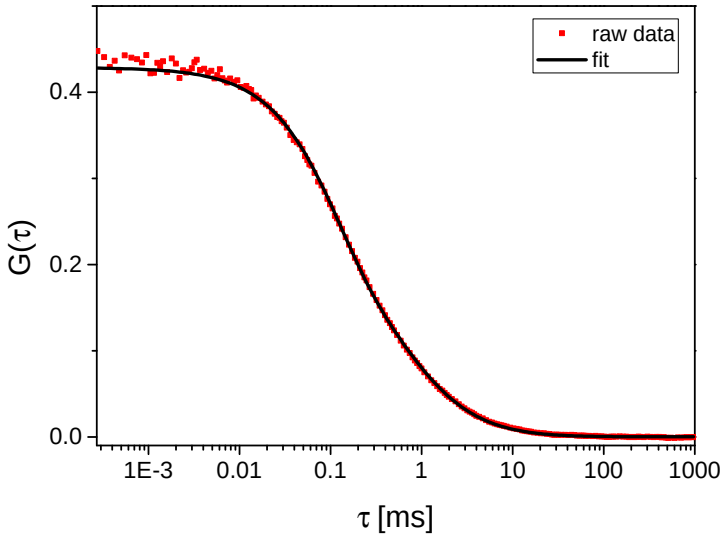

Figure 3.10: YFP autocorrelation function of glucose sensor construct no. 1 (see Sec. 4.4) fitted including triplet blinking (see Eq. 3.27). Fitting parameters are: τ_{diff} = 0.51 ms, $\langle N \rangle$ = 4.02, T = 0.42, τ_{trip} = 117 μs.

3.3 Single-Molecule Detection of Freely-Diffusing Fluorescent Biomolecules

3.3.1 Why Single-Molecule Measurements?

The way we think about biology on the molecular level is: How is molecule A interacting with molecule B? The way we measure it is: How are ~ 10^{17} copies of molecule A interacting with ~ 10^{17} copies of molecule B[1]. There is obviously some discrepancy between both conditions.
If all molecules of type A and B are each structural and chemically identical, their interaction will also be always identical. Due to the homogeneity it makes hence no difference how many molecules are investigated in order to determine a certain quantity. If we make a small excursion to solid state physics, we can recapitulate that this concept has proven to be extremely helpful there when describing the structure of a crystalline material. Instead of giving the coordinates of all atoms, the material is fully described by a lattice and a basis. In a metallic crystal it is also not necessary to characterize the interaction of e. g. a conduction electron with all atoms. Owing to the periodicity of the lattice and the homogeneity of the basis, the potential is periodic and the electron is described by a Bloch wave [86].

Returning to living matter, biological molecules behave completely different, even if they are of the same kind. Biomolecules in their native environment are usually neither present in a crystalline state nor are they absolutely structural identical. In addition, their interaction might vary due to the structural heterogeneity or (chemical) interaction with the environment. It is therefore very plausible to expect heterogeneity for systems that are based on biomolecules and their interactions.

The term of heterogeneity has certainly several aspects. Biomolecules exhibit a structural heterogeneity because they are mostly biopolymers, like proteins or DNA, and sample a certain conformational space. Furthermore, the structural heterogeneity is enlarged by the interaction with other biomolecules. This interaction may be unspecific (see Sec. 4.6) or specific when interacting with dedicated interaction partners (see Sec. 4.4).
A second source of heterogeneity arises when looking at the temporal behavior of biomolecules. In an ensemble measurement one can only characterize the equilibrium. A single-molecule experiment that is also conducted in equilibrium is nevertheless able to reveal temporal information e. g. about rate constants. An additional source of temporal heterogeneity arises if multiple transition pathways are present. With single-molecule resolution it is possible to specify for each molecule which pathway was taken (see Sec. 5.10).
Finally, it should be mentioned that the interpretation of single-molecule experiments relies on ergodicity of the system under study, i. e. the ensemble average equals the temporal average [87].

[1] Assuming a concentration of 1 mM and a volume of 1 ml.

3.3.2 Requisites for Single-Molecule Detection: The Signal-to-Background Ratio

After the recapitulation of the main characteristics of fluorescence in Section 3.1, it is now time to take a look at those properties that make it suitable for single-molecule detection. The specific question is: Which properties does a fluorophore need to bring along in order to be detected at the single-molecule level? If one assumes that the fluorophore is only observable for a certain time, like in the case of confocal detection of freely-diffusing molecules, the simple answer is that it should emit as many photons as possible during the dwell time in the confocal volume. Hence, it should exhibit (i) a high molar absorption coefficient, (ii) a low probability to populate the triplet state, (iii) absence of additional blinking processes like photo induced isomerization, (iv) a high fluorescence quantum yield, and (v) a sufficiently large photostability [56].
Next, the fluorescence of the single emitter needs to be effectively detected by the confocal setup introduced in Section 3.2. The optical and electronic detection result in a global detection efficiency. A quantity that combines the photophysical aspects as well as the detection efficiency is the molecular brightness (MB). It is defined as the detected fluorescence emission rate normalized to a single fluorophore:

$$MB = \frac{f - bg}{N}, \tag{3.31}$$

where f is the detected count rate of the sample, bg is the background count rate of solely the buffer and N is the average number of molecules in the confocal volume obtained by FCS (see Eq. 3.28). The value of N needs to be corrected when f becomes comparable to bg [88]. However, this is not the case here because it would anyway impede single-molecule detection.
Equation 3.31 provides simply the calculation rule for the experimentally obtained MB. Theoretical considerations yield the following expression for the expected rate of fluorescence emitted by a single fluorophore [77]:

$$k_f = \frac{\phi_f \, \sigma_f \, I_{exc}}{1 + \tau \, \sigma_f \, I_{exc}(1 + {}^{k_{isc}}/_{k_{ph}})}, \tag{3.32}$$

where ϕ_f is the fluorescence quantum yield, σ_f is the absorption cross section of the fluorophore, I_{exc} is the excitation intensity, τ is the fluorescence lifetime, k_{isc} is the rate of intersystem crossing, and k_{ph} is the rate of triplet state depletion.
Equation 3.32 shows that k_f will increase linearly for small I_{exc} and start to saturate for higher I_{exc} due to the finite fluorescence lifetime and the triplet state kinetics. Figure 3.11 shows that this dependency is indeed reflected in the experimental data for a selection of fluorophores. All fluorophores show a linear increase of the MB for low excitation intensities followed by a flattening for higher intensities. However, there is a clear trend that the MB of fluorescent

proteins shows a saturation at lower excitation powers accompanied with lower MBs.
The signal-to-background ratio is defined as

$$SB = \frac{MB}{bg} = \frac{k_f}{k_{bg}}, \tag{3.33}$$

where the first definition is related to experimental quantities and the second definition is related to theoretically predicted quantities.
The background count rate can be predicted by [77]

$$k_{bg} = N_{sol}\sigma_{sol}I_{exc} + k_{el}, \tag{3.34}$$

where N_{sol} is the number of solvent molecules in the detection volume, σ_{sol} is the molecular Raman scattering cross section of the solvent, and k_{el} represents the noise count rate of the detection electronics.
Plugging Equations 3.32 and 3.34 into Equation 3.33, one obtains:

$$SB = \frac{MB}{bg} = \frac{\phi_f\sigma_{dye}I}{1 + \tau\sigma_f I(1 + k_{isc}/k_{ph})} \cdot \frac{1}{N_V\sigma_{sol}I_{exc} + k_{el}}. \tag{3.35}$$

The experimental characterizations of the SB as a function of I_{exc} is shifted to Section 4.9.1. Briefly, three regions can be identified: (i) the SB increases linearly for small I_{exc} because the background is dominated by the detector dark counts and the MB increases linearly; (ii) at intermediate I_{exc} the SB reaches a plateau because k_f and k_{bg} increase both linearly with I_{exc}; (iii) at high I_{exc} the SB decreases again because the fluorescence emission starts to saturate and the background continues to increase linearly.

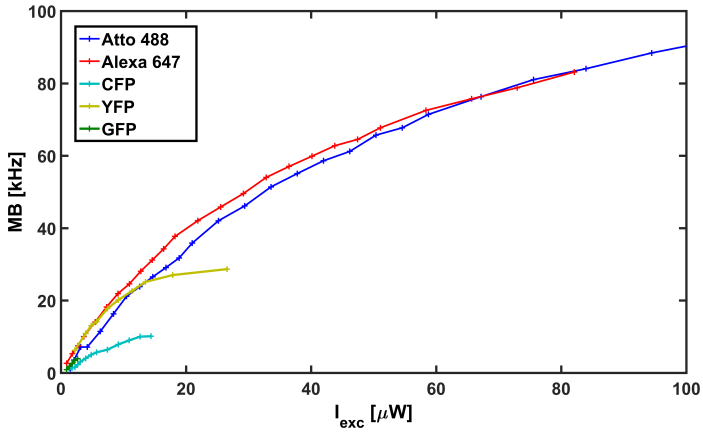

Figure 3.11: Measured molecular brightness (MB) for a selection of dyes and fluorescent proteins as as a function of excitation intensity.

3.3.3 Workflow of a Single-Molecule Experiment

This section deals with the practical implementation of a single-molecule experiment. The first step is to check the diffusion properties and the effectiveness of the cover slide blocking with the help of FCS. The next step is to dilute the sample appropriately to achieve single-molecule observation. For the choice of a suitable concentration, it is worth to consider the probability to find n molecules in the observation volume, given that the average number is $\langle N \rangle$, which follows a Poisson distribution [89]:

$$p_n(\langle N \rangle) = \frac{\langle N \rangle^n}{n!} e^{-\langle N \rangle} \tag{3.36}$$

Writing the probability explicitly as a function of $\langle N \rangle$ should stress that this is the experimental parameter that can be varied by adjusting the concentration: $\langle N \rangle = c\, V_{eff}$.
The crucial probability for single-molecule detection is that of finding not more than one molecule at a time:

$$p_{n>1}(\langle N \rangle) = 1 - p_0(\langle N \rangle) - p_1(\langle N \rangle) = 1 - (1 + \langle N \rangle) e^{-\langle N \rangle} \tag{3.37}$$

The choice of a specific $\langle N \rangle$ is a trade-off between a sufficiently small $p_{n>1}$ and reasonable time for the data acquisition. For single-molecule detection of FRET-based biosensor (see Sec. 4.9), the concentration was chosen to get $\langle N \rangle = 0.03$ which results in $p_{n>1} < 0.1\%$. The burst coincidence analysis requires even lower values as discussed in Section 5.8.

After the experiment has been conducted, the single-molecule signal has to be discriminated against the background. Most of the experimental time, there is no sample molecule in the confocal volume. From time to time, a sample molecule will traverse the confocal volume and emit a burst of fluorescence photons. The macrotime of each photon (see Fig. 3.8) can be utilized to generate a time trace of a suitable quantity characterizing the arrival of photons. A widespread approach is to calculate an intensity time trace with fixed bins [90]. Bursts will appear as spikes in such a time trace. Simple binning of the time trace is in many applications sufficient if the bin width is set slightly above the average dwell time [91]. Binning might not allow to detect dim bursts but especially in smFRET studies solely bright bursts are evaluated anyway. The bin size also dictates the temporal resolution for the determination of the beginning and ending of the burst. This might also be of minor interest for many application but in the case of burst coincidence detection, the precise knowledge of the start and end time tags of each burst is essential (see Sec. 5).
The burst identification method used in this work is based on the inter-photon lag (IPL) between consecutive photons. For the n^{th} photon it is given by

$$IPL(n) = t(n) - t(n-1)\,, \tag{3.38}$$

where t is the macrotime [92].
The IPL can be considered as an inverse count rate defined for each individual photon. Accordingly, bursts appear as dips in the time trace. The IPL time trace of the raw data is rather

noisy due to the stochastic character of photon emission (see Fig. 3.12). Therefore, a moving average filter was applied to the IPL time trace:

$$IPL_m(n) = \frac{1}{2m+1} \sum_{i=n-m}^{n+m} IPL(i) \tag{3.39}$$

where m is the half width of the smoothing.
The symmetric smoothing ensures that the start and end times are not shifted. A burst is identified when the IPL time trace intersects a burst detection threshold. The selection of a threshold value is a trade-off between a low m-value in order not to smooth over dim bursts, the reproduction of diffusion time and molecular brightness from FCS, and a low probability to misinterpret background fluctuations as a burst. Since these requirements partially compete each other, the following procedure was followed. The smoothing value m was chosen as low as possible and the IPL threshold was increased until the burst parameters matched those of FCS. More precisely, the single-molecule dwell time should be longer by a factor 4/3 compared to the diffusion time from FCS [93]. If the threshold results in a false-positive probability above 0.1%, the m-value was increased until burst parameters and background detection probability were matching the criteria [92].

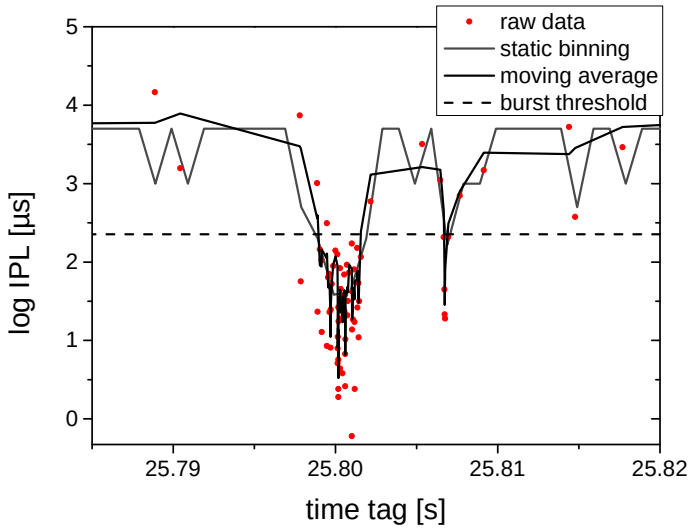

Figure 3.12: Exemplary IPL time trace with static binning and using a moving average filter. Long bursts are identified similar with both methods but static binning starts to become imprecise for dim bursts.

Depending on the analysis, different signals are used to generate the IPL and to identify the bursts. If all signals (I_D, I_A, I_A^{Aexc}) are merged, the corresponding IPL can be used for an all photon burst search [94]. This search will identify all fluorescent species and was used for the determination of correction parameters for the biosensor (see Sec. 4.9.2). Here, only bursts were used for the analysis that contained more than 40 photons. For the identification of only the FRET-capable molecules, the I_A^{Aexc} signal was used to identify the molecules that have a fluorescent acceptor. All photons of the actual FRET experiment (I_D, I_A) that occurred between the start and end time of these bursts were accumulated. The burst was analyzed if $I_D + I_A > 20$ which ensures the presence of the donor and sufficient counting statistics. In the case of a coincidence analysis (see Sec. 5), two bursts sets are generated using IPL time traces for $I_D + I_A$ and I_A^{Aexc}. The I_A^{Aexc} bursts probe the presence of the acceptor. The $I_D + I_A$ signal probes the presence of the donor because I_A arises due to FRET or spectral bleed-through. This approach enables to apply the coincidence analysis to high-FRET, low-FRET and also non-FRET samples.

Finally, before performing the intended single-molecule analysis, the stability over time was verified. Commonly, the total measuring time of a single-molecule experiment was several hours which was subdivided into data sets of 20 mins. For each of these subsets, a series of parameters was determined (e. g. dwell time, molecular brightness, background, etc.), and their stability over time was checked. If any parameter did significantly differ for one subset, the data of this subset was discarded.

4 Genetically-Encoded FRET-Based Biosensors

4.1 Introduction to Biosensors

Before directly jumping to FRET-based biosensors it is worth to consider the basic principles of biosensors in general. In 1992 the International Union of Pure and Applied Chemistry (IUPAC) defined a biosensor as "a device that uses specific biochemical reactions mediated by isolated enzymes, immunosystems, tissues, organelles or whole cells to detect chemical compounds usually by electrical, thermal or optical signals" [95]. This definition provides a reasonable and general description but for this reason it is at the same time also rather imprecise. Therefore, in 2001 the IUPAC specified the definition of a electrochemical biosensor as "a self-contained integrated device, which is capable of providing specific quantitative or semi-quantitative analytical information using a biological recognition element (biochemical receptor) which is retained in direct spatial contact with an electrochemical transduction element" [96]. This definition contains now all relevant components of a biosensor. A *recognition* element specifically interacts with the targeted (bio-)physical quantity, e. g. an analyte molecule, based on a biochemical interaction mechanism. Subsequently, a *transduction* element converts this interaction into a quantitative read-out signal [97]. The most famous example of an electrochemical biosensor is probably that of the glucose monitor devices that diabetes patient use to determine their glucose concentration in the blood. A first system was reported in 1962 and was based on the oxidation of glucose catalyzed by glucose oxidase (recognition element) which caused a change in pH (transduction) that could be measured [98].

Exchanging the word 'electrochemical' by 'optical' in the aforementioned definition, one obtains the definition of an optical biosensor which transduces the interaction of the recognition element into an optical signal. Among the biosensors that use an optical read-out, FRET-based biosensors represent an own class. Here, the amount of Förster resonance energy transfer (FRET) is used as the biosensor's signal. The basic composition of a FRET-based biosensor consists of a sensing domain, mostly a protein, that is linked to a donor and an acceptor fluorophore. There are various sensing mechanisms which can be based on cleavage, assembly or conformational changes of the sensing domain [99]. However, the choice of one of these sensing mechanism depends on the biological stimulus that should be measured. For example, the proteolytic cleavage of the sensing domain leads to a separation of donor and acceptor and, thus, to an irreversible, total loss of FRET. In contrast, protein-protein interactions can be monitored if the donor is attached to one protein and the acceptor, accordingly, to the other protein. Here, the FRET signal increases from zero for no interaction to a certain value if the proteins interact with each other.

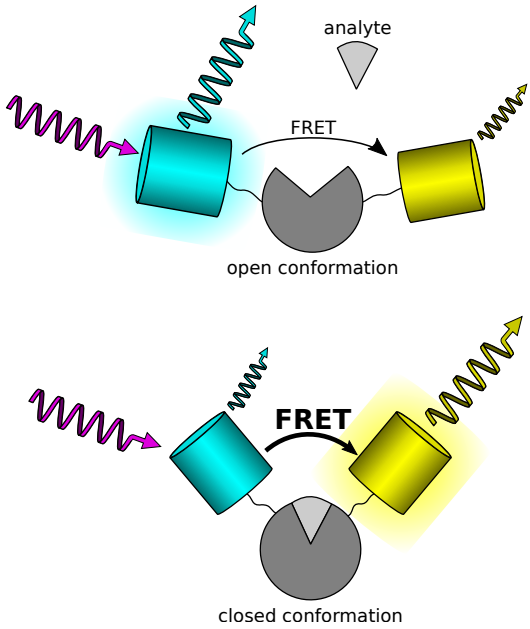

Figure 4.1: Operating principle of a FRET-based biosensor that utilizes a conformational change of the sensing domain. In the upper panel the sensing domain (dark gray) is in the open conformation. The donor (cyan) is excited with light of a suitable wavelength (purple arrow) and it will mostly emit fluorescence by itself. In the lower panel, the analyte binds which leads to a conformational change of the sensing domain to a closed conformation. The conformational change leads to a rearrangement of the donor and acceptor which causes an increased energy transfer and, hence, an increases of the acceptor's fluorescence emission (yellow).

For the concentration determination of ions or small molecule analytes, conformational changes of the sensing domain, that occur upon binding of the analyte, can be utilized because they can be potentially well transduced into a change in FRET (see Fig. 4.1). The working principle of the sensor is as follows. The energy transfer is low if the sensing domain is in the open conformation (analyte not bound) and it increases when the sensing domain undergoes a conformational change (analyte bound). Note, that the change from low FRET to high FRET upon binding of the analyte is indeed common but also the opposite behavior is possible and has been reported, e. g. in reference [30]. It is only necessary that there is an observable change in FRET upon binding of the analyte.

FRET-based biosensors that use conformational changes for sensing have a special feature: they consists of only one molecule which has the consequence that a clear distinction between the recognition and transduction element is not always possible. In fact, the trans-

duction element (donor and acceptor molecules) can interact with the recognition element (sensing domain) which may be either an undesired effect or which can be used to modify the affinity and sensitivity of the sensor. The main challenge in the design of highly sensitive sensor is to establish an effective transduction of the relatively small conformational change into a preferably large change in FRET.

4.2 Sensing Principles of Genetically-Encoded FRET-Based Biosensors

If fluorescent proteins are used as the donor and acceptor pair, the biosensor becomes a fusion protein and, thus, genetically encodable. Due to the possibility of *in vivo* applications, the class of genetically-encoded FRET-based biosensors has gained a lot of researchers' attention due to the great potential in fundamental research and possible diagnostic applications [20, 100].

Besides enabling *in vivo* measurements, the utilization of fluorescent proteins has an additional consequence for the generation of the FRET signal itself. The amount of FRET in assays using small organic dyes attached to the sensing protein depends only on the inter-dye distance (see Eq. 3.11 and 3.12 with $\kappa^2 = 2/3$), whereas FRET between two fluorescent proteins depends also on their relative orientation. The rotational correlation time of freely-diffusing green fluorescent protein was determined to be 17 ns which is considerably slower than its fluorescence lifetime of 3.2 ns (data not shown). Both time scales are in agreement with reported values [101]. Hence, during the excited state lifetime of the donor, the direction of the transition dipole moments of the donor and acceptor are rather static. For freely-rotating fluorescent proteins this would result in a static averaged value for κ^2 (see Eq. 3.14). If, in addition, not all possible relative orientations can be taken, an averaging is not possible and the amount of FRET will depend on the relative orientation. This conclusion applies to genetically-encoded FRET-based biosensor in general because other fluorescent protein variants have similar rotational correlation times, due to their structural similarity, and also comparable fluorescence lifetimes. The attachment of the fluorescent proteins to the sensing domain will further reduce their rotational mobility which ensures the validity of the static orientation regime.

A selection of possible relative orientations is depicted in Figure 4.2 where the donor is a cyan fluorescent protein and the acceptor a yellow fluorescent protein. The transition dipole moments are depicted as red arrows. They are oriented approximately perpendicular to the principal axis of the barrel structures of the fluorescent proteins because the fluorophore is also pointing perpendicular into the barrel and the dipole moments lie within the atomic plane of the fluorophore (see Fig. 3.5). However, the exact orientation of the dipole moment varies slightly for different variants of fluorescent proteins [102]. Three types of relative orientations of the fluorescent proteins are shown in Figure 4.2 which cover the whole range of relative dipole orientations. In a side-by-side orientation of the fluorescent proteins, the possible relative orientations of the dipole moments range from a collinear orientation that can turn into a perpendicular orientation by a 90° rotation of one fluorescent protein around its principal axis. These orientations correspond to the extreme values of the orientation fac-

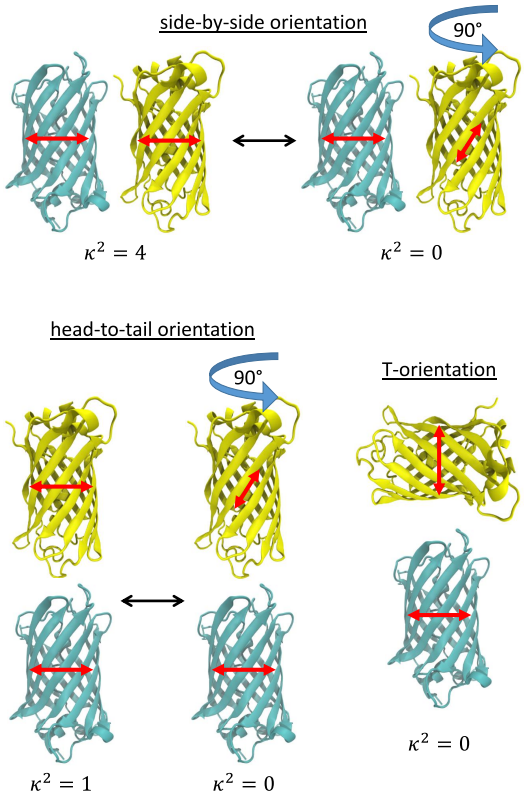

Figure 4.2: Possible spatial arrangements of two fluorescent proteins (pdb entries: 3ztf (CFP), 1myw (YFP)) and respective range of orientation factor κ^2. Dipole moments are depicted as red arrows.

tor of $\kappa^2 = 4$ and $\kappa^2 = 0$, respectively. In a head-to-tail alignment of the fluorescent proteins, the best coupling can be reached by a parallel orientation of the dipole moments ($\kappa^2 = 1$) which can again be transferred to a perpendicular alignment by a 90° rotation. Finally, a T-orientation of the fluorescent protein results in no coupling of the dipole moments which is also invariant of rotations around the principal axis of the fluorescent proteins. Note, that the positions of the cyan and yellow can be interchanged and the same results are obtained. These examples should illustrate the multiplicity of possible orientations. Although a simple 90° rotation can change the amount of FRET from zero to the maximal value, this is unlikely to happen in a real sensor. Also a mere distance change that preserves the relative orientation is unlikely to occur. In fact, the signal change of a real sensor will be caused by a combination of distance change and a relative reorientation of the fluorescent proteins. As

distance changes are limited by the conformational change of the sensing domain, a sensitive sensor should combine distance changes with a reorientation in a reinforcing manner, i. e. a decrease in the distance should be accompanied with a reorientation that favors the occurrence of FRET and vice versa.

In summary, fluorescent proteins are not only necessary to make biosensors genetically encodable but they enable amplified sensitivity by using the relative fluorophore orientation as an additional parameter to tune FRET. However, the design of biosensors with improved sensitivity is far from being straightforward due to the variety of parameters that can be changed in the design of the sensor and a lack of methods that would allow to verify the rational ideas that guide the design process [21]. In the following section, the degrees of freedom in the design of a biosensor are shortly discussed.

4.3 Design of Genetically-Encoded FRET-Based Biosensors

For a systematic optimization of an existing biosensor or the development of a new biosensor, one needs to become aware of the possible parameters that can be varied. First, one can choose between different variants of fluorescent proteins that are employed as donor and acceptor. One of the most popular choices in the past was to use cyan and yellow fluorescent proteins as donor and acceptor, respectively [99]. However, there are multiple variants of cyan and yellow fluorescent proteins that vary in their properties [19]. In general, variants with good photophysical properties, such as high photostability and high quantum yield are favored. Depending on the application, other parameters such as fluorophore maturation time and efficiency, dimerization tendency, or fluorescence lifetime need to be considered.

Next, the insertion position where the fluorescent proteins are linked to the sensing domain need to be optimized. The simplest approach is to place one fluorescent protein at each terminus of the sensing domain. In practice, this is not always giving the best results. Thus, the fluorescent proteins are internally fused to the sensing domain which enables much more insertion positions [30]. Finally, the fusion protein can be circular permuted which can also change the FRET signal [103].

One of the probably most important design parameters are the linkers that connect the fluorescent proteins and the sensing domain. This linkers enable on the one hand, a correct folding of the fluorescent proteins and the sensing domain. On the other hand, different linkers can enable or restrict rotational flexibility of the fluorescent proteins and change the orientation of the fluorescent proteins with respect to the sensing domain which will change FRET (see Fig. 4.2).

Overall, the design of sensitive sensors is a time consuming process due to the multiplicity of parameter combinations as outlined above. In order to reduce the complexity and to understand the effect of an individual parameter, this parameter can be varied while all other parameters are kept constant. Consequently, the impact of different linker combination is investigated for a glucose biosensor in Section 4.4 . In Section 4.6 the sensing domain is varied in a biosensor for macromolecular crowding.

4.4 Biosensor for Determination of Glucose Concentration

FRET-based biosensors promise to have a great potential in biotechnological applications. One example is a glucose sensor that can monitor the glucose concentration in a solution. In a typically production process in biotechnology, modified microorganism produce a desired product in large cultivation vessels. One aspect for an optimized production yield is to maintain optimal growing conditions for the microorganisms. Glucose serves as nutrition for the microorganisms and the concentration of glucose should be kept at the optimal value. A glucose sensor, immobilized in a transparent by-pass, would enable a non-invasive, real-time read-out of the glucose concentration. The information about the glucose concentration could be used for a feedback mechanism to maintain the optimal glucose concentration [104].

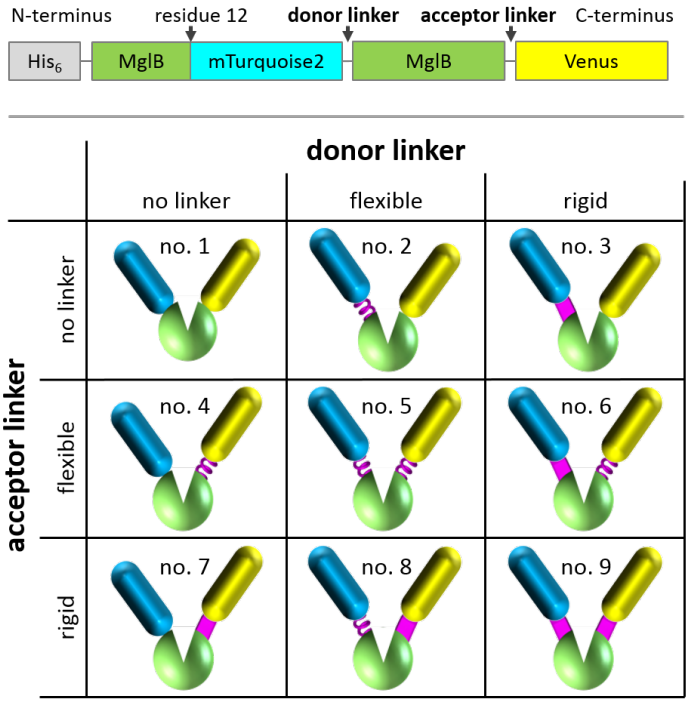

Figure 4.3: upper panel: Composition of the glucose sensor. The N-terminus begins with a polyhistidine followed by the glucose binding protein (MglB). The donor (mTurquoise2) is internally fused after residue 12 followed by the donor linker, the rest of MglB, the acceptor linker and the acceptor (Venus) itself. lower panel: Combination of three different linkers for donor or acceptor position results in 9 different sensor constructs. Adopted from [37].

The glucose sensor that is reported in this work was developed in the biotechnology institute (IBG-1) at Forschungszentrum Jülich. The sensor consists of the glucose binding protein MglB that is fused to mTurquoise2 (CFP) and Venus (YFP) as the donor and acceptor fluorescent proteins, respectively. MglB belongs to the class of periplasmic binding proteins and undergoes a conformational change based on the Venus flytrap principle upon binding of glucose. The conformational change is then transduced in a rearrangement of the fluorescent proteins which results in an increase of FRET.
The starting point for the sensor design was the sensor construct FLII^{12}Pglu-600µ developed by Deuschle and coworkers [30]. Deuschle et al. optimized the sensor by varying the insertion position of the fluorescent proteins. They report an increase of FRET changes upon glucose addition when truncating the linker of terminal attached fluorescent proteins or when internally fusing one fluorescent protein which they both attribute to a decreased orientational flexibility. The employed construct FLII^{12}Pglu-600µ has the donor inserted at position 12 of MglB. Steffen et al. developed a linker toolbox to further increase the sensitivity of FRET-based biosensors and first applied it to a lysine sensor [105]. The linker toolbox was consequently applied to the FLII^{12}Pglu-600µ glucose sensor construct. The toolbox consists of three different linkers (no linker, flexible linker, rigid linker) which results in nine possible combinations of linkers (see Fig. 4.3). All glucose sensor constructs were characterized in ensemble and vary remarkably in their sensitivity (see Sec. 4.5).

By screening of all possible constructs obtained with the linker toolbox, highly sensitive glucose sensors could be identified which are suitable for application. However, the strong dependency of the sensor performance on the linkers is not clear. By understanding the effect of the linkers it might also be possible to predict linker combinations and therefore enable a more rational and targeted sensor design.

4.5 Ensemble Read-Out of Biosensor Signal

So far, FRET-based biosensors were introduced and design strategies to improve the biosensor signal were discussed. In the following, it is shown how the signal of such biosensors is measured practically in a bulk experiment and which parameters are extracted to characterize the sensors.

As shown in Section 3.1.2 there are various ways to measure the amount of FRET. The most common approach for FRET-based biosensors is to measure the fluorescence emission intensities of donor and acceptor with an emission spectrometer after excitation of the donor. An example of the obtained emission spectrum is shown in Figure 4.4 for the glucose sensor construct no. 2 (see Fig. 4.3 for naming of sensor constructs). After exciting the donor with light of a wavelength of 420 nm, the emission spectrum exhibits two peaks at wavelengths of 472 nm and 524 nm which correspond to the emission peaks of the donor and acceptor, respectively. Dissolving the sensor in a buffer that contains 125 mM of glucose and performing the same experiment yields a different shape of the emission spectrum (blue line) in contrast to that without glucose (red line). One can observe a decrease in intensity of the donor peak with a concurrent increase of the acceptor peak intensity which is a clear indication of an in-

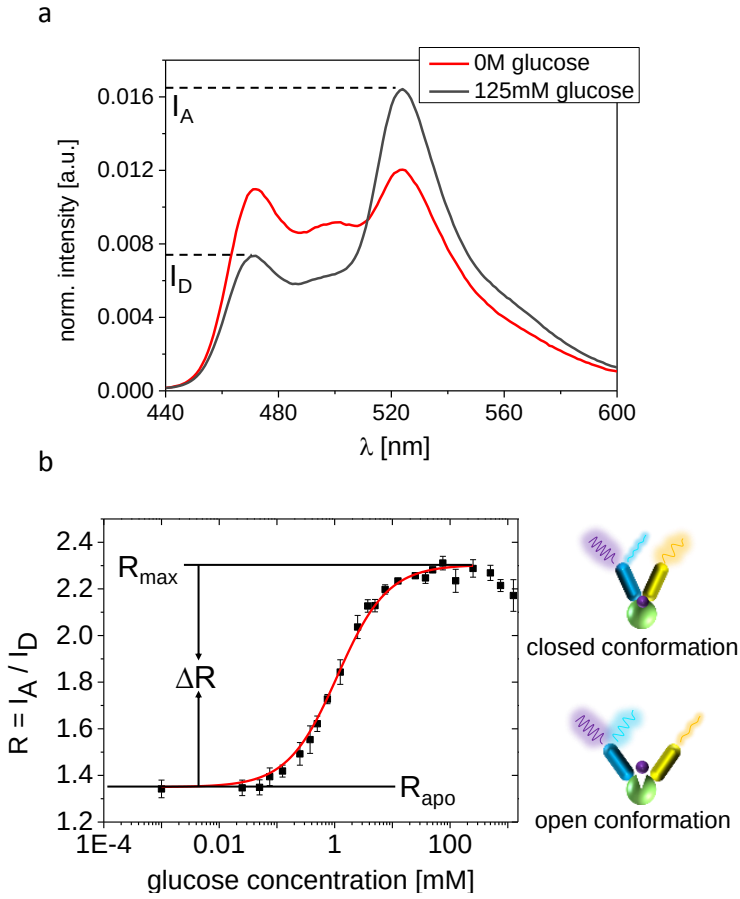

Figure 4.4: Ensemble characterization of FRET-based glucose sensor exemplarily shown for construct no. 2. (a) Emission spectrum after excitation with 420 nm shows two peaks belonging to the emission maxima of donor (472 nm) and acceptor (524 nm). After addition of glucose, the acceptor peak intensity I_A increases and the donor peak intensity I_D decreases caused by a higher energy transfer. (b) Isothermal binding curve of glucose sensor. The peak intensity ratio R shows a sigmoidal increase as a function of glucose concentration. The total increase ΔR characterizes the sensitivity of the sensor. Adopted from [37].

crease of FRET in the presence of glucose. As a measure for the extent of FRET it has become common to use the ratio

$$R = \frac{I_A}{I_D}, \tag{4.1}$$

where I_A and I_D are the maximum intensities of donor and acceptor bands, respectively. The definition of the sensor signal according to Equation 4.1 has the advantage that it does not depend on the absolute sensor concentration because R is a ratiometric quantity and it does not require any additional calibration parameters.

The performance of the sensor is characterized by plotting the peak intensity ratio R as a function of the glucose concentration (see Fig. 4.4). The resulting isothermal binding curve is fitted by a sigmoidal function:

$$R = \Delta R \frac{c_{glu}}{K_D + c_{glu}} + R_{apo}, \tag{4.2}$$

where $\Delta R = R_{max} - R_{apo}$ is the difference between the intensity ratio at saturated glucose concentrations R_{max} and without glucose R_{apo}, c_{glu} is the glucose concentration and K_D is the glucose concentration at which R rises half of the full increase. The relevant parameters that characterize the sensor are the K_D, which sets the glucose concentration regime that the sensor is sensitive to, and the sensitivity ΔR which is total increase of R. This binding curve could potentially serve as a calibration for *in vivo* measurements. However, the presence of crowding inside the cytosol will change (increase) the amount of FRET in a *in vivo* measurement in an unpredictable manner and, hence, impede a quantitative read-out. This effect will be discussed in detail in Section 4.7. In addition, other parameters such as pH, ionic strength, temperature, or the presence of intracellular metabolite have shown to change the FRET signal [106].

Coming back to the collection of glucose sensors, isothermal binding curves were recorded for all nine constructs by Julia Otten (IBG-1, Forschungszentrum Jülich). The constructs showed remarkable different sensitivities whereas construct no. 2 showed the highest sensitivity. The ΔR values of the investigated constructs are given in Table 4.2. The corresponding isothermal binding curves are given in ref. [37]. However, the microscopic reasons for the high sensitivity of construct no. 2 and also for the large range of sensitivities are still unknown. Here, single-molecule measurements provide the framework to perform a more detailed analysis (see Sec. 4.9).

4.6 Biosensor for Determination of Macromolecular Crowding

Most of our knowledge about proteins is based on measurements performed in highly-diluted aqueous solutions. However, the cellular environment of a protein is fundamentally different. The cell contains a mix of various macromolecules and cellular organelles. In general, each of these molecular species is not present at high concentrations but summing up all concentrations results indeed in remarkably high concentrations. A cell of *Escherichia coli* contains for example a macromolecule concentration of 300 – 400 $^{mg}/_{ml}$ [107]. This situation

is termed *crowding* and can dramatically change the properties of biomolecules. Possible effects are changes of diffusion, protein folding, and reaction kinetics [31]. Moreover, the macromolecules occupy a fraction of the total volume which leads to an apparent increase of concentration. This can results in 20 – 30 % of the volume occupied by macromolecules which is known as the "excluded volume effect" [32]. Yet, it is not completely understood how strong the influence of crowding on cellular processes is and how the extent of crowding varies between the different cellular compartments.

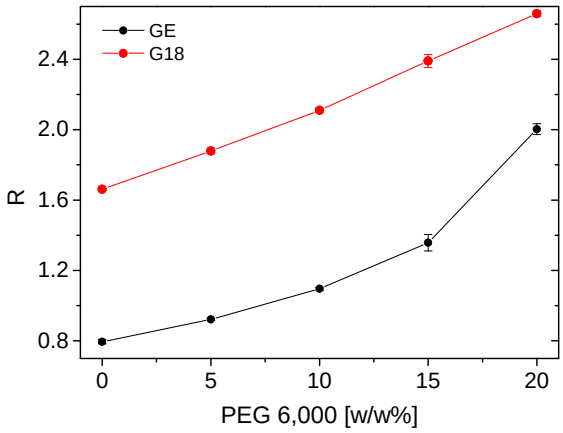

Figure 4.5: Intensity ratio R as a function of PEG 6,000 concentration for crowding sensor constructs GE and G18. Adopted from [37].

Recently, Boersma and coworkers developed a set of genetically-encoded FRET-based biosensors for the fundamental investigation of crowding [108]. Their sensors consist of a cyan and a yellow fluorescent protein that are fused to the terminal ends of a sensing domain. First, Boersma and coworkers used a sensing domain that consists of two alpha helices connected by a flexible random coil. They later presented different combinations of random coils and alpha helices for the sensing domain [38]. Interestingly, all sensor constructs show a clear response to crowding, even without flexible elements in the sensing domain. For example, construct E6 in reference [38] has only one alpha helix sandwiched between the donor and acceptor. It is nevertheless obvious that the sensing domain must contain some flexible elements that enables a certain compressibility of the probe. For the construct E6 this flexibility is most probable provided by the additional linker elements that connect the alpha helix to the fluorescent proteins.

All of these crowding sensor constructs have in common that a clear differentiation between the linker and the sensing domain is not possible. In fact, the polypeptide chain that connects donor and acceptor fluorescent protein can be considered as the linker and at the

same time as the sensing domain. Since the sensing domain has no tertiary structure, it is reasonable to assume a compaction of the probe with the increase of crowding. However, the exact sensing mechanism remains unclear and a detailed understanding would also enable to design improved crowding sensors that might also be specific for a certain size or composition of the crowder molecules.

In this work, two crowding sensor constructs were analyzed. The construct GE is the aforementioned prototype construct consisting of two alpha helices connected by a flexible coil. The second sensor is construct G18 which contains no alpha helix but only a random coil. The crowding sensor constructs are characterized *in vitro* using artificial crowding agents. A frequently used crowding agent is polythylene glycol (PEG) which is a linear polymer that coils up when dissolved in water. Another common crowding agent is Ficoll, a crosslinked polymer, which forms stiffer particles compared to PEG. A characterization of the pure crowder solutions analogous to the smFRET characterization showed fluorescence impurities of Ficoll and larger PEG molecules that appear as fluorescence bursts. While ensemble measurement like FCS can tolerate a certain amount of impurities due to the large signal-to-background ratio, a frequent appearance of impurity bursts in single-molecules experiments would impede the detection of the sensor and lead to a false interpretations of the data. Only PEG 6,000 (m = 6,000 Da) showed a sufficiently low background and is therefore used as the crowding agent for single-molecule experiments. For an ensemble characterization of both constructs with Ficoll and other PEG crowders see references [38,108]. The response of both sensor constructs to PEG 6,000 is shown in Figure 4.5. The amount of FRET is characterized by the peak intensity ration R (see Eq. 4.1). Construct G18 exhibits a larger initial R value which increases approximately linear with increasing PEG 6,000 concentration. Construct GE has a smaller R value in the absence of crowding but increases stronger with increasing PEG concentration. In contrast to the glucose sensors, the crowding sensors shows no saturation of the signal which means that addition of PEG leads to a steady compaction of the sensor. Finally, it is not clear how the glucose sensor would react to a crowded environment which is investigated in the following section.

4.7 Response of Glucose Biosensor to Crowding Conditions

In the previous section, a biosensor was presented that was specifically designed to report on macromolecular crowding. The consequent next question would be, how the glucose sensor presented in Section 4.4 reacts to a crowded environment. Crowding becomes relevant if the glucose sensor should be applied *in vivo* but also for *in vitro* applications like the determination of the glucose concentration in a cultivation buffer [104]. If very large volumes of a cultivation buffer should be monitored one needs a trapping mechanism for the sensor molecules. Otherwise, the sensor would disperse in the whole cultivation volume which would reduce the signal and waste a lot of the sensor material. It has been shown that the encapsulation of sensor molecules inside silica nanoparticles is a possible immobilization strategy [109]. These nanoparticles could be kept in a transparent bypass which would enable a real-time read-out of the sensor signal and, hence, the glucose concentration. However, the confinement inside the nanoparticles is expected to have a similar effect as crowding.

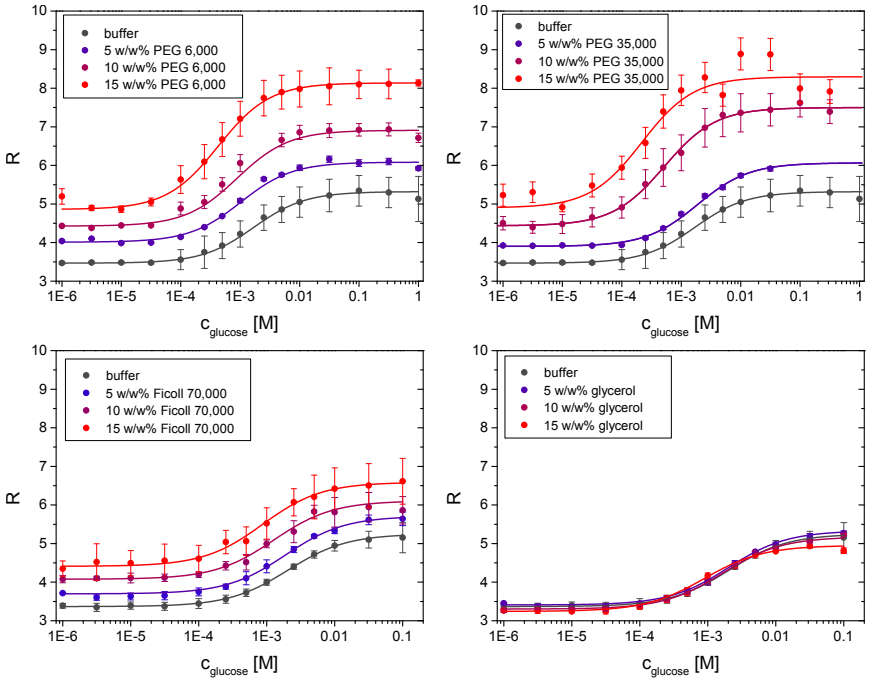

Figure 4.6: Isothermal binding curves of glucose sensor similar to construct no. 2 but with exchanged fluorescent protein variants eCFP and Citrine as donor and acceptor, respectively. Glucose titration is performed in various concentrations of crowding agents PEG 6,000 (upper left), PEG 35,000 (upper right), Ficoll 70,000 (lower left), and glycerol (lower right). Sigmoidal curves are fitted according to Equation 4.2. Macromolecular crowder (PEG, Ficoll) cause a shift of the binding curves whereas glycerol is not a macromolecule and leads to no remarkable change. Adopted from [110].

The response to crowding of a slightly modified glucose biosensor based on construct no. 2 was investigated. The modified sensor carries the exchanged fluorescent protein constructs eCFP and Citrine as donor and acceptor, respectively. The change of the fluorescent protein variants was done during the design process. However, different fluorescent protein constructs are not expected to give qualitatively different results. Figure 4.6 shows that macromolecular crowding agents such as PEG and Ficoll lead to a shift of the isothermal binding curves towards larger R-values. PEG 6,000 and PEG 35,000 lead to a similar shift of the binding curve whereas Ficoll 70,000 shows a smaller shift compared to PEG. A pure viscosity enhancer like glycerol leads to no signal change which proves that only macromolecules have the ability to increase the sensor signal. Hence, the increase of the R-value

in the presence of macromolecular crowding agents can be related to a compaction of the glucose sensor. In Figure 4.7 the exclusive effect of crowding is shown by plotting only the increase of R_{apo} (without glucose). All crowding agents lead to a linear, non-saturating increase which is similar to the response of the crowding sensors (see Fig. 4.5). The absolute increase of the glucose sensor signal is even higher than that of the crowding sensor (cf. Figs. 4.5 and 4.7). Hence, metabolite sensors have also the potential to be used as crowding sensors. For *in vivo* applications, however, the binding of the metabolite has to be inhibited because the signal will superimpose with the crowding signal. Otherwise the same signal can be caused by different combinations of metabolite concentration and crowding. In reference [111] such an approach was realized by using an ATP insensitive mutant of an ATP biosensor.

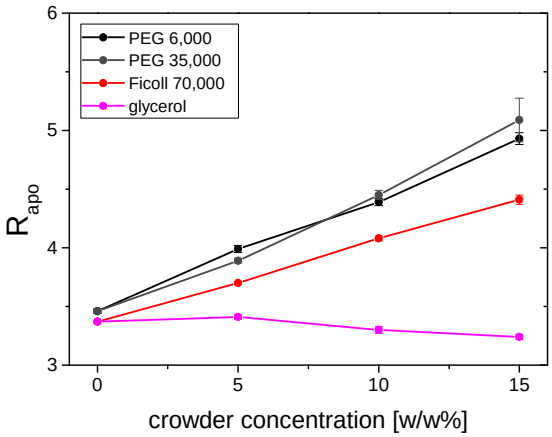

Figure 4.7: Increase of glucose sensor signal in absence of glucose (R_{apo}) is approximately linear for PEG and Ficoll. Pure viscosity enhancer glycerol leads to no change of R_{apo}. Adopted from [110].

Finally, the question remains whether the presence of crowding and glucose have a distinct effect on the glucose sensor. The linear response to crowding and the observation of a sigmoidal glucose binding curve in the presence of crowding indicate indeed that both effects are independent of each other. This is supported by the observation that very high crowder concentrations can cause R-values in the absence of glucose that exceed the R-value of a glucose saturated, non-crowded sensor (data not shown). However, ensemble measurements do not give enough evidence for this hypothesis and single-molecules measurements in Section 4.9.6 will provide a deeper insight.

4.8 Limitations of Ensemble Characterization

So far, the peak intensity ratio R was used as the biosensor's signal (see Eq. 4.1). Although the biosensor community mostly agreed to use R as a FRET indicator, it has the disadvantage to be not normalized which results in an unbounded quantity. Instead, it is preferential to use a quantity that describes the underlying physical process of FRET such as the energy transfer efficiency E (see Eq. 3.16).

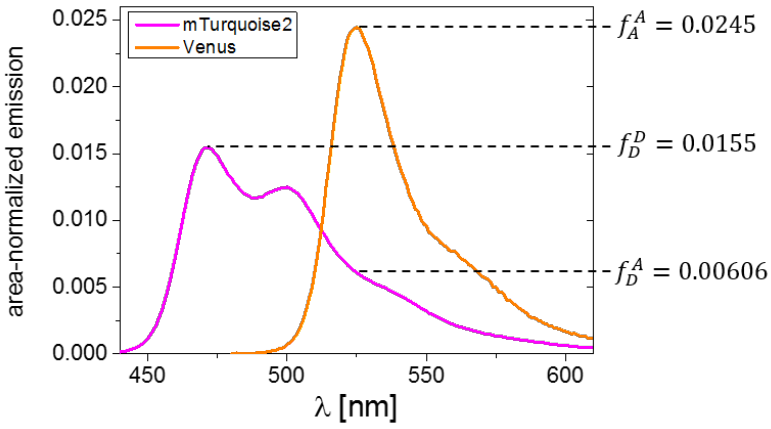

Figure 4.8: Area-normalized fluorescence emission spectra of mTurquoise2 and Venus. Adopted from [37].

To understand how the transfer efficiency and the intensity ratio are related, an expression for the conversion from energy transfer efficiency values to R-values is derived in the following taking into account a donor-only fraction of sensor molecules. For a given transfer efficiency E, the R-value is composed of all contributions adding up at the donor and acceptor emission peak:

$$\begin{aligned} R(E, x_{D0}) = \frac{I_A(E, x_{D0})}{I_D(E, x_{D0})} &= \frac{(1 - x_{D0})\left(c_A^A \cdot E + c_D^A(1 - E)\right) + x_{D0} \cdot c_D^A}{(1 - x_{D0})c_D^D(1 - E) + x_{D0} \cdot c_D^D} \\ &= \frac{(1 - x_{D0})E}{1 - (1 - x_{D0})E} \cdot \frac{c_A^A}{c_D^D} + \frac{c_D^A}{c_D^D}. \end{aligned} \tag{4.3}$$

The numerator accounts for acceptor intensity caused by FRET as well as spectral crosstalk of the donor by FRET-capable molecules and by donor-only molecules. The donor intensity originates likewise from FRET-capable molecules and donor-only molecules.
The constants

$$c_x^y = f_x^y \cdot \Phi_x \tag{4.4}$$

account for the peak-to-area fraction f_x^y of the emission spectrum of fluorophore x emitted at the wavelength used to read the intensity of fluorophore y with quantum yield Φ_x (see Fig. 4.8).

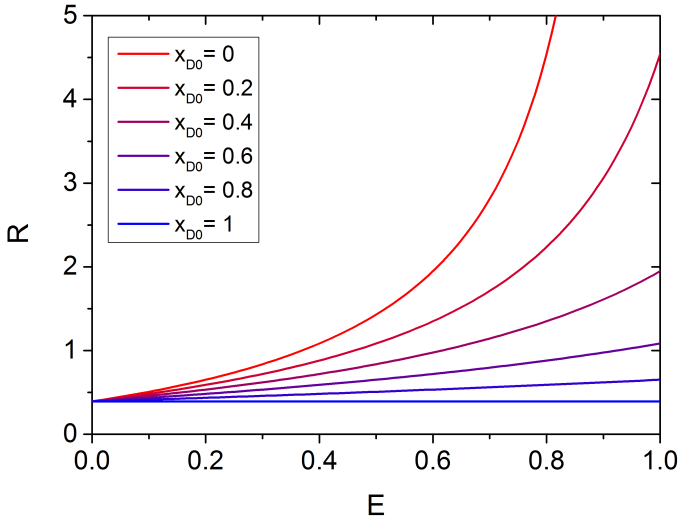

Figure 4.9: Conversion of transfer efficiency E to peak intensity ratio R for various donor-only fractions according to Equation 4.3. Donor and acceptor are mTurquoise2 and Venus, respectively. Quantum yields were determined as $\Phi_D = 0.90$ and $\Phi_A = 0.59$ which results in $c_D^D = 0.0139$, $c_D^A = 0.00546$, and $c_A^A = 0.0144$. Adopted from [37].

The transfer efficiency E in Equation 4.3 applies only to molecules that are capable to show FRET, i. e. they have a pair of fluorescent donor and acceptor. However, an ensemble experiment cannot deliver this transfer efficiency but a reduced transfer efficiency due to the presence of donor-only molecules:

$$E_{ens} = (1 - x_{D0})\, E\,. \tag{4.5}$$

Hence, the conversion of an ensemble transfer efficiency is given for the glucose and crowding biosensors by

$$R_{gluc}(E_{ens}) = \frac{E_{ens}}{1 - E_{ens}} \cdot 1.04 + 0.392 \qquad \text{D= mTurquoise2, A=Venus} \tag{4.6a}$$

$$R_{crow}(E_{ens}) = \frac{E_{ens}}{1 - E_{ens}} \cdot 1.38 + 0.392 \qquad \text{D=mCerulean3, A=mCitrine.} \tag{4.6b}$$

Equation 4.6b shows a good agreement with an experimentally determined conversion function (see Fig. S3 in ref. [38]).
Equation 4.3 is plotted in Figure 4.9 for the FRET pair mTurquoise2 and Venus. For small transfer efficiencies the conversion to R is almost linear whereas it becomes highly nonlinear for large transfer efficiencies. For $x_{D0} = 0$ it is even diverging for $E \longrightarrow 1$. As a consequence, the sensitivity, i. e. the slope of R(E), is apparently increased for large transfer efficiencies. This may implicate that a sensor should work with transfer efficiencies as high as possible. However, the read-out noise will increase for very high values of R because the donor signal will be very weak and the signal will become prone to very small perturbations. The utilization of the transfer efficiency E instead of the intensity ratio R can prevent such effects.

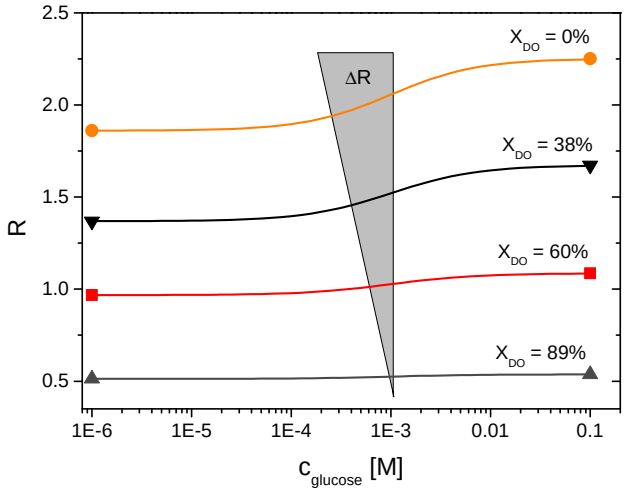

Figure 4.10: Effect of different donor-only fractions x_{D0} on ensemble read-out of glucose sensor construct no. 4. Donor-only fractions were determined with BTCCD (see Chap. 5). The sensor had an initial donor-only fraction of 38 % which was increased to 60 % and 89 % by photo-bleaching the acceptor with a 532 nm laser. Orange line shows hypothetical sensor signal for interpolation to vanishing donor-only fraction. Only R_{apo} and R_{max} were measured and connected to guide the eye according to Equation 4.2 with a fixed K_D. Adopted from [37].

A second aspect that can be extracted from Figure 4.9 is the impact of the donor-only fraction x_{D0} on the ensemble read-out. If one assumes a biosensor that can change between a low FRET and a high FRET state, like the glucose biosensor, the signal changes between R_{apo} ans R_{max} (see Fig. 4.4). In terms of transfer efficiencies, this would correspond to one state having a transfer efficiency of E_{apo} and the other state E_{max}. In Figure 4.9 these states

could be represented by two vertical lines positioned at E_{apo} and E_{max}. Depending on the value of x_{D0}, the resulting R-values would considerably differ. An increase of x_{D0} would reduce the R-values but also reduce the sensitivity $\Delta R = R(E_{max}, x_{D0}) - R(E_{apo}, x_{D0})$. This was experimentally verified by partially photo-bleaching the acceptor with a 532 nm laser and measuring R_{apo} and R_{max} as shown in Figure 4.10.

A donor-only fraction of sensor molecules mainly arises due to an incomplete chromophore maturation of the acceptor. Chromophore maturation depends on various parameters and is in general not perfect. As a consequence, the application of a calibration curve as well as the comparison of different sensor constructs among each other relies on identical donor-only fractions. Since this is generally not the case, it can result in wrong results/conclusions. Here, single-molecule measurement have the advantage to get results free of donor-only molecules and even to quantify the donor-only fraction.

4.9 Single-Molecule Measurements of Genetically-Encoded FRET-Based Biosensors

4.9.1 Experimental Realization

Reports about single-molecule Förster resonance energy transfer (smFRET) studies with fluorescent proteins are absolutely rare in literature. Already in the year 2000, the group of Moerner published a single-molecule study of 'cameleon', a calcium sensor based on calmodulin as the the sensing domain [112]. However, the counting statistics was rather poor and no further publications could be found. The reasons for the rareness of single-molecule studies may be manifold. Possible explanations may be found in the existence of different scientific communities. While the 'single molecule community' focuses on studies with bright fluorescent dyes that also enable to extract structural information, the 'biosensor community' works mainly on sensor development with a focus of possible *in vivo* applications. While *in vivo* smFRET studies with fluorescent dyes are already extremely challenging [113], the method of choice for *in vivo* experiments with fluorescent protein based biosensors is mostly fluorescence lifetime imaging (FLIM) [99].

A further reason for the rareness of smFRET studies with fluorescent proteins is obviously the poor applicability of fluorescent proteins for single-molecule studies compared to organic dyes. As shown in Section 3.3.2, the crucial parameter for the feasibility of a single-molecule experiment is the signal-to-background ratio.

The absorption coefficients and quantum yields of fluorescent proteins (see e. g. ref. [19]) are indeed comparable to those of organic dyes which reveals as similar initial slopes in Figure 3.11. However, the molecular brightness of fluorescent proteins saturates at much lower absolute values due to a pronounced triplet state occupation (see Fig. 3.10). In addition, fluorescent proteins exhibit a pronounced and complex photobleaching behavior [114, 115]. As a consequence, for a sufficient large signal-to-background ratio, the background must be reduced as much as possible. The main source of background is Raman scattering of the

excitation light. The major Raman scattering peak of water has a wavenumber shift of $\Delta\tilde{\nu} \approx 3400\,\mathrm{cm}^{-1}$ [116] which results in a wavelength of the Raman scattered light of

$$\lambda_R = \left(\lambda_{exc}^{-1} - \Delta\tilde{\nu}\right)^{-1}, \tag{4.7}$$

where λ_{exc} is the excitation wavelength.
Here, the spectral proximity of cyan fluorescent protein (CFP) and yellow fluorescent protein (YFP) leads to further complications. The excitation wavelengths must be chosen such, that the Raman scattering peaks overlay as little as possible with the emission band filters of CFP and YFP. Likewise, the emission filters should cover most of the emission spectrum. A reasonable choice of excitation wavelengths that accounts for these constraints is the use 440 nm and 510 nm for CFP and YFP excitation, respectively. CFP is commonly excited with slightly lower wavelengths [99, 117] but the Raman scattering peak of 440 nm is located at approximately 516 nm which is sufficiently blocked by the emission filters (see Fig. 4.11). Note, that 440 nm is only the nominal emission wavelength of the employed laser. The actual emission wavelength of diode lasers can slightly shift from laser to laser. The employed laser

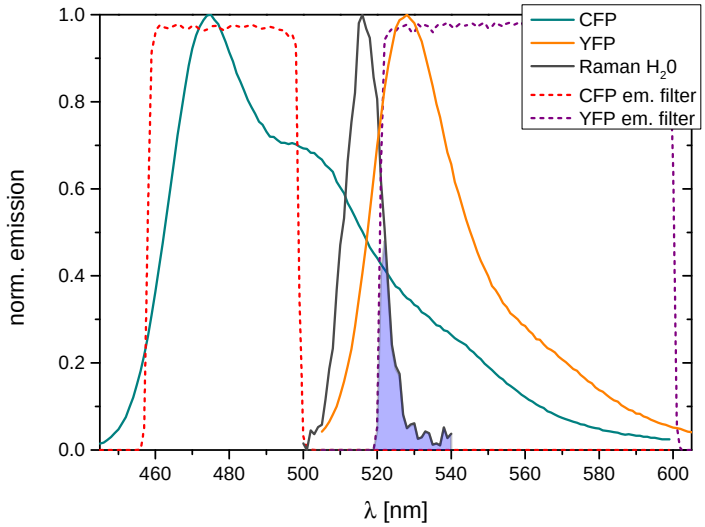

Figure 4.11: Emission spectra of mTurqouise2 (CFP) and Citrine (YFP) with corresponding band-pass filters. Raman scattering peak of 440 nm excitation in water was obtained with the fluorescence spectrometer and is sufficiently blocked. Only the blue shaded area leaks into the YFP channel. Note, that for simplicity only the emission filters are considered.

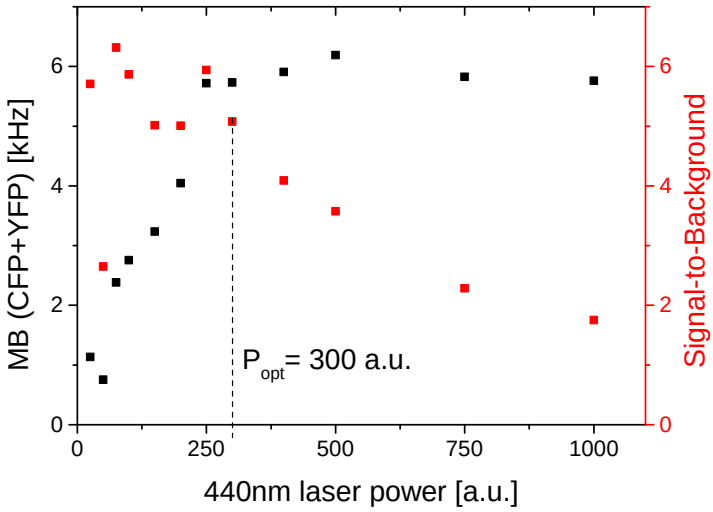

Figure 4.12: Molecular brightness (MB) and signal-to-background ratio of summed CFP and YFP signal as a function of excitation power of 440 nm laser.

displays an asymmetric, power-dependent emission spectrum with an average wavelength of 437 nm (see App. Fig. A.1) which is even better blocked by the emission filters.

An excitation power is finally chosen by measuring the molecular brightness and the signal-to-background ratio as a function of the excitation power for the glucose sensor. This was done separately for 440 nm excitation and plotting the joint molecular brightness of CFP and YFP (see Fig. 4.12), and for YFP molecules brightness after 510 nm excitation (see Fig. 4.13). One can see that the signal-to-background ratio (SB) follows the behavior predicted by Equation 3.35. For small laser powers, the SB increases because the background is dominated by the constant, electronic part. For intermediate laser powers, the SB is constant because both, the MB and the SB increase linearly. The SB decreases finally for large laser powers because the MB saturates. The optimal laser powers are reached at the end of the SB plateau. The 440 nm laser was operated at exactly this power of 300 a.u.. This is also the power at which the number of photons emitted by a single molecule reaches its maximum. Higher laser powers lead to shorter diffusion times because the CFP photobleaches before it totally traversed the confocal volume (see App. Fig. A.2). The fact that both considerations (triplet state occupation vs. photobleaching) result in the same optimal laser power, shows that both properties can become the limiting factor of a smFRET with fluorescent proteins. It should be mentioned that the joint MB of CFP and YFP can slightly vary depending on the amount of FRET.

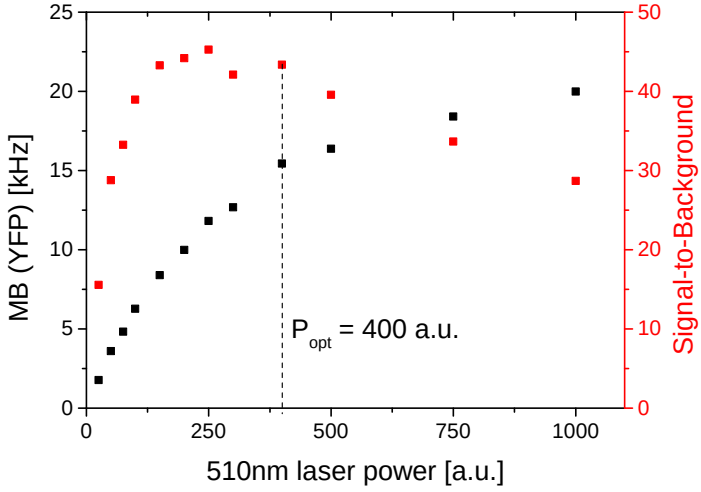

Figure 4.13: Molecular brightness (MB) and signal-to-background ratio of YFP signal as a function of excitation power of 510 nm laser.

The 510 nm laser was operated at the beginning of the plateau at 100 a.u.. The direct YFP excitation is only needed to verify the presence of the acceptor and the lower power prevents rapid photo bleaching. The conversion to real powers can be found in Appendix Figures A.3 and A.4.

4.9.2 Determination of Correction Parameters α, β, γ

Finally, single-molecule experiments of the glucose and crowding biosensor were performed with the setup presented in the previous section. The workflow of the experiment including the discrimination of the bursts is described in Section 3.3.3. The PIE scheme was used to separately excite the donor and acceptor (see Sec 3.2.4). The accurate calculation of burst-wise FRET efficiencies relies on a likewise accurate determination of the donor and acceptor intensities (see Eq. 3.16). Besides the detection efficiency ratio γ, two further experimental imperfections need to be accounted for: direct acceptor excitation and spectral leakage of donor emission into the acceptor channel. Both lead to an apparent increase of the acceptor signal. The corrected intensities are given by [118]

$$I_D = F_D - BG_D\,, \tag{4.8a}$$

$$I_A = F_A - BG_A - Lk - Dir\,, \tag{4.8b}$$

where F_D and F_A are the measured photon counts for donor and acceptor, and BG_D and BG_A are the background counts in the donor and acceptor channel, respectively.
The background is obtained as the product of the dwell time and the background count rate. The number of leakage photons is given by

$$Lk = \alpha I_D , \tag{4.9}$$

where α is the leakage coefficient that quantifies the ratio of donor photons leaked in the acceptor channel with respect to those emitted in the donor channel.
The number of directly excited photons is accordingly characterized by a direct excitation coefficient β according to

$$Dir = \beta I_A^{Aexc} , \tag{4.10}$$

where I_A^{Aexc} is the acceptor emission signal after direct acceptor excitation.
For the FRET pair of CFP and YFP, the corrections become even more crucial because of the large spectral overlap of absorption (see App. Fig. A.1) and emission (see Fig. 4.11). The spectral crosstalk coefficient α depends only on the shape of the donor emission spectrum and the probability of direct acceptor excitation β is proportional to the acceptor's absorption coefficient at 440 nm (donor excitation wavelength) and the ratio of both laser powers [119]. Since these properties are similar for the CFP and YFP variants used for both biosensors, α and β were determined for the glucose sensor and also used for the crowding sensor.

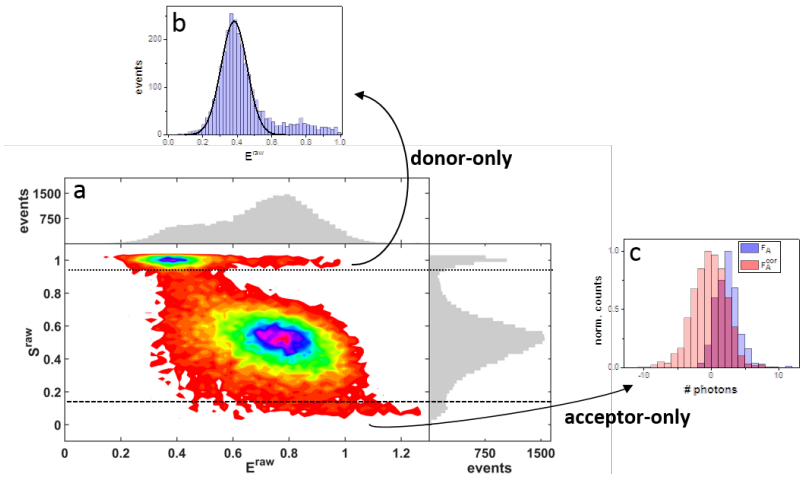

Figure 4.14: 2D-plot of raw transfer efficiency E^{raw} and raw stoichiometry S^{raw} is used to sort donor-only molecules ($S^{raw} > 0.95$, dotted line) and acceptor-only molecules ($S^{raw} < 0.15$, dashed line) of all detected glucose sensor bursts. Donor-only and acceptor-only populations are used to determine α and β, respectively (see main text). Adopted from [37].

The determination of α and β requires an analysis of a donor-only and acceptor-only species of the sensor, respectively. This was realized by sorting all detected single molecules in a 2D-plot of E_{raw} versus S_{raw} as shown in Figure 4.14. An ensemble of sensor molecules contains always a fraction of donor-only and acceptor-only molecules due to incomplete chromophore maturation or bleaching. The stoichiometry is defined by

$$S = \frac{I_D + I_A}{I_D + I_A + I_A^{Aexc}}. \tag{4.11}$$

The raw transfer efficiency and stoichiometry are obtained when only applying the background correction to all intensities in Equations 4.8a and 4.8b and setting $\gamma = 1$ in Equation 3.16.
Donor-only molecules appear in the E_{raw} vs. S_{raw} plot at $S_{raw} \approx 1$ and, accordingly, acceptor-only molecules at $S_{raw} \approx 0$. Hence, donor-only molecules were identified with $S_{raw} > 0.95$ and acceptor-only molecules with $S_{raw} < 0.15$. A fit of a Gaussian distribution to the E_{raw} histogram of donor-only molecules yielded a mean of $E_{raw,D0} = 0.39$ and was used to calculate the leakage coefficient

$$\alpha = \frac{E_{raw,D0}}{1 - E_{raw,D0}} = 0.64 \pm 0.01. \tag{4.12}$$

The standard procedure to obtain the direct acceptor excitation coefficient β is to fit the S_{raw} histogram of acceptor-only molecules. However, the fit was not reliable because the S_{raw}-distributions of the donor-acceptor and acceptor-only populations overlap. As an alternative approach, the emission of the acceptor-only molecules after donor excitation was analyzed. The direct excitation coefficient was varied manually until the distribution of the corrected acceptor signal peaked around zero. The obtained value is

$$\beta = 0.078. \tag{4.13}$$

Finally, the dual-tagged population was used to determine the γ factor. Therefore, the proximity ratio E^{pr} (transfer efficiency for $\gamma = 1$) and the corrected stoichiometry S^{cor} were used. Both quantities are obtained with the fully corrected intensities (see Eqs. 4.8a, 4.8b) and the respective definitions. The center positions were read by eye (see Fig 4.15) for all investigated glucose sensor constructs in pure buffer and at 125 mM glucose (see Sec. 4.9.4). A linear fit of a $1/S_{cor}$ against E_{pr} plot can be used to calculate γ according to

$$\gamma_{glu} = \frac{\Omega - 1}{\Omega - 1 + \Sigma} = 1.42 \pm 0.11, \tag{4.14}$$

where Ω is the y-intercept and Σ is the slope.
There was not enough data to perform a similar fit for the crowding sensor. Alternatively, it was assumed that the detection efficiencies for the CFP and YFP variants were similar. As a consequence, γ needs to be solely adjusted for different quantum yields:

$$\gamma_{crow} = \frac{\phi_{A,crow}}{\phi_{D,crow}} \frac{g_{A,crow}}{g_{D,crow}} \approx \frac{\phi_{A,crow}}{\phi_{D,crow}} \frac{g_{A,glu}}{g_{D,glu}} = \frac{\phi_{A,crow}}{\phi_{D,crow}} \frac{\phi_{D,glu}}{\phi_{A,glu}} \gamma_{glu} = 1.89 \pm 0.15 \tag{4.15}$$

Quantum yields of $\phi_{D,crow}$ = 0.87 [120], $\phi_{A,crow}$ = 0.76 [121], $\phi_{D,glu}$ = 0.90, and $\phi_{A,glu}$ = 0.59 were used. The quantum yields of the glucose sensor were obtained with the low intensity FCS method [122] (data not shown).

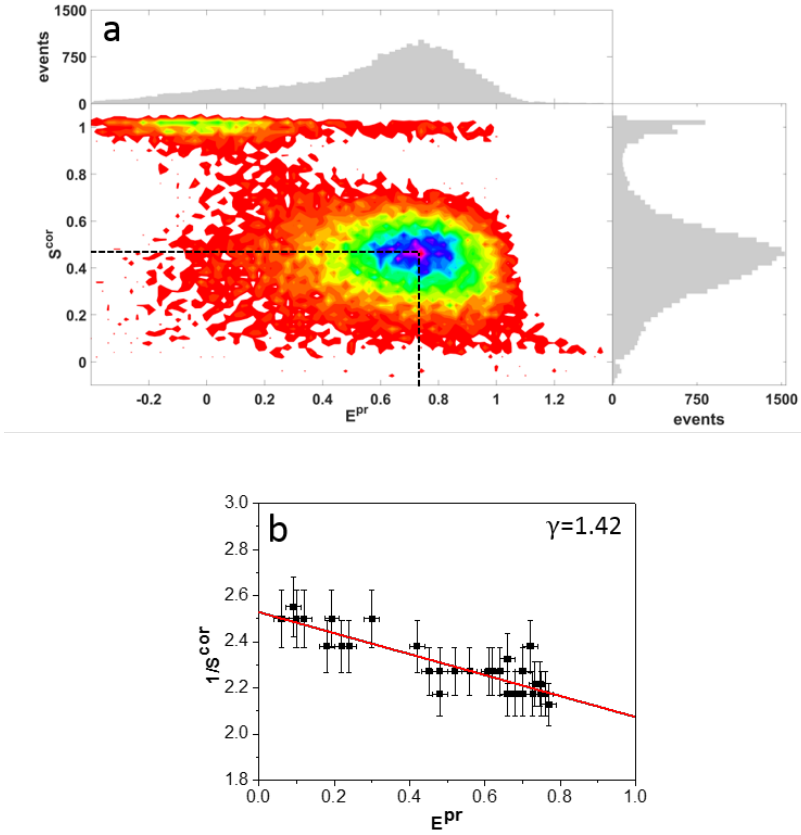

Figure 4.15: (a) 2D-plot of proximity ratio E^{pr} and corrected stoichiometry S^{cor} is used to identify center of donor-acceptor population (dashed lines). (b) Plot of $1/S^{cor}$ against E^{pr} for all investigated glucose sensor constructs. Linear fit (red line) is used to calculate γ (see Eq.4.14). Adopted from [37].

4.9.3 Correction for PEG 6,000 Background

Background measurements of PEG 6,000 solutions showed a small number of fluorescence impurities that arise as high FRET events for concentrations above 10 w/w%. Consequently, background measurements were performed for each PEG 6,000 concentration under identical conditions as the smFRET sensor experiments and analyzed with the same parameters. The obtained pseudo FRET histograms were rescaled to the measurement time of the real experiment and subtracted.

4.9.4 Single-Molecule Characterization of Glucose Biosensor

In order to gain insight into the working principles of the glucose sensor, smFRET measurements were performed at three characteristic glucose concentration: in the absence of glucose, at the K_D around 1 mM, and at the concentration of saturated sensor signal of 125 mM.

First, the most sensitive sensor construct no. 2 was analyzed. The corresponding smFRET efficiency histograms are shown in Figure 4.16. In presence of 1 mM glucose, two populations are visible that center at a low and high transfer efficiency. Each of the populations shows a broad distributions of transfer efficiencies which leads to a partial overlap of them. Without glucose (for 125 mM glucose) the histograms show only one major population at low (high) transfer efficiencies with a tail towards high (low) transfer efficiencies. These observations lead to the following interpretation. The glucose sensor can be described by a two state system. The apo state corresponds to a low FRET state and is mainly occupied in the absence of glucose. At saturating glucose concentration, the sensor is mainly in the glucose-bound, high FRET state and at the K_D concentration both states are equally occupied. Accordingly, all histograms were fitted globally with two Gaussian distributions that have fixed mean positions and fixed widths for each population. The weighting of each population was kept as a free fitting parameter for every glucose concentration. The fit describes the data reasonably well and it becomes also apparent that due to the large width of the distributions, the high FRET (low FRET) state in the absence of glucose (at 125 mM) appears only as a shoulder.

The width of the populations is broadened well beyond the shot noise limited width which is given by [94]

$$\sigma_{SN} = \sqrt{\frac{E_c\,(1 - E_c)}{N_\gamma + 1}}, \tag{4.16}$$

where E_c is the center position of the population and N_γ is the average number of photons within a burst.

A comparison to the shot noise limited distributions is given in Figure 4.17. The effects that can lead to a broadening of the FRET efficiency distribution are manifold [123]. One inherent reason is the existence of the static averaging regime. The rather low threshold for the number of donor and acceptor photons might lead to an imperfect static averaging. Further processes that cause a broadening must occur on a timescale similar or slower than the dwell time of a few ms. A possible photophysical effects is the triplet state transition which indeed occurs on a timescale of a few 100 μs (see Fig 3.10). So far, it cannot be definitely stated if also conformational heterogeneity within each state contributes to the broadening. If so, the fluorescent proteins would not sample the full conformational space, i. e. all accessible posi-

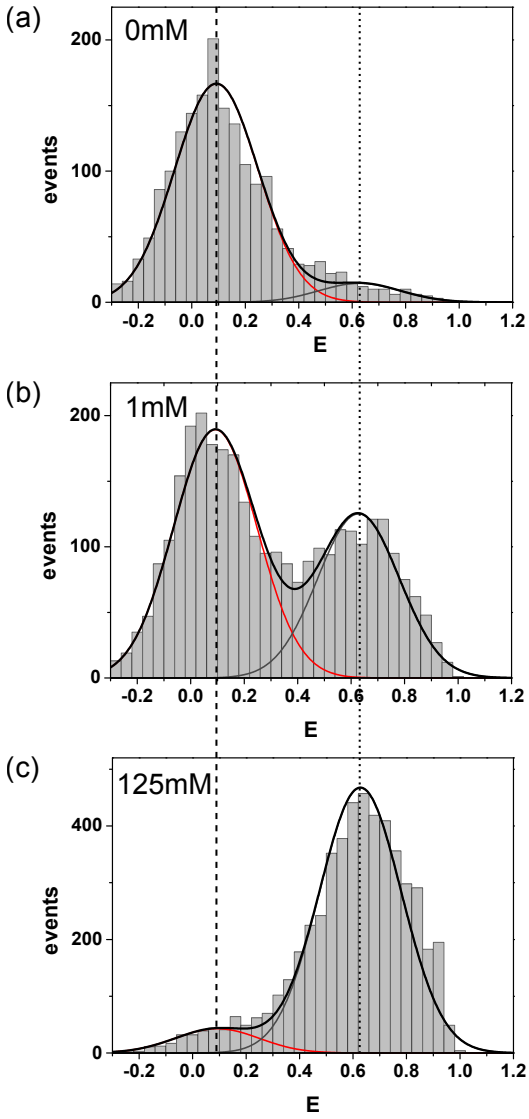

Figure 4.16: smFRET histograms of glucose sensor construct no. 2 (a) without glucose, (b) at glucose concentration equal to K_D and (c) at saturating glucose concentration of 125 mM. Adopted from [37].

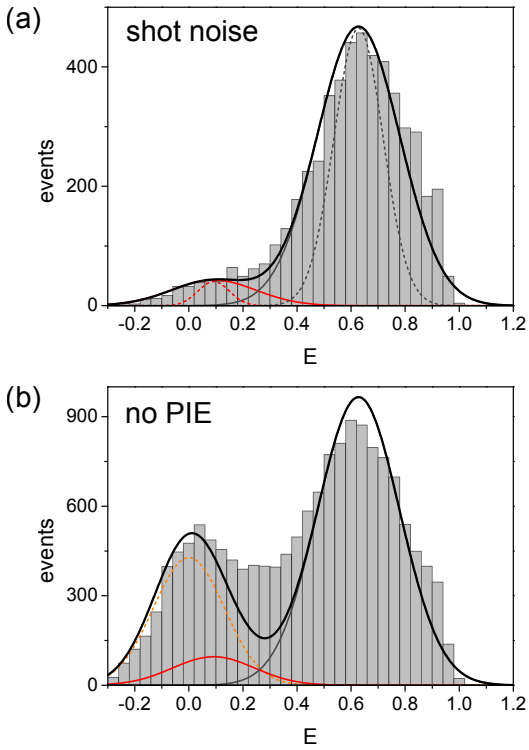

Figure 4.17: smFRET histograms of glucose sensor construct no. 2 at saturating glucose concentration of 125 mM (a) with shot noise limited widths of populations (dashed lines) and (b) without the exclusion of donor-only molecules (dashed orange line) by PIE. Adopted from [37].

tions/orientations, within the ms timescale. The observation of a smaller width in a smFRET histogram for an unstructured sensing domain suggest such a scenario [124]. In contrast, the smFRET histograms of the crowding sensors show a similar width which (see Sec. 4.9.6) contradicts any conformational heterogeneity. The only certain statement that can be made about dynamics is related to the interconversion dynamics between the unliganded and the liganded state. The interconversion must take place on a time scale slower than ms because each population is separately observable in the smFRET histogram at intermediate glucose concentration [125].

Next, the initial sensor construct no. 1 was characterized as shown in Figure 4.18. In contrast to construct no. 2, the distribution of FRET efficiencies peaks already at high values in the absence of glucose. At the K_D concentration, the distribution becomes asymmetric with a tail towards lower transfer efficiencies but there is no clear separation of two populations.

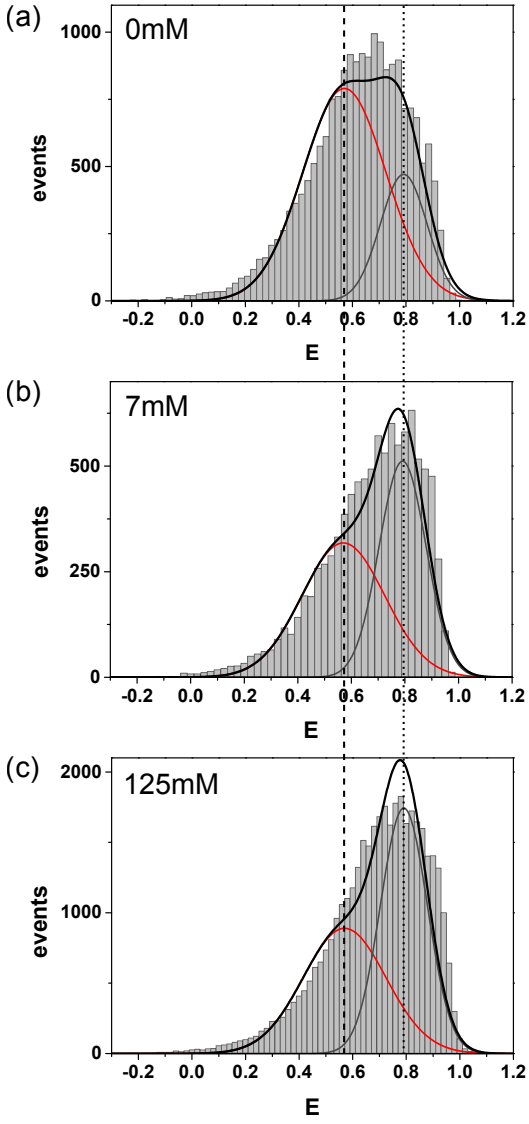

Figure 4.18: smFRET histograms of glucose sensor construct no. 1 (a) without glucose, (b) at glucose concentration equal to K_D and (c) at saturating glucose concentration of 125 mM. Adopted from [37].

Further increasing the glucose concentration leads to a hardly noticeable change of the histogram. The similarity of the FRET efficiency histograms for 7 mM and 125 mM is caused by utilization of the intensity ratio R for the determination of K_D. In Section 4.8 it was shown that the conversion of E to R becomes nonlinear for larger absolute values of E. Since construct no. 1 works at large absolute values of E, the K_D is systematically overestimated and does not correspond to an equal occupation of the apo and bound state. Based on the observations made for construct no. 2, it is nevertheless reasonable to assume also a two state model for construct no. 1 and, hence, fit the histograms globally with two populations. In comparison to construct no. 2, the occupation of the high FRET state is much more pronounced in the absence of glucose and, vice versa, a remarkable fraction remains in the lower FRET state at 125 mM glucose.

The single-molecule characterization of all remaining sensor constructs was not possible because the experiments are very time consuming. Hence, a subset of constructs was selected by keeping always one linker of the most sensitive construct no. 2 fixed (flexible donor linker, no acceptor linker). This subset of constructs corresponds to the second column (all constructs with flexible donor linker) and the first row (all constructs without acceptor linker) in Figure 4.3 . In addition, construct no. 4 was investigated which exhibits interchanged linkers with respect to construct no. 2. The smFRET efficiency histograms of construct no. 3, 4, 5, 8 are shown in Appendix Figures A.5, A.6, A.7, and A.8, respectively, and were also fitted globally with a two state model for each construct. The fitting results for all investigated constructs are given in Table 4.1.

In summary, the presented examples of construct no. 2 and no. 1 represent the extreme scenarios of a well and poorly performing sensor, respectively. All other constructs showed a behavior that was in between. This manifests of course also in the smFRET histograms. A more detailed analysis that uses the smFRET results to characterize the sensor performance follows in the next section.

4.9.5 Performance of Glucose Biosensor

In the previous section, the smFRET characterization of the most sensitive (no. 2) and the less sensitive (no. 1) sensor construct were presented. The FRET efficiency histograms exhibit a low-FRET population that corresponds to the open (apo) state and a high-FRET state that corresponds to the closed (liganded) state of the glucose binding domain.

A more quantitative evaluation is possible by comparing the difference of various parameters between glucose saturated (125 mM) and non-liganded conditions that are presented in Table 4.2. First, each construct can be characterized on the ensemble level with the increase of the peak intensity ratio ΔR (see Sec. 4.5). As discussed in Section 4.8, the utilization of R as a measure for FRET has the disadvantage that, in contrast to the transfer efficiency, the signal is not proportional to the underlying physical process. This is clearly demonstrated by comparison of ΔR to $\Delta E_{avg,ens}$, the average change in transfer efficiency that would be obtained at ensemble level. $\Delta E_{avg,ens}$ is calculated by taking the average change of transfer

construct	glucose [mM]	$\langle E \rangle_{sm}$	E_1	E_2	σ_1	σ_2	p_1	p_2	ΔE_{bin}
no. 1	0	0.62	0.57	0.79	0.15	0.09	0.75	0.25	0.023
	7	0.67					0.52	0.48	0.025
	125	0.69					0.48	0.52	0.020
no. 2	0	0.13	0.09	0.63	0.15	0.15	0.92	0.08	0.040
	1.1	0.30					0.61	0.39	0.040
	125	0.60					0.09	0.91	0.040
no. 3	0	0.24	0.17	0.63	0.18	0.14	0.85	0.15	0.040
	1.1	0.37					0.58	0.42	0.040
	125	0.63					0.06	0.94	0.040
no. 4	0	0.29	0.18	0.48	0.17	0.18	0.63	0.37	0.040
	1	0.42					0.17	0.83	0.040
	125	0.47					0.07	0.93	0.040
no. 5	0	0.19	0.13	0.53	0.16	0.16	0.84	0.16	0.035
	125	0.51					0.08	0.92	0.035
no. 8	0	0.40	0.29	0.58	0.17	0.15	0.64	0.36	0.040
	1.2	0.52					0.24	0.76	0.035
	125	0.53					0.17	0.83	0.040

Table 4.1: Fitting results of smFRET histograms of all investigated glucose sensor constructs. $\langle E \rangle_{sm}$: mean single-molecule transfer efficiency; E_1, E_2: center position of Gaussian distribution of low FRET and high FRET state; σ_1, σ_2: width of Gaussian distribution of low FRET and high FRET state; p_1, p_2 weighting of Gaussian distribution of low FRET and high FRET state; ΔE_{bin}: bin width of histogram.

efficiency measured at single-molecule level $\Delta E_{avg,sm}$ and reducing it according to the donor-only fraction x_{D0} of the construct (see Fig. 5.24):

$$\Delta E_{avg,ens} = (1 - x_{D0})\, \Delta E_{avg,sm}\,. \tag{4.17}$$

For example, construct no. 5 and no. 8 exhibit a similar ΔR but no. 5 shows a 2.5-fold larger $\Delta E_{avg,ens}$ because it operates on an lower absolute value of E.

The difference between the center positions of the high-FRET and low-FRET population is named ΔE_{pop}. It defines the quality of the transduction mechanism, i. e. how well the conformational change is transduced in a preferable large change of FRET. In this sense, it sets the limit for the sensor performance because the maximum change of the transfer efficiency would be achieved if all molecules transfer from the low-FRET to the high-FRET state. The

construct	ΔR	$\Delta E_{avg,ens}$	$\Delta E_{avg,sm}$	ΔE_{pop}	$\Delta E_{avg,ens}/\Delta E_{pop}$	$\Delta E_{avg,sm}/\Delta E_{pop}$
no. 1	0.40	0.04	0.07	0.22	18 %	30 %
no. 2	0.98	0.30	0.47	0.54	56 %	87 %
no. 3	0.92	0.27	0.39	0.47	57 %	83 %
no. 4	0.22	0.14	0.18	0.30	44 %	60 %
no. 5	0.49	0.22	0.31	0.39	57 %	79 %
no. 8	0.52	0.09	0.13	0.29	30 %	45 %

Table 4.2: Parameters characterizing the performance of the glucose sensor constructs.

effects that lead to a reduction of the sensor performance can now be analyzed individually. First, the ratio $\Delta E_{avg,sm}/\Delta E_{pop}$ quantifies to which extend the construct makes use of the transduction mechanism. A reduction of $\Delta E_{avg,sm}$ with respect to ΔE_{pop} appears if molecules are already in the high-FRET state in the absence of glucose and if the low-FRET state is not completely depopulated at saturating glucose conditions. Construct no. 2, 3 and 5 have the highest utilization levels of the transduction mechanism of around 80 – 90 %. Interestingly, there is a strong correlation between $\Delta E_{avg,sm}/\Delta E_{pop}$ and ΔE_{pop} which implies that the more efficient the transduction is, the more molecules make use of it. However, there is neither enough data to confirm a general trend nor a microscopic insight to explain this phenomenon.
Second, $\Delta E_{avg,ens}/\Delta E_{pop}$ quantifies how efficient an ensemble measurement would make use of the translation mechanism, i. e. how the presence of donor-only molecules would further reduce the signal.

In summary, the following criteria for a highly sensitive sensor can be proposed:

1. A large separation between the center positions of the low-FRET (apo) and the high-FRET (liganded) state
2. An accumulation in the apo state in the absence of glucose that completely transfers to the high FRET state for glucose saturation
3. A low donor-only fraction

With the help of the smFRET data it is now possible to separately check the fulfillment of the above points. If a constructs shows for example a reasonable large ΔE_{pop} but only a low fraction of the molecules change from the low- to the high-FRET state, this might indicate that the fluorescent proteins hinder the conformational change of the binding domain. A minor change of the sensor layout, e. g. a elongation of the linkers, could already improve the sensitivity. If on the other hand ΔE_{pop} is small, a major revision of the sensor layout, e. g. a change of the fluorescent proteins' attachment position, is most promising. High donor-only fractions indicate a reduced acceptor chromophore maturation which can either originate from incorrect folding or non-ideal cultivation/purification conditions.

4.9.6 Single-Molecule Characterization of Biosensors in Crowding Conditions

In Section 4.6 it was shown that the crowding sensors exhibit a linear increase of intensity ratio R as a response to increasing crowder concentrations. The underlying sensing mechanism, however, remained unclear. In order to get a more detailed picture, smFRET measurements of both constructs were performed in absence, at 10 w/w%, and at 20 w/w% of PEG 6,000. Applying the procedure described in Section 3.3.3 yielded the transfer efficiency histograms presented in Figure 4.19. The histograms are well described by a single Gaussian distribution which continuously shifts towards larger transfer efficiencies with increasing crowder concentrations. Sensor construct G18 shows larger energy transfer efficiencies than construct GE but both sensors behave qualitatively similar (see Tab. 4.3 for fitting parameters). The width of the Gaussian distribution increases slightly for increasing crowder concentrations. However, the shot noise width increases also if the transfer efficiency approaches 0.5 (cf. Eq. 4.16). Comparing the fitted width with the shot noise width indicates an additional, slight broadening for 20 % PEG 6,000 (see Tab. 4.3). A FRET-FCS analysis [126] (data not shown) did not show any dynamics on the time scale faster than the dwell time of a few ms. In summary, both crowding sensor constructs behave rather homogeneously by taking more compacted conformations with increasing crowder concentrations that are static on timescales of milliseconds.

construct	PEG 6,000 [w/w%]	E_1	σ_1	ΔE_{bin}	σ_{sn}	σ_1/σ_{sn}
GE	0	0.115	0.13	0.040	0.050	2.6
GE	10	0.182	0.14	0.050	0.062	2.3
GE	20	0.240	0.17	0.052	0.063	2.7
G18	0	0.357	0.16	0.050	0.073	2.2
G18	10	0.403	0.17	0.040	0.078	2.2
G18	20	0.453	0.20	0.059	0.073	2.7

Table 4.3: Fitting parameters of smFRET efficiency histograms of crowding sensors. E_1: center position of Gaussian distribution; σ_1: width of Gaussian distribution; ΔE_{bin}: bin width of histogram; σ_{sn}: shot noise limited width.

In Section 4.7 it was shown that also the glucose sensor shows a linear increase of R with increasing crowder concentrations. The remaining question is whether crowding has a similar effect like glucose, i. e. a change of population occupancies (see Sec. 4.9.4), or if it causes a shift of the population as observed for the crowding sensor. To access that question, smFRET measurements of glucose sensor no. 2 were performed at various concentrations of PEG 6,000 up to 20 w/w% (see Fig. 4.20). The FRET efficiency histograms were fitted with two Gaussian populations but, in contrast to glucose titration, the fit parameters were free for each PEG concentration. Global fitting approaches fail to describe especially the histogram for 20 w/w% PEG (see App. Fig. A.9). Both populations continuously shift towards higher

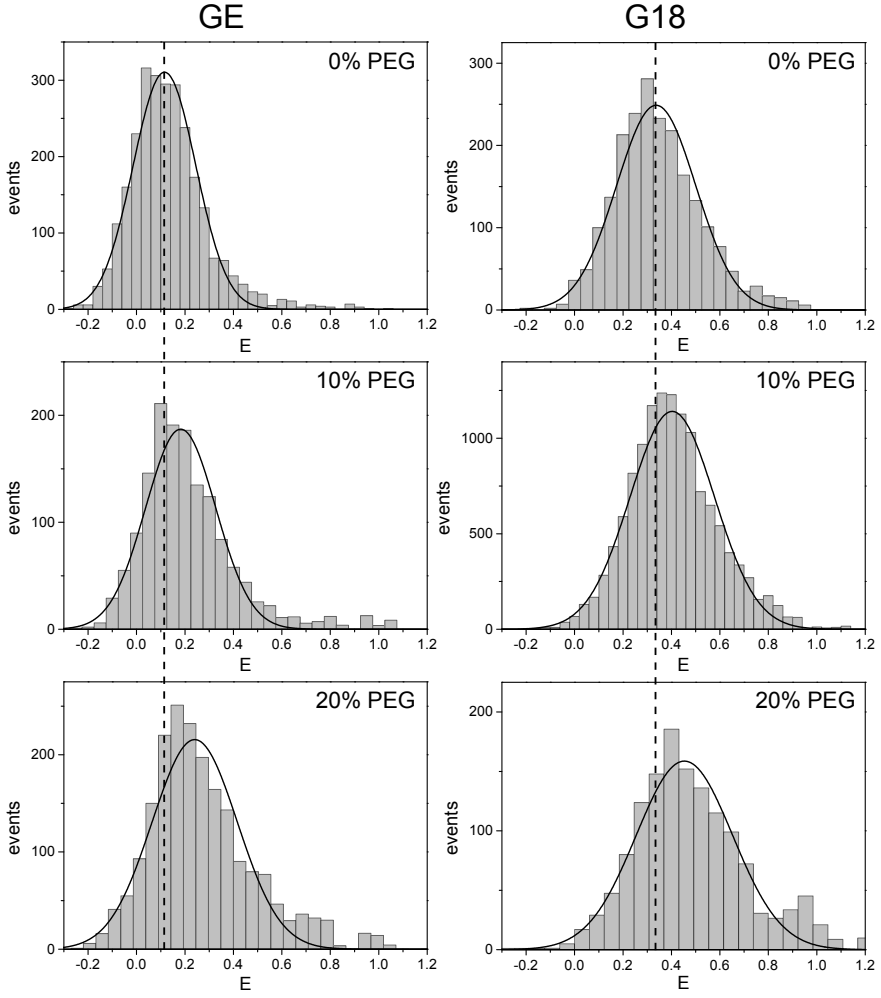

Figure 4.19: smFRET histograms of crowding sensor construct GE (left column) and G18 (right column) in absence of crowding (top row), for 10 w/w% PEG 6,00 (middle row), and for 20 w/w% PEG 6,000 (bottom row). All histograms are fitted with a single Gaussian distribution. The center of the non-crowded population is marked with a vertical dashed line to better notice the shift with increasing crowder concentrations. Adopted from [37].

transfer efficiencies whereas the weighting of each population stays approximately constant

(see Tab. 4.4 for fitting results). Hence, the glucose sensor and the crowding sensor show a qualitatively similar response to crowding.

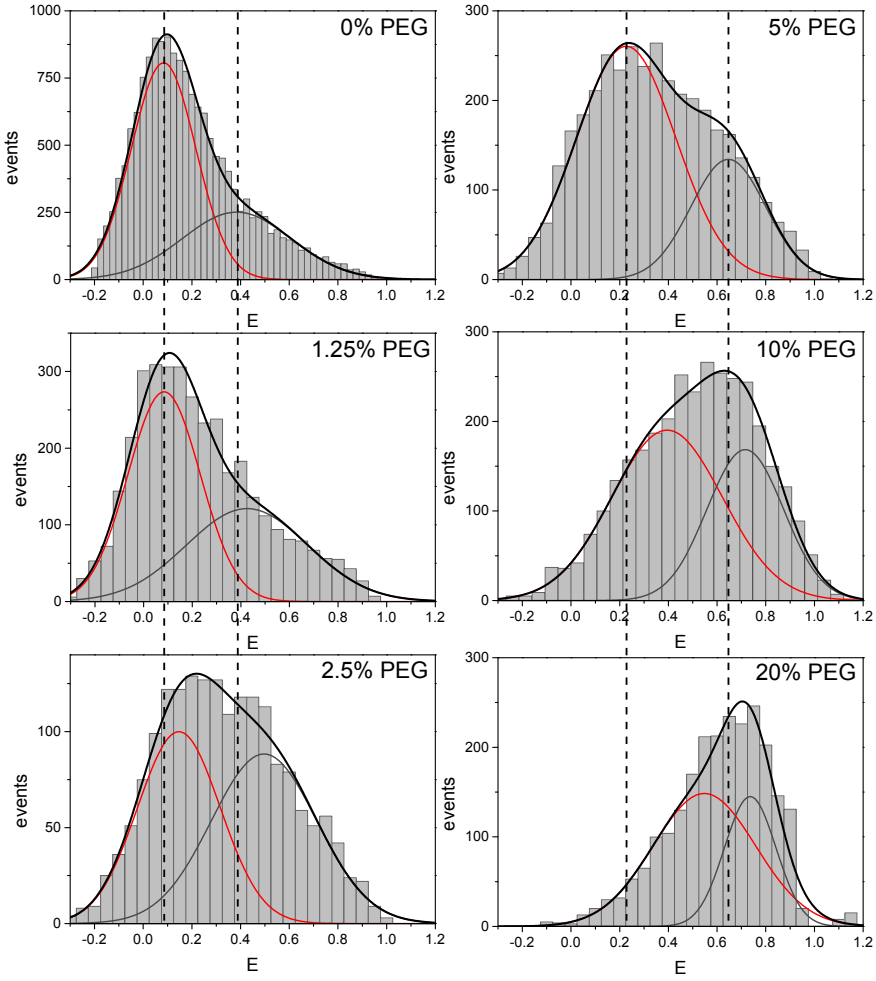

Figure 4.20: smFRET histograms of glucose sensor no. 2 in various concentrations of PEG 6,000. Histograms are fitted individually with a two Gaussian distributions. The mean values of both Gaussian populations are marked for the non-crowded and for 5 w/w% PEG6,000 (upper row) with vertical dashed lines to better notice the shift. Adopted from [37].

Finally, the effects of crowding and glucose sensing were investigated in a combined manner by putting the glucose sensor no. 2 in 10 w/w% of PEG 6,000 and obtaining smFRET histograms in absence, at 1 mM, and at 125 mM of glucose (see Fig. 4.21). Although the isothermal binding curves showed that glucose sensing is still possible in presence of crowding (see Fig. 4.6), a detailed analysis of the single-molecule data was not possible because the smFRET histograms show only minor changes. This is again caused by the non-linear conversion from E to R. Nevertheless, the ensemble measurements indicated a similar sensing mechanism as in the absence of crowding. The histograms were accordingly fitted globally with a two state model (see Tab. 4.4 for fitting results). This interpretation is yet a bit vague and the experiment should be repeated with lower PEG concentrations.

glucose [mM]	PEG 6,000	$\langle E \rangle_{sm}$	E_1	E_2	σ_1	σ_2	p_1	p_2	ΔE_{bin}
0	0 w/w%	0.192	0.084	0.384	0.13	0.22	0.66	0.34	0.025
0	1.25 w/w%	0.228	0.085	0.432	0.15	0.23	0.60	0.40	0.050
0	2.5 w/w%	0.333	0.147	0.496	0.17	0.21	0.47	0.53	0.050
0	5 w/w%	0.348	0.227	0.646	0.20	0.15	0.72	0.28	0.050
0	10 w/w%	0.517	0.395	0.716	0.23	0.15	0.62	0.38	0.050
0	20 w/w%	0.602	0.548	0.736	0.21	0.10	0.67	0.33	0.042
0		0.529					0.27	0.73	0.050
1.1	10 w/w%	0.583	0.292	0.608	0.19	0.19	0.08	0.92	0.025
125		0.587					0.07	0.93	0.020

Table 4.4: Fitting parameters of smFRET histograms of glucose sensor no. 2 in crowding conditions. $\langle E \rangle_{sm}$: mean single-molecule transfer efficiency; E_1, E_2: center position of Gaussian distribution of low FRET and high FRET state; σ_1, σ_2: width of Gaussian distribution of low FRET and high FRET state; p_1, p_2 weighting of Gaussian distribution of low FRET and high FRET state; ΔE_{bin}: bin width of histogram.

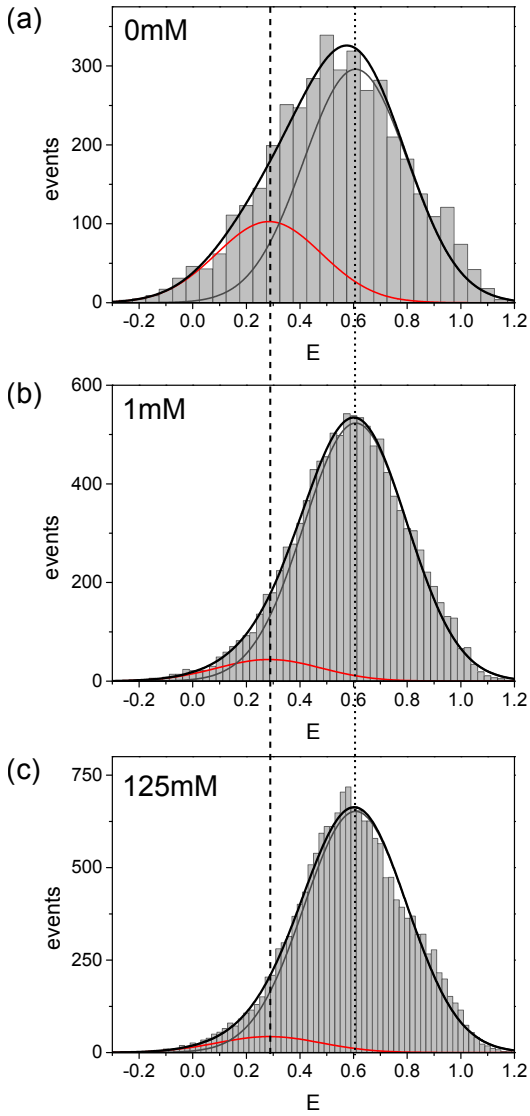

Figure 4.21: smFRET histograms of glucose sensor no. 2 in 10 w/w% PEG 6,000 (a) without glucose, (b) at glucose concentration equal to K_D, and (c) at saturating glucose concentration of 125 mM. Histograms are fitted globally with sum of two Gaussian distributions. Adopted from [37].

4.9.7 Reproducibility and Sample-to-Sample Variations

smFRET measurement of FRET-based biosensors are very time consuming and, hence, systematic repeated measurements were not performed for practical reasons. The reproducibility was exemplarily checked for the glucose sensor construct no. 2. Yet, reproducibility has two aspects: (i) differences in detection caused by the setup and (ii) sample-to-sample variations. The latter point is a common issue when investigating biomolecules. Since biological systems are very sensitive to their environment, the samples of different production batches may show variations in their properties. In addition, the storing conditions may have slightly varied for the different sample batches.

Both aspects of reproducibility were checked in a combined manner by obtaining smFRET histograms for three different batches of glucose sensor no. 2 (see Fig. 4.22). The measurements were conducted with a time lag of several months. In between, the setup was changed to the 481 nm/633 nm configuration and back to the 437 nm/509 nm configuration. The new alignment will cause slightly different detection efficiency that reveal in variations of the correction parameters (see Sec. 4.9.2). The mean of the apo state shifts slightly from $E_1 = 0.092$ for sample #1 to 0.141 and 0.135 for sample #2 and #3, respectively. The population weights are approximately constant and are given by $p_1 = 0.92/0.93/0.94$ for sample #1 to #3.

The minor differences between the histograms demonstrate the reproducibility of the data. It should be noted that a set of single-molecule measurements was always conducted without changing the setup and using the same sensor batch. A 'set of measurements' denotes varying one external parameter like glucose or crowding for a certain sensor construct. Hence, the conclusions drawn from these measurements are not affected by varying detection parameters or sample-to-sample variations.

4.9.8 Consistency of Single-Molecule and Ensemble Data

As shown in the previous sections, single-molecule data of FRET-based biosensors can provide more detailed information than ensemble data. Since this is one of the first comprehensive reports about single-molecule studies with genetically encoded biosensors, the reliability of the approach needs to be demonstrated by relating single-molecule data to ensemble data. Therefore, an ensemble-equivalent intensity ratio R_{conf} is calculated based on the single-molecule data obtained with the confocal microscope and compared to the ensemble R_{spec} obtained with the fluorescence spectrometer. Since the detection efficiency ratio of the confocal setup was determined only for the corrected intensities (see Sec. 4.9.2), the R-value obtained with the fluorescence spectrometer is also corrected for donor crosstalk

$$R_{spec} = \frac{I_A - \left(f_D^A/f_D^D\right) I_D}{I_D} = R - \frac{f_D^A}{f_D^D} = R - 0.392\,, \tag{4.18}$$

where f_D^A and f_D^D are intensities of the area-normalized donor emission spectrum at the acceptor and donor peak wavelength, respectively (see Fig. 4.8).

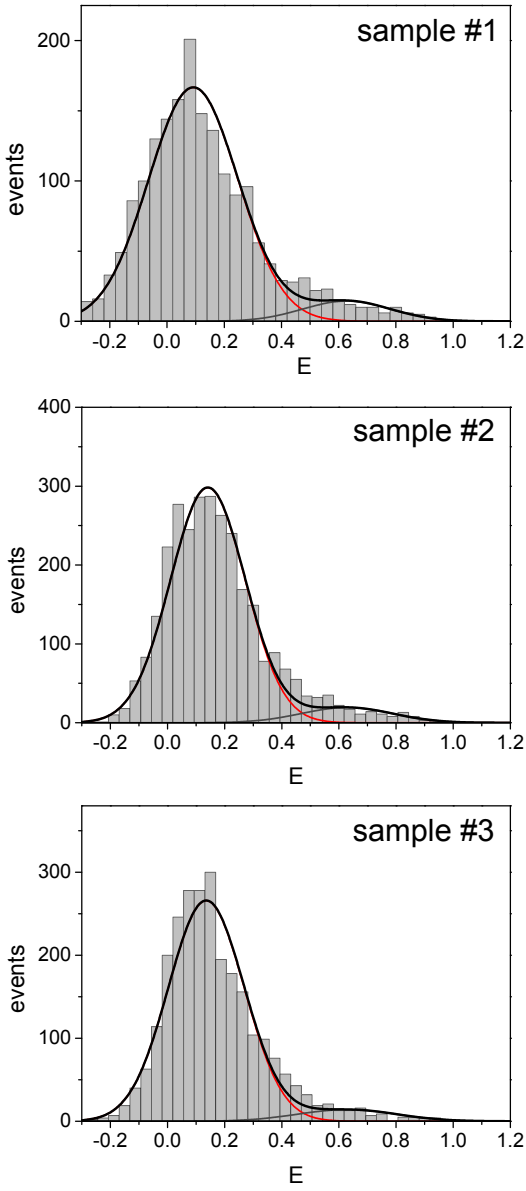

Figure 4.22: Three independent measurements of smFRET histograms of glucose sensor no. 2 in absence of glucose. The histograms are fitted individually with two Gaussian distributions where the mean of the second distribution is fixed $E_2 = 0.628$ according to the results obtained in Section 4.9.4. Sample #1 is identical to the sample presented in Figure 4.16. Adopted from [37].

The ensemble-equivalent R value of the single-molecules data was calculated by converting the integrated intensities to peak intensities, correcting for different detection efficiencies, and accounting for a donor-only fraction by

$$R_{conf} = (1 - x_{D0}) \frac{g_D}{g_A} \frac{f_A^A}{f_D^D} \frac{F_A}{F_D}, \tag{4.19}$$

where x_{D0} is the donor-only fraction, $g_D/g_A = \gamma^{-1}\Phi_A/\Phi_D = 0.462$ is the detection efficiency ratio of donor and acceptor, f_A^A is the peak-to-area ratio of the acceptor emission spectrum at the maximum, and F_D and F_A are the corrected, burst-averaged intensities of donor and acceptor, respectively.

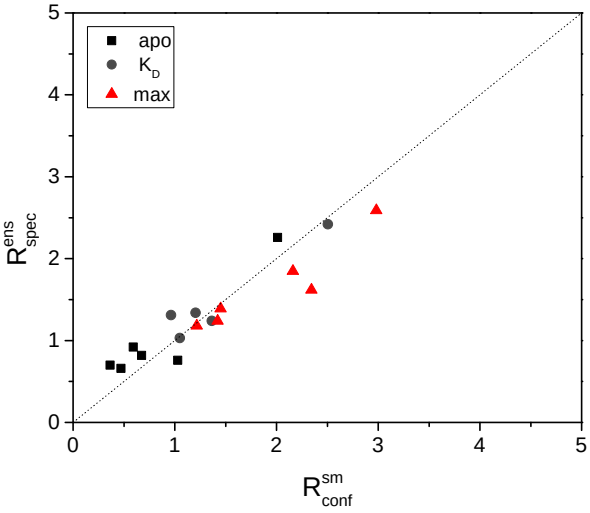

Figure 4.23: Intensity ratio R_{spec}^{ens} obtained with the emission spectrometer at ensemble level is compared to ensemble-equivalent intensity ratio R_{conf}^{sm} that is calculated based on the single-molecule data obtained with the confocal microscope. Adopted from [37].

A comparison of R_{spec} and R_{conf} for the glucose sensor (see Fig. 4.23) shows a reasonable identity of both quantities. The noticeable spreading around the bisecting dashed line is most probable related to a varying detection efficiency ratio. The confocal microscope was regularly changed between a 481 nm/633 nm and the 437 nm/509 nm configuration. A new alignment will result in slightly different detection efficiencies which will cause the spreading because not all experiments were performed with the same alignment. Data that was acquired with the same alignment showed a much better consistency.

4.10 Comparison of Fluorescent Protein-Equipped Versus Dye-Labeled Biosensors

The performance of different glucose sensor constructs and the response to crowding can be well studied with single-molecule experiments as shown in the previous Section 4.9. Yet, one might wonder whether the extensive sensor optimization and the time-consuming single-molecule characterization is actually necessary, because at least the glucose sensor should be applied *in vitro*. If the genetically encoding is not required, one might attach a dye FRET pair to the sensing domain instead of fluorescent proteins (FPs). Fluorescent dyes will generally provide a brighter signal and better photostability. Hence, this section deals with the development of a dye-labeled glucose sensor and the question whether it is possible to achieve a similar sensitivity as for the FP-equipped sensor. It is furthermore investigated if the dye-labeled sensor shows similar response to glucose and crowding as the FP-equipped analogue.

4.10.1 Accessible Volume Calculation for Dye Attachment to Glucose Binding Protein MglB

The dyes were bound to the glucose binding protein MglB by using maleimide functionalized dye linker that bind to the sulfur atom of a cystein residue. The labeling positions need to be (i) located at peripheral regions of MglB that are non-crucial for the structural integrity and function of the protein, e. g. at a loop, and (ii) the inter-dye distance should be close to the Förster radius R_0 to be sensitive to distance changes. The employed dye pair Alexa 488/Alexa 647 has a Förster radius of R_0 = 54.5 Å [13]. The dyes contain a C6-amino linker which provides a high rotational mobility that allows $< \kappa^2 >= 2/3$ dynamic averaging. The linker provide simultaneously also a translational mobility which will lead to a different inter-dye distance than the distance between the attachment points. Here, accessible volume calculations have proven to be a useful tool to predict the averaged inter-dye distance [127]. Briefly, the linker is modeled as a flexible tube and the dye as a sphere (see ref. [36] for geometrical parameterization). An algorithm calculates all dye accessible points that can be reached by the linker without any steric clashes of the linker or the dye itself. The resulting cloud of points represents the accessible volume of each dye (see Fig. 4.24). The mean inter-dye distance R_{DA} is calculated by averaging over all possible distance combinations [128]. In order to judge if a certain dye attachment results in a distinct distance change, the mean inter-dye distance was calculated using the Protein Data Bank (PDB) structures of the apo state (PDB entry: 2FW0) and the liganded state (PDB entry: 2FVY) of MglB. The FRET efficiencies that correspond to the calculated R_{DA} were calculated by Equation 3.11 with R_0 = 54.5 Å. A comparison of different combinations of attachment positions revealed that the attachment to residues 42 and 137 gave the largest difference in FRET efficiencies (see Tab.4.5). Despite extensive search it was not possible to find attachment points that result in inter-dye distances closer to R_0 and yield a larger distance change between the apo and glucose-bound state.

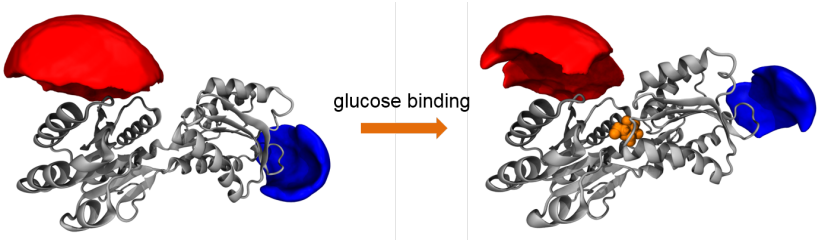

Figure 4.24: Visualization of donor (blue) and acceptor (red) AV clouds in open (left) and closed (right) conformation of MglB. Adopted from [13].

MglB state	R_{DA}	E
glucose-free (PDB: 2FW0)	65 Å	0.27
glucose-bound (PDB: 2FVY)	58 Å	0.40

Table 4.5: AV parameter of MglB for dye attachment to residues 42 and 137.

4.10.2 Single-Molecule Characterization of Dye-Labeled Glucose Biosensor

The experimental single-molecule characterization of the dye-labeled glucose sensor was similar to that used for the fluorescent protein-equipped sensor, i. e. a smFRET histogram was generated in absence of glucose, at the sensor's K_D, and at saturating glucose concentrations (see Fig. 4.25). In addition, several other glucose concentrations in between were investigated. The data was obtained by Michele Cerminara. The resulting smFRET histograms in absence of glucose and at saturation glucose concentration were fitted with a single Gaussian distribution and are in good agreement with the transfer efficiencies predicted by the accessible volume (AV) calculation. All other smFRET histograms were fitted with a linear combination of these distributions with only the relative weights as fitting parameters (see Tab 4.6 for fitting parameters). This fitting approach assumes a two state model which is a reasonable assumption but cannot be directly resolved in the smFRET histograms because the transfer efficiencies of the apo and the saturated state are too close to each other. In fact, the smFRET histograms show apparently only a shift of the population.
Plotting the fraction of the glucose-saturated state as a function of glucose concentration yields a sigmoidal binding curve similar to that of the FP-equipped sensor (cf. Fig. 4.26 and 4.4). The increase of the saturated fraction can be fitted in analogy to Equation 4.2 with the apo and max values fixed to zero and one, respectively. It turns out that the obtained K_D = 0.9 μM of the dye-labeled sensor is only slightly larger than that of the wild-type MglB which is 0.2 μM [129]. It has been reported that the apparent affinity of other dye-labeled sensors is also in the μM-range but can also vary [130]. However, the K_D of the FP-equipped biosensors is around 1 mM, three orders of magnitude higher than that of the dye-labeled sensor. It has been shown that the affinity of FP-equipped sensors depends strongly on the

sensor design and is in the range of μM – mM [26]. A possible explanation for the generally lower affinity of FP-equipped sensors might be either that the fluorescent proteins hinder the diffusion of glucose molecules towards the binding site or the attachment of fluorescent proteins induces mechanical strain to MglB that slightly changes the conformation of the binding pocket and therefore lowers the affinity to glucose.

glucose	PEG 6,000 [$w/w\%$]	E_1	E_2	σ_1	σ_2	p_1	p_2
0 μM		0.29	-	0.09	-	1	-
1 μM	-	0.29	0.39	0.09	0.09	0.47	0.53
100 mM		-	0.39	-	0.09	-	1
-	10 w/w%	0.29	-	0.10	-	1	-

Table 4.6: Fitting results of smFRET histograms of dye-labeled glucose sensors.

Next, the response of the dye-labeled sensor to macromolecular crowding was investigated. A crowder concentration of 10 w/w% of PEG 6,000 was used that resulted in a considerable shift of the FRET efficiency for the FP-equipped sensor (see Fig. 4.20). In contrast, the FRET efficiency histograms of the dye-labeled sensor in absence and presence of crowding are indistinguishable (cf. upper and lower panel in Fig. 4.25). This reveals that the glucose binding protein itself is not compacted by crowding and, hence, the crowding response of the FP-equipped sensor is solely caused by the presence of the fluorescent proteins.

In summary, despite extensive efforts it was not possible to design a dye-labeled glucose sensor that reaches similar sensitivity as the FP-equipped glucose sensor. The highest possible shift of the transfer efficiency for the dye-labeled sensor is $\Delta E_{pop} = 0.10$ whereas the best FP-equipped sensor construct showed $\Delta E_{pop} = 0.54$ (see Tab. 4.2). However, the dye-labeled sensor shows no sensitivity to crowding. The surprising conclusion of this observations is that one has to question the generally accepted scope of applications. Due to their high sensitivity, FP-equipped biosensors show the best potential for *in vitro* applications. On the other hand, dye-labeled sensors offer a better reliability for *in vivo* applications due to their insensitivity to crowding. Of course, one has to deal with a reduced signal sensitivity but the application of FP-equipped sensors in crowded environments can lead to a fatal misinterpretation of the signal (see Sec. 4.7). For completeness, it has to mentioned that the incorporation of dye-labeled sensors into living cells, e. g. by microinjection [113], is challenging.

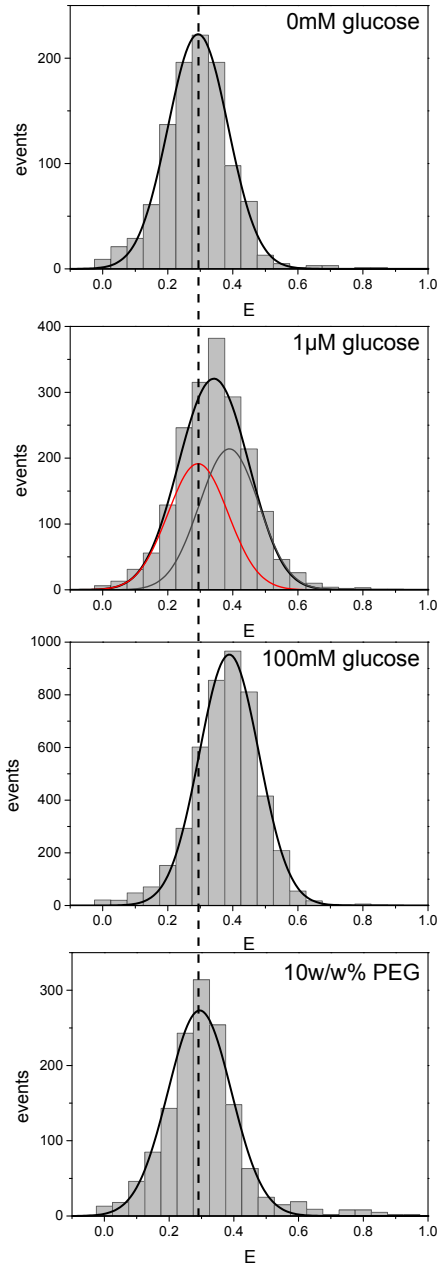

Figure 4.25: smFRET histogram of dye-labeled glucose sensor in absence of glucose, at glucose concentration equal to K_D (1 μM), at saturating glucose concentration of 100 mM, and for 10 w/w% PEG 6,000. Adopted from [13].

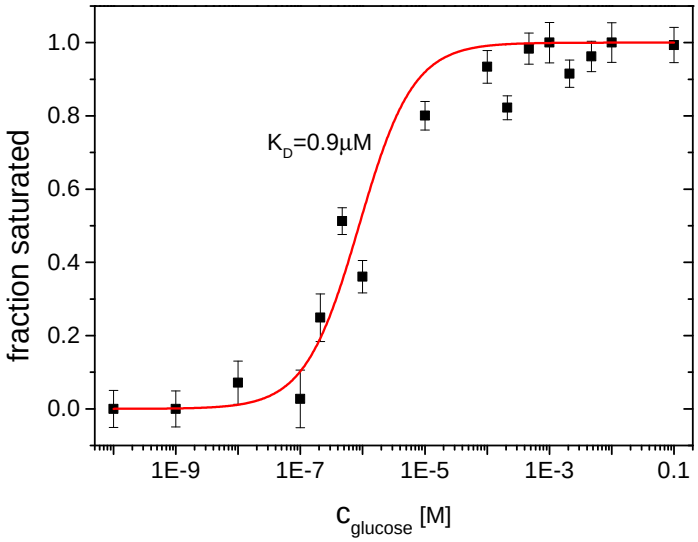

Figure 4.26: Fraction of glucose-saturated population in smFRET histogram of dye-labeled sensor as a function of glucose concentration. Isothermal binding curve is fitted in analogy to Equation 4.2. Adopted from [13].

5 Brightness-Gated Two-Color Coincidence Detection (BTCCD)

5.1 Introduction to Two-Color Coincidence Detection

A biological cell is composed of a multitude of different biomolecules. However, the simple presence of these individual biomolecules does not create life, it is their interaction. One of the most crucial properties of biomolecules is, hence, the ability to recognize and specifically interact with each other. This interaction is frequently a binding between two or more biomolecules. Thereby, a molecular complex is formed which is in most cases associated with a biological function [131].
One example of a cellular process that relies on the binding of biomolecules is the formation macromolecular machines, e. g. ribosomes, which consists of two subunits which in turn are built from numerous proteins and RNA [132]. Apparently, the binding affinities of the interaction partners as well as the presence of co-factors regulate the occurrence of the functional complex. In the case of ribosomes this regulates consequently the overall protein biosynthesis.
A second example for the importance of binding for biological functions is (intra-) cellular signaling. Although there is no general mechanism, signaling commonly occurs by binding of a 'signaling molecule' to a receptor molecule which either activates a transducer molecule or directly initiates a signaling cascade [132].

But how can the binding of two biomolecules be measured? There are various biochemical/biophysical methods to do so like electrophoresis [133], surface plasmon resonance [134], or calorimetric approaches, e. g. isothermal titration calorimetry [135]. In contrast to elec-

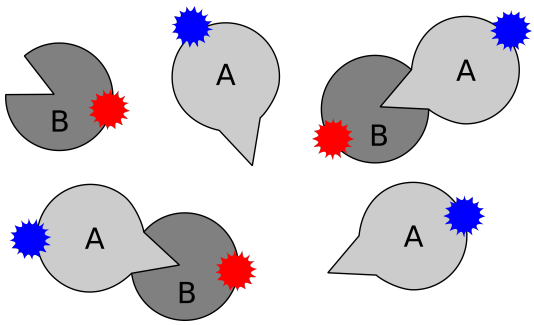

Figure 5.1: Fluorescence assay to investigate binding of biomolecules.

trophoresis and surface plasmon resonance which are both sensitive to a change in the mass of the molecule (complex), isothermal titration calorimetry directly measures the heat that is generated due to the binding.
Yet, fluorescence based methods have proven to be beneficial due to the high specificity, sensitivity and versatility of fluorescence assays. Figure 5.1 illustrates the concept of fluorescence-based assays to investigate the binding of two molecules A and B. Molecule A is labeled with a blue fluorescent dye while its binding partner molecule B is labeled with a red fluorescent dye. Without any interaction between both molecules, blue and red fluorescence will occur independently of each other. If molecule A and B bind, the molecular complex will show fluorescence of both colors simultaneously. Other combinations of dyes are of course also possible if their emission can be sufficiently separated.
There are several methods to investigate the presence of the dual-labeled complex. For single molecules that are immobilized on a cover slip, one can study the co-localization of blue and red spots using wide field [136] or total internal reflection microscopy [137]. However, the presence of the glass surface and interaction with the anchor molecules that are used to tether the molecules to the cover slip might change the binding characteristics.
For confocal microscopy of freely-diffusing molecules this problem resolves. Here, the most obvious approach is probably to use correlation techniques such as fluorescence cross correlation spectroscopy (FCCS) [138] because the dual-labeled complex will lead to a cross correlation of the occurrence of blue and red fluorescence. However, the quantitative analysis of FCCS experiments is in practice challenging because it depends on various calibration steps and the selected fitting model [33]. Alternatively, one can utilize the occurrence of FRET as a probe of binding [139]. However, this requires that the distance between the dyes in the bound state is short enough to enable FRET to occur. The most direct approach is to look for coincidence of blue and red fluorescence in a single-molecule experiment. This approach is termed two-color coincidence detection (TCCD) [34].

An accurate, quantitative coincidence detection requires certain experimental conditions that have to be fulfilled, i. e. (i) the label ratio of each binding partner should be 100% or at least its value should be known and (ii) fluorescence bursts must be reliable identified for each color. Both aforementioned issues are covered in the following sections.

5.2 Imperfect Overlap of Confocal Volumes Causes Underestimated Coincidence

The major prerequisite for a quantitative coincidence analysis is the ability to detect the fluorescence of both emitters with a similar probability. This does not mean that both detection efficiencies have to be identical. It rather implies that if the fluorescence of a dual-labeled molecule is detected for one color it should be definitely detected also for the other color and vice versa.

For dual-color confocal microscopy, this implies that the overlap of the MDFs should be maximized. Two effects can occur that reduce this overlap. First, both confocal volumes differ in size which is a direct consequence of the diffraction limit. Second, there can be a relative shift between both volumes due to chromatic aberrations. The presence of both effects was

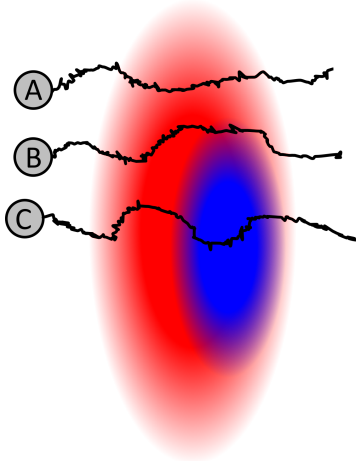

Figure 5.2: Schematics of mismatch of blue and red confocal volume and example of borderline (A) , peripheral (B), and central trajectory (C). Adopted from [140].

verified for the employed setup by dual-color raster imaging of fluorescent beads (see App. Fig. B.1). The imperfect overlap of both confocal volumes leads to a trajectory-dependent burst detection efficiency that differs for both colors. Hence, the prerequisite of similar detection efficiencies is not fulfilled because there are trajectories that just penetrate one of the confocal volumes. Figure 5.2 illustrates this situation. The red confocal volume is larger than the blue confocal volume and both volumes are shifted with respect to each other. Exemplarily, three trajectories through the confocal volumes are depicted; borderline trajectories that only touch the red volume at the edge (trajectory A), peripheral trajectories that penetrate the outer part of the red volume and may eventually touch the blue volume (trajectory B), and central trajectories that penetrate both, red and blue, confocal volumes centrally. Figure 5.3 shows how the appearance of fluorescence bursts depends on the trajectory of the molecules. The data was obtained for a 100% dual-labeled nano-bead reference (see Sec. 5.5.2). A single-molecule transit is detected as a drop of the IPL time trace below the burst threshold (see dotted and dashed line for blue and red channel, respectively). Three bursts are visible that correspond to the trajectories depicted in Figure 5.2. Trajectory A just leads to a detection of a dim burst in the red channel. However, the blue IPL trace is not dropping below the burst threshold and, hence, no burst in the blue channel is detected. If the molecule trajectory is starting to touch also the blue volume (trajectory B), also the blue IPL time trace is shortly dropping below the burst threshold. For a central trajectory (trajectory C), a distinct burst in both channels is apparent. A coincidence analysis would yield that burst A was not coincident but only red, and bursts B and C were coincident. Physically, the sample is completely dual-labeled and, hence, the coincidence would be underestimated.

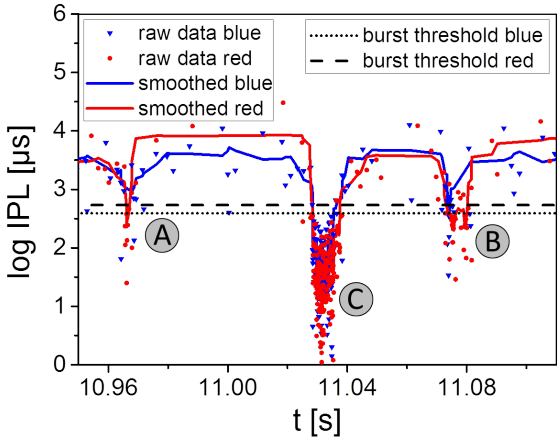

Figure 5.3: Illustration of bursts that correspond to borderline (A) , peripheral (B), and central trajectories (C) (see Fig. 5.2).

This underestimation of coincidence can be avoided if only central trajectories (trajectory C) are selected for the analysis and trajectories of kind A and B are discarded. Trajectory B should also not be used for the analysis because the burst in the blue channel is only very dim and small changes, e.g. changing the burst threshold or the IPL smoothing parameter, can strongly affect the results of a coincidence analysis. Selecting only central trajectories leads to quantitative and robust coincidence detection.

5.3 Basic Idea of Brightness Gating

In the previous section it was recognized that for a quantitative coincidence analysis it is necessary to solely select central trajectories that traverse the overlap region of the confocal volumes. However, it was not discussed which parameter is suitable to do so. Possible parameter are the dwell time in the confocal volume, i. e. the time the IPL time trace stays below the burst threshold (see Fig. 5.3), or the burst intensity given in number of photons. Another option would be to use the IPL itself or the molecular brightness, i.e. the number of photons normalized to the dwell time.

Figure 5.4 shows the distribution of burst intensities (photons per burst) for the nanobead reference (see Sec. 5.5.2). Bursts that consist of only a few photons are very frequent and correspond to borderline trajectories (trajectory A in Fig. 5.2). Accordingly, peripheral (trajectory B) and central (trajectory C) trajectories are rather rare. The burst intensity is thus well suited to select central trajectories because it is easily accessible from the data (without any post-processing) and there is obviously a clear relation between the trajectory

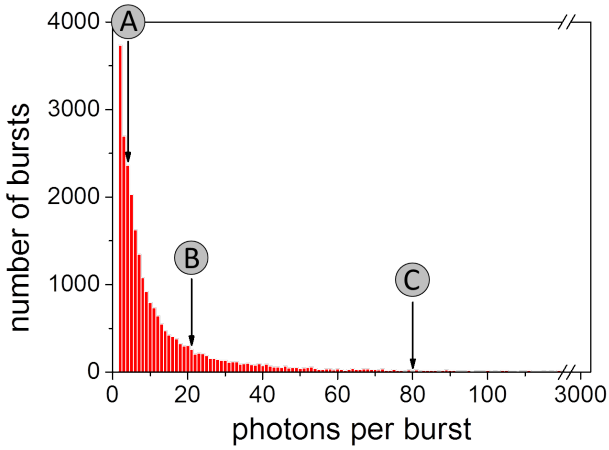

Figure 5.4: Distribution of burst brightness of red channel for nano-bead reference. Distribution of blue channel looks similar and can be found in Appendix Figure B.2. Adopted from [140].

and the burst intensity. In addition, central trajectories lead to an increased burst intensity in comparison to peripheral trajectories with the same dwell time because the molecular detection function is maximal at the center of the detection volume (see Sec. 3.2.2). The basic idea of brightness-gated two-color coincidence detection is to select only bright bursts for the coincidence analysis because they correspond to central trajectories.

5.4 Implementation of Brightness-Gated Two-Color Coincidence Detection

The practical implementation of brightness-gated two-color coincidence detection is based on two thresholds: (i) the *burst threshold* is used to discriminate a single-molecule fluorescence burst against the background and (ii) the *brightness threshold* selects only bursts that contain more photons than the threshold value. Subsequently, the coincidence of all bright bursts in one channel to all burst in the other channel, and vice versa, is calculated. Two bursts are considered to be coincident if the start or end time tag of one burst lies within the start and end time of the other burst. The algorithm of BTCCD is illustrated in the flowchart in Figure 5.5. The brightness threshold n_{br} is continuously increased and the fraction of coincident bursts is calculated by

$$f_{RB}(n_{br}) = \frac{N_{RB}(n_{br})}{N_R(n_{br})}\,, \tag{5.1a}$$

$$f_{BR}(n_{br}) = \frac{N_{BR}(n_{br})}{N_B(n_{br})}\,, \tag{5.1b}$$

where f_{RB} and f_{BR} are the fractions of coincident bursts in the red and blue channel, N_{RB} and N_{BR} are the number of coincident bursts in the red and blue channel, and N_R and N_B are the total number of selected red and blue bursts, respectively.

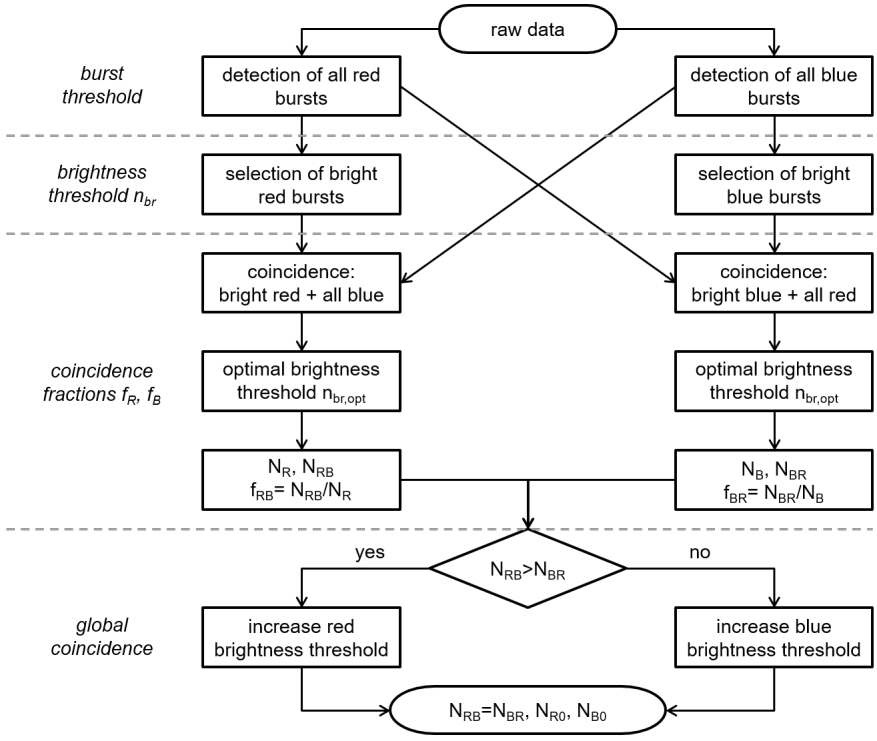

Figure 5.5: Workflow of brightness-gated two-color coincidence detection. Adopted from [140].

It is difficult to tell a priori how large the brightness threshold should be chosen in order to sufficiently exclude all peripheral trajectories. Therefore, the coincidence fractions in Equations 5.1a and 5.1b are plotted as a function of the brightness threshold. Figure 5.6 shows the dependency of both coincidence fractions on the brightness threshold for the nano-bead reference (see Sec. 5.5.2). The brightness threshold is normalized to the mean number of

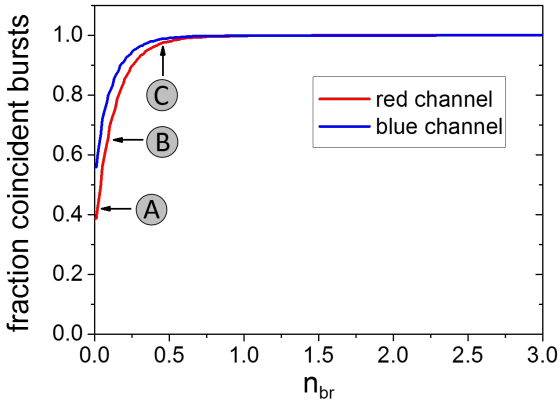

Figure 5.6: Coincidence fractions of nano-beads as a function of brightness threshold. Adopted from [140].

photons for all burst of the respective channel. This scaling scheme makes a comparison of both channels and a comparison to other samples easy. Both coincidence fractions show a steep increase for low brightness thresholds ($n_{br} < 0.2$) which diminishes for intermediate brightness thresholds ($0.2 < n_{br} < 0.7$) and, finally, turns into a plateau for large brightness thresholds ($n_{br} > 0.7$). These three brightness threshold regimes can be related to the trajectories in Figure 5.2. For low brightness thresholds the bursts are dominated by borderline trajectories (cf. occurrence of trajectories A, B and C in Fig. 5.4). Hence, the fraction of red coincident bursts is very low ($f_{RB}(n_{br} = 0) \approx 0.4$). The coincidence fraction is not zero because all type of trajectories are analyzed. However, if the brightness threshold is increased, more and more borderline trajectories (trajectory A) are excluded from the coincidence analysis which leads to the steep increase of the coincidence fraction. Finally, larger brightness thresholds also exclude all peripheral trajectories (trajectory B) and only central trajectories (trajectory C) enter the coincidence analysis. This central trajectories have always on overlap with the blue confocal volume. Thus, a further increase does not change the coincidence fraction which leads to a saturation of the coincidence fraction and the appearance of the plateau. Note, that the blue coincidence fraction shows a similar behavior but differs in the absolute value of coincidence. The red confocal volume is usually larger than the blue one. Consequently, there are more trajectories that touch the red volume and not the blue volume than, vice versa, trajectories that touch the blue volume and not the red one. The initial value of the red coincidence fraction is thus much lower than that of the blue coincidence fraction. The fact that the blue coincidence fraction is increasing at all, indicates that there is a pronounced shift between the red and blue confocal volume. Only if some part of the blue confocal volume juts out of the red confocal volume there are trajectories that are within the blue volume and not the red one.

In summary, sufficiently large brightness thresholds lead to saturated coincidence fraction. How large the brightness threshold is optimally chosen is discussed in the following section.

5.4.1 Determination of Optimal Brightness Threshold

The brightness threshold should be large enough to exclude all peripheral trajectories which reveals in a saturation of the coincidence fraction (see Sec. 5.4). However, it cannot be chosen arbitrarily large because at some point it would exclude all detected single-molecule events. Additionally, increasing the brightness thresholds decreases the precision because less molecules enter the calculation. The relative precision of the coincidence fractions (see Eqs. 5.1a, 5.1b) is given by

$$\left(\frac{\sigma_f}{f}\right)^2 = \left(\frac{\sigma_{N_c}}{N_c}\right)^2 + \left(\frac{\sigma_N}{N}\right)^2, \tag{5.2}$$

where f is the coincidence fraction, N is the number of selected bursts and N_c is the number of coincident bursts.
Assuming a Poisson distribution for the number of bursts, i. e. errors are given by the square root of number of bursts, and rearranging Equation 5.2 leads to

$$\frac{\sigma_f}{f} = \sqrt{\frac{1}{N_c} + \frac{1}{N}}. \tag{5.3}$$

As already mentioned, the best guess for the true value of the coincidence fraction is reached for the largest brightness threshold. Accordingly, the relative accuracy is defined as the difference to the coincidence ratio of the highest brightness threshold

$$\frac{\Delta_f}{f} = \frac{f_{high} - f}{f} \tag{5.4}$$

where f_{high} is the coincidence fraction of the highest brightness threshold.
The optimal brightness threshold is reached when a gain in accuracy due to an increase of the brightness threshold is overcompensated by a loss in precision. In practice, the optimal brightness threshold is determined individually for each channel by plotting the relative precision (Eq. 5.3) and relative accuracy (Eq. 5.4) and determining their intersection as shown in Figure 5.7.

The definition of accuracy in Equation 5.4 requires a careful selection of the highest brightness threshold. On the one hand it needs to be high enough to ensure that the plateau is reached. On the other hand it should not be too high because the coincidence fraction is then fluctuating a lot due to the low precision. In addition, the presented approach to determine the optimal brightness threshold leads to a systematic underestimation of the coincidence fractions.

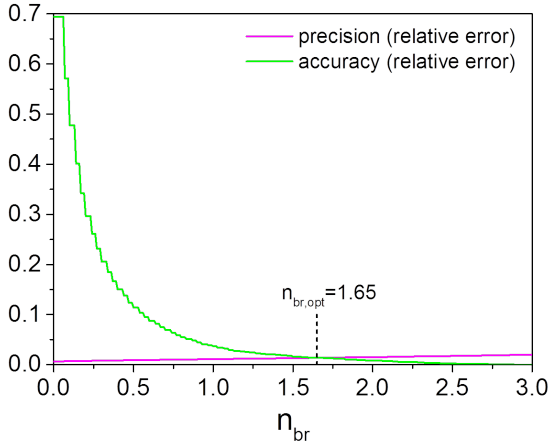

Figure 5.7: Determination of optimal brightness threshold as intersection of relative precision and accuracy. Data shown for red channel of nano-bead reference. Same analysis for blue channel can be found in Appendix Figure B.3.

5.4.2 Fitting of Coincidence Fraction Curves

An alternative approach to determine the saturated coincidence fraction is to fit the coincidence fraction curves with a suitable function. This function should exhibit a strong increase for low brightness thresholds and a saturating behavior for large brightness thresholds. A phenomenological comparison reveals that a bounded exponential function is well suited to describe the coincidence fractions. The coincidence fractions can be fitted by

$$f(n_{br}) = f_{sat} - \Delta f \; e^{-n_{br}/n_{1/2}} \tag{5.5}$$

where f_{sat} is the saturated coincidence fraction, Δf is the increase of the coincidence fraction, and $n_{1/2}$ is the half-value brightness threshold.
A fit of the coincidence fractions is exemplarily shown for the nano-beads in FIgure 5.8. The fitting parameters of all samples can be found in the Appendix Tables B.1 and B.2.

5.4.3 Global Coincidence Analysis

In many applications it is sufficient to determine the coincidence of one color to the other color, e. g. to characterize the molecular binding or interactions. However, there are situations where the total ensemble of molecules should be characterized. The characterization includes the quantification of molecules that show only blue fluorescence (N_{B0}), only red fluorescence (N_{R0}) or fluorescence of both colors (N_{BR}, N_{RB}). Since in BTCCD two brightness thresholds are used for the coincidence analysis, there are also two coincidence values,

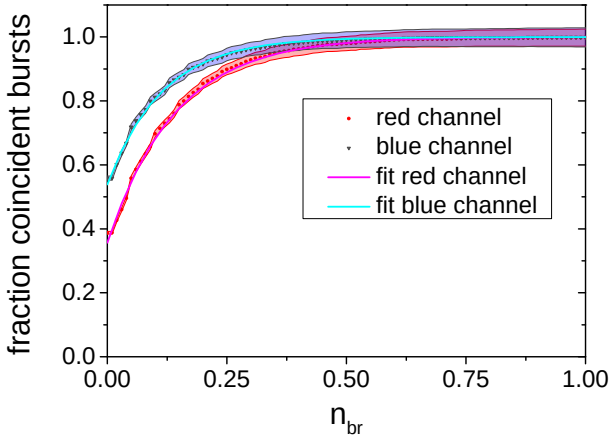

Figure 5.8: Fitting of coincidence fractions of nano-bead reference.

i. e. the fraction of coincident blue bursts with respect to all selected blue bursts and, accordingly, the fraction of coincident red bursts with respect to all selected red bursts. However, the number of coincident bursts is not necessarily equal for both colors because different subensembles of all detected bursts were selected to characterize the ensembles of red and blue labeled molecules. In the picture of trajectories, these are different sets of trajectories.

The idea of a global coincidence analysis is to obtain the same number of coincident bursts for both colors, i. e. $N_{BR} = N_{RB}$. The general procedure is shown in Figure 5.5 and illustrated using the data obtained for the single dye dsDNA reference in Figure 5.9. The starting points for the global coincidence analysis are the optimal brightness thresholds of the individual channels (see Sec. 5.4.1). Subsequently, the brightness threshold of the color that shows the larger number of coincident bursts is increased until the number of coincident bursts equals that of the other color. Increasing the brightness threshold is only reducing the total burst number but is not remarkably changing the coincidence fraction because it saturated. Finally, the number of coincident red bursts N_{RB} and coincident blue bursts N_{BR} equal, and the number of only red N_{R0} and only blue bursts N_{B0} can be calculated (see Fig. 5.9).

An example where a global coincidence analysis is relevant is given by FRET-based biosensors (see Sec. 5.9). Here, the global fraction of dual-labeled biosensors matters as single-labeled sensor molecules reflect waste products in the biotechnological context.

5.5 Reference Samples

The capabilities of BTCCD can be evaluated by means of reference samples. A reference sample has to have a well-defined fraction of dual-labeled molecules that is a priori known

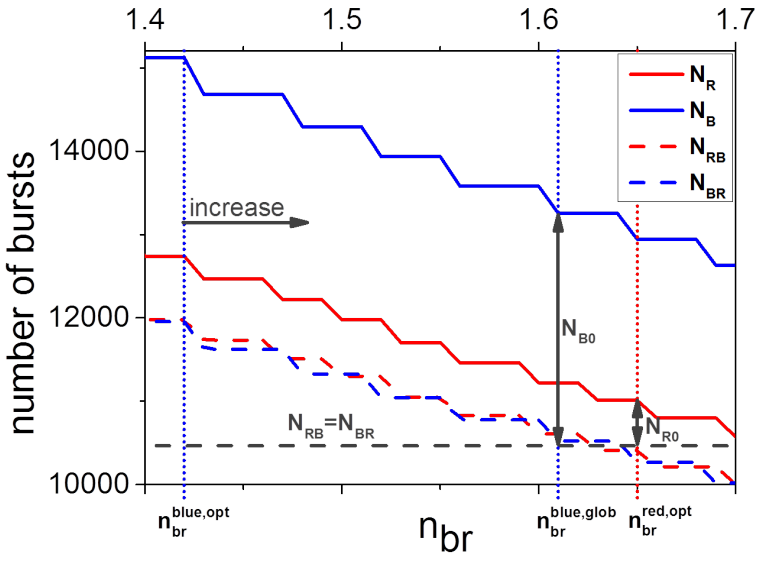

Figure 5.9: Procedure of global coincidence analysis. The number of coincident bursts at the optimal brightness threshold is compared. The brightness threshold of the channel that results in the larger number of coincident burst (here blue) is increased until the number of coincident bursts is equal for both channels ($N_{RB} = N_{BR}$). The number of single labeled molecules is given by the difference to the total number of burst in the respective channel (indicated by gray arrows).

and/or can be determined independently. The most obvious approach is to have 100 % of dual-labeling because this can be verified with independent ensemble measurements like absorption spectroscopy. If the dual-labeling ratio would be below 100 %, absorption spectroscopy can reveal the individual concentrations of the fluorophores but it would be unclear how they distribute among the molecules.

A reliable approach to achieve full dual-labeling is to label each reference molecule with multiple dyes. The reference molecules should exhibit a homogeneity in size and for the number of labeling sites. Still, the number of fluorophores per molecules will exhibit a certain distribution but if the mean number of fluorophores is sufficiently large, it can be neglected that the molecule is not even labeled with a single fluorophore.

In this section different reference samples are utilized where the number of fluorophores per molecules is systematically reduced. First, TetraSpeck beads that carry a large number of dyes (≈ 100) are used as a reference (see Section 5.5.1). In the following, a custom-made DNA origami sample is used where the number of dyes is reduced to only a few (see Section 5.5.2). Consequently, the number of dyes is reduced to a single copy of each color using DNA

oligonucleotides and the impact a different dye combinations is investigated (see Sections 5.5.3 and 5.5.4).

5.5.1 TetraSpeck Beads

TetraSpeck beads consist of polystyrene spheres with a diameter of $100nm$ that are decorated with hundreds of dyes in four spectral regions. The high labeling ratio guarantees full coincidence and very bright fluorescent bursts in a single-molecule experiment. Figure 5.10 shows the corresponding coincidence fractions. As expected, both coincidence fractions reach 100 % after a steep increase for low brightness thresholds.

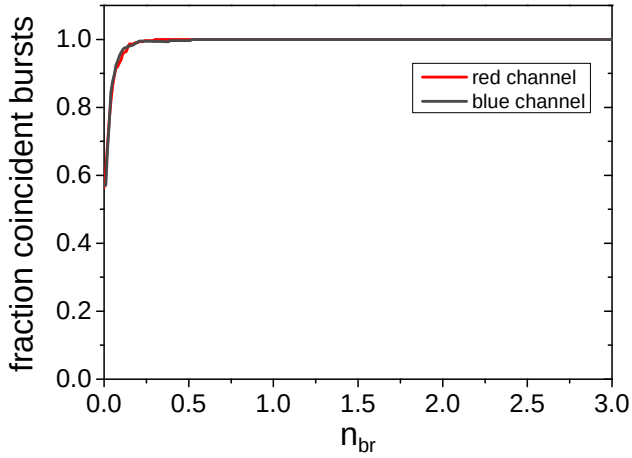

Figure 5.10: Coincidence fractions of TetraSpeck beads as a function of brightness threshold. After a steep increase for low thresholds both colors show full coincidence.

Although the coincidence reaches 100 % and it would remarkably underestimated without brightness gating. TetraSpeck beads have some drawbacks as reference samples. First, fundamental parameter like the diffusion coefficient or the molecular brightness are much different in comparison to the samples of interest. The diffusion coefficient of TetraSpeck beads was determined with FCS to be 2.28 $\frac{\mu m^2}{s}$ which is at least one order of magnitude smaller than that of the samples of interest. Due to the high labeling ratio the excitation powers have to be chosen approximately two orders of magnitude lower than for single dye labeled samples in order not to saturate the detectors. Owing to the high signal-to-background ratio the burst thresholds are also not comparable to that of single dye samples. Second, the spatial distribution of dyes is different for TetraSpeck beads. The dyes are smeared out over a sphere with $100nm$ diameter whereas biomolecules of interest have usually dimensions of $\lesssim 10nm$.

5.5.2 Nano-Beads

As shown in the previous section, TetraSpeck beads show indeed full coincidence but they differ in crucial properties like diffusion coefficient and molecular brightness from the later samples of interest. As a better suited reference we utilized a sample manufactured with DNA origami technology [141] that was multiply labeled with ~ 5 dye copies of each Alexa 488 (blue) and Atto 647N (red). DNA origami technology allows to create various geometries and place the dyes at well-defined positions. This freedom of the sample design was already used to create rod-like structures with well-defined dye separation that serve as calibration standard for super-resolution microscopy [142]. The BTCCD reference is a bead-like structure with a diameter of 23 nm. The obtained diffusion coefficient of 11.0 $\frac{\mu m^2}{s}$ is in reasonable agreement with the size. Multiple dye labeling ensures a complete dual labeling and prevents a full darkening due to blinking because the dyes blink independently. The dye separation is however large enough to exclude the occurrence of FRET. Due to the similarity to TetraSpek beads, but having smaller dimensions, we termed the reference sample 'nano-beads'.
Figure 5.6 shows that both coincidence fraction reach indeed full coincidence which proves the capability of the brightness-gated two-color coincidence approach in combination with nano-beads as a reference sample.

5.5.3 Double-Stranded DNA Labeled with Alexa 488 and Atto 647N

In many fluorescence assays that are applied in a biological context it is not possible to label the interaction partners with several fluorophores. In contrast to the nano-bead reference introduced in Section 5.5.2, a more realistic reference sample would therefore only have one dye copy of each color. For that purpose, we utilize a dsDNA oligonucleotide that consists of a single-stranded DNA (ssDNA) that is labeled with one dye copy of Alexa 488 (blue) and Atto 647N (red) each. The dual labeled ssDNA is hybridized to its complementary DNA strand in order to obtain the well-defined structure of double-stranded DNA. The dual labeling on the same single strand is important because it ensures a constant coincidence fraction despite an eventual dissociation of the double strand at the low concentration of a few 10 pM that are used during the single-molecule experiment.

Figure 5.11 shows the distribution of the photon counts per molecule for the dsDNA reference sample. The photon counts are similar to that obtained for the nano-bead reference (cf. Fig. 5.4 and 5.11) which was intentionally reached by using lower laser powers for the nano-beads. The nano-beads sample was excited with a power of 100a.u. (4.2 μW) and 100 a.u. (3.7 μW) for the blue and red laser, respectively. The single dye dsDNA reference was excited with a laser power of 500 a.u. (21 μW) and 500 a.u. (18 μW) in blue and red, respectively. Similar brightnesses of both reference samples can rule out any bias due to different photon counting statistics. The obtained coincidence fractions as a function of brightness threshold are shown in Figure 5.12. The y-intercepts, i. e. the coincidence fractions for $n_{br} = 0$, are different compared to the nano-bead reference (cf. Fig.5.6 and 5.12). The difference might be attributed to slightly different parameters for burst identification and the presence of blinking for the dsDNA reference. However, a similar steep increase of the coincidence fractions can be observed which turns into a plateau. The saturated coincidence fractions are

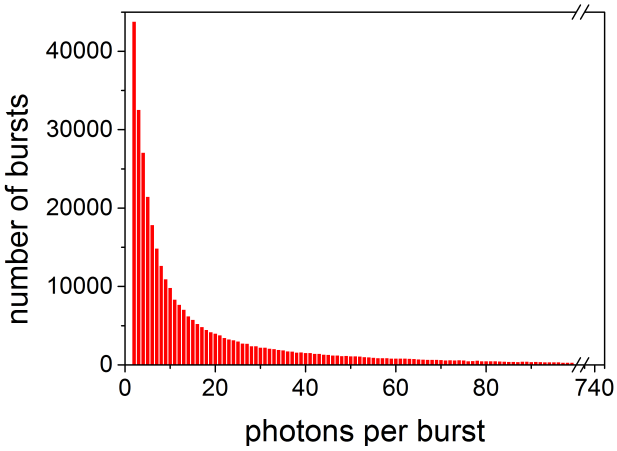

Figure 5.11: Distribution of burst brightness of red channel for dsDNA (Alexa 488/Atto 647N) reference. Distribution of blue channel looks similar and can be found in Appendix Figure B.4. Adopted from [140].

f_{RB} = 0.95 ± 0.01 and f_{BR} = 0.94 ± 0.01. The small deviation to full coincidence is most likely caused by incomplete dual labeling or bleaching of one dye. Nevertheless, published coincidence fractions for a single dye reference are much smaller [143].

5.5.4 Double-Stranded DNA Labeled with Alexa 488 and Alexa 647

In the previous section it was shown that BTCCD yields almost 100 % coincidence for a single dye labeled reference sample. Was that only a lucky 'coincidence' for this specific reference sample or can this also be observed for other single-labeled references? In order to answer this question, the same DNA oligonucleotide was taken and labeled with the red dye Alexa 647 instead of Atto 647N. Alexa 647 is a bright and rather photostable dye suitable for single-molecule experiments but shows however a pronounced photoblinking [144].

The coincidence analysis is shown in Figure 5.13 and yields coincidence fractions of 0.95 ± 0.01 and 0.82±0.03 for the red and blue channel, respectively. In comparison to the Atto 647N-labeled reference, the coincidence fraction of the red signal is identical within the errors. This is consistent because the coincidence of red to blue is calculated and the blue dye (Alexa 488) was retained. In contrast, the coincidence fraction of blue bursts reduces by ~ 12 % which is caused by the exchange of the red dye. Since all experimental conditions were kept identical, especially the laser powers, the reduced blue coincidence is caused by long-lived dark states of Alexa 647 that are common for many carbocyanine dyes and occur on a ms-s time scale [145]. The typical dwell time of the molecule in the detection volume is ~ 1 ms and if Alexa 647 is dark during the entire transit there can obviously no coincidence be detected.

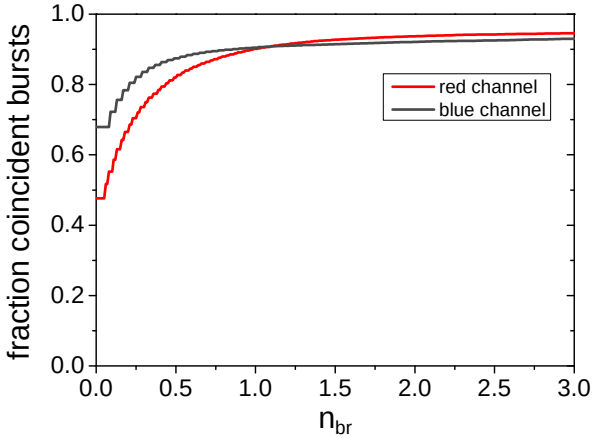

Figure 5.12: Coincidence fractions of dsDNA (Alexa 488/Atto 647N) reference as a function of brightness threshold. Adopted from [140].

Although the long-lived dark states are a rather special characteristic of Alexa 647, the example demonstrates that a careful choice of dyes for coincidence analysis has to be made and, if possible, a calibration with a completely dual-labeled reference should be performed. If the calibration measurement yields coincidence values that are considerably lower than 100 %, these values should be used to rescale the coincidence fractions in a latter experiment. In the case of Alexa 647, this means that the highest detectable blue coincidence fraction is 0.82 and if similar coincidence fractions are obtained for an unknown sample the true coincidence fraction is actually 100 %.

5.6 Benchmark with Conventional Two-Color Coincidence Detection

In this section, the superiority of BTCCD over conventional two-color coincidence detection (TCCD) is demonstrated by a direct comparison. Therefore, the data obtained for all three reference samples is analyzed with state-of-the-art TCCD and the results are compared to those obtained with BTCCD. Conventional TCCD uses binned time traces with an individual brightness threshold applied to each channel. The optimal threshold values are determined by maximizing the coincidence fraction as a function of the threshold values [91]. In particular, the association quotient

$$Q = \frac{C_{cor}}{B + R - C_{cor}} \tag{5.6}$$

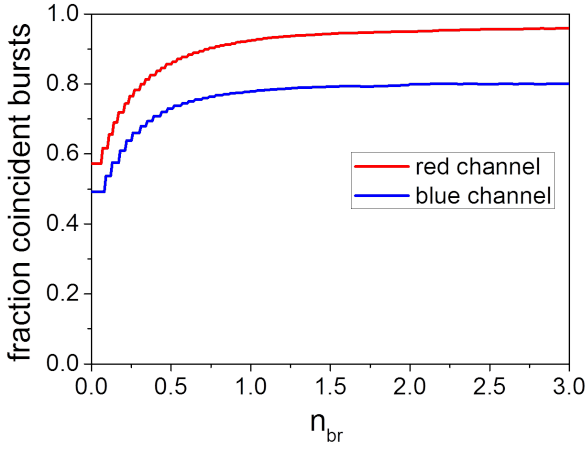

Figure 5.13: Coincidence fractions of dsDNA (Alexa 488/Alexa 647) reference as a function of brightness threshold. Adopted from [140].

is maximized, where C_{cor} is the corrected rate of coincidence events and B and R are the rate of bursts in the blue and red channel, respectively.
The corrected rate of coincident bursts is calculated by subtracting the rate of chance coincidences:

$$C_{cor} = C - BR\tau \tag{5.7}$$

Here, C is the measured rate of coincidence bursts and τ is the binning time. The binning time should be chosen slightly longer than the typical dwell time in the confocal volume. Accordingly, a value of $\tau = 1\,\text{ms}$ was used. The identification of the maximum association quotient Q_{max} is presented in Figure 5.14.
For a comparison of the obtained coincidence to that obtained with BTCCD, individual coincidence fractions of each color are calculated in analogy to Equation 5.1:

$$f_{RB} = \frac{R}{C} \tag{5.8a}$$

$$f_{BR} = \frac{B}{C} \tag{5.8b}$$

Table 5.1 summarizes the TCCD results for the three calibration samples. In comparison to the BTCCD analysis, the coincidence fractions are underestimated by ~ 20 % for the nanobeads and up to ~ 30 % for the single-dye calibration samples.

Interestingly, the TCCD approach also utilizes brightness thresholds for the photon counts in each channel. The main difference to BTCCD is that both thresholds are applied simultaneously. This reduces the dimension of the detection volumes and thereby eventually increases

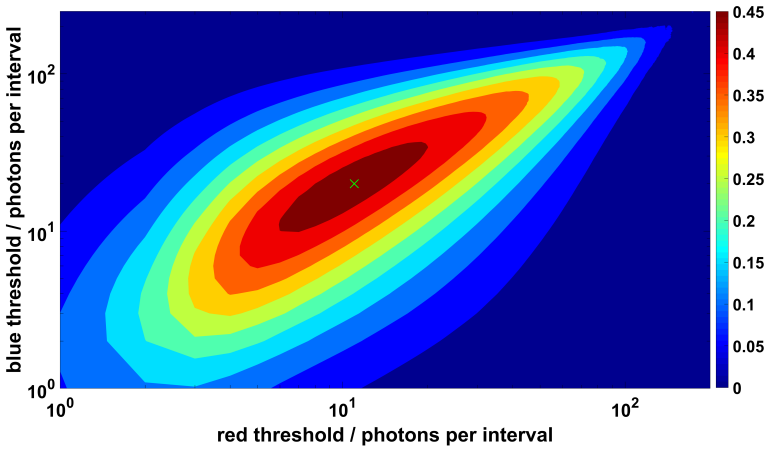

Figure 5.14: Association quotient (see Eq. 5.6) of conventional two-color coincidence detection plotted in color code depending on the brightness thresholds of the blue and red channel. Maximum value is marked with green cross. Data shown for dsDNA (Alexa 488/Atto 647N). Same analysis for other dsDNA reference and nano-bead can be found in Appendix Figure B.5. Adopted from [140].

the overlap. However, this approach cannot compensate for a relative shift of both detection volumes and variations of the relative brightness, e. g. due to blinking.

reference	C	B	R	Q_{max}	f_{BR}	f_{RB}
nano-beads	2.16 Hz	2.63 Hz	2.78 Hz	0.66	0.81	0.77
dsDNA Alexa 488 / Atto 647N	7.28 Hz	11.0 Hz	11.1 Hz	0.48	0.66	0.66
dsDNA Alexa 488 / Alexa 647	0.92 Hz	1.57 Hz	1.46 Hz	0.43	0.58	0.62

Table 5.1: Parameter of conventional TCCD analysis of reference samples.

5.7 Testing the Limits of BTCCD

5.7.1 Dependency on Burst Detection Parameters

The impact of the burst detection parameters, i. e. IPL smoothing value and burst threshold, on the coincidence results was tested by varying the parameters and performing each time a new BTCCD analysis. First, solely the IPL time trace smoothing values m (see Eq. 3.39) or solely the IPL burst thresholds (see Fig. 3.12) were varied concurrently for both channels.

Second, the smoothing values or the burst thresholds were varied conversely, i.e. they were increased for one channel and decreased for the other channel or vice versa.

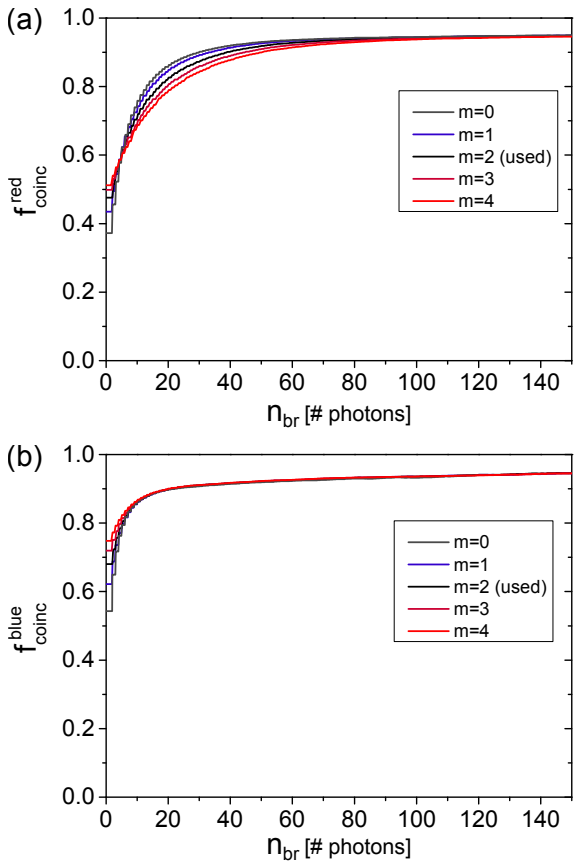

Figure 5.15: Fraction of coincident (a) red and (b) blue bursts as a function of brightness threshold for dsDNA reference (Alexa 488/Atto 647N). The IPL time trace smoothing parameter m is varied concurrently for both channels around the used value (black lines). Note, that large smoothing values will already filter out dim bursts. The red coincidence fraction shows generally a stronger dependency on the smoothing parameter, however, all coincidence fractions saturate at approximately the same value. Adopted from [140].

The coincidence fractions as a function of brightness threshold are shown exemplarily for the dsDNA reference (Alexa 488/Atto 647N) in Figure 5.15 for concurrently increasing or decreasing the IPL smoothing value m and in Figure 5.16 for conversely changing the

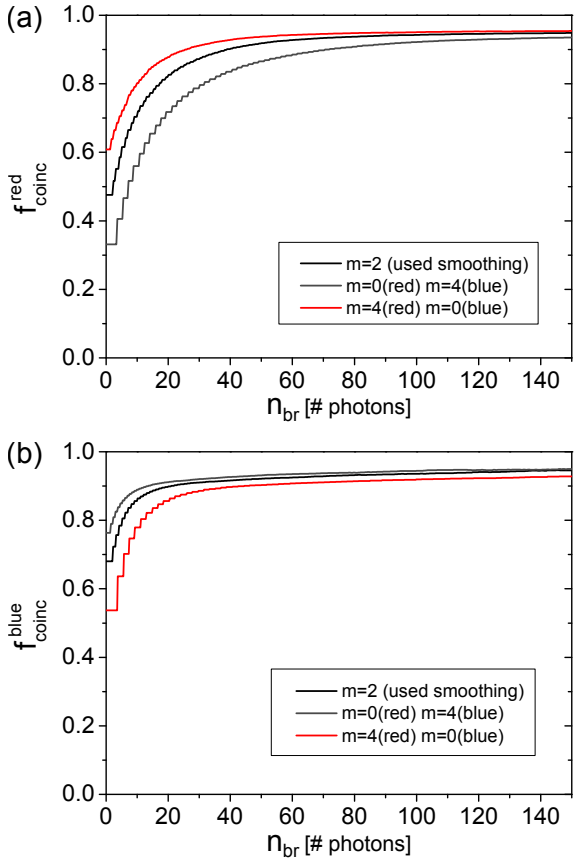

Figure 5.16: Fraction of coincident (a) red and (b) blue bursts as a function of brightness threshold for dsDNA reference (Alexa 488/Atto 647N). The IPL time trace smoothing parameter m is varied from the used value (black lines) conversely for both channels. The red and blue coincidence fractions show an opposite dependency on the smoothing value combinations because a higher smoothing value leads to a preselection of bright bursts in the respective channel and, hence, to higher coincidence fractions and a saturation at smaller brightness thresholds. Adopted from [140].

smoothing values. The same analyses for a variation of the IPL burst threshold can be found in Appendix Figures B.6 and B.7. In all analyses, the brightness thresholds are plotted on an absolute scale because the burst detection parameters have a pronounced impact on the average burst brightness and, hence, using the normalized brightness thresholds would distort

the comparison.
In the case of a concurrent change of the burst detection parameters (see Fig 5.15 and App. Fig. B.6) the coincidence fraction of red bursts shows some variance, whereas that of blue bursts is almost unaffected. This can be interpreted as a higher robustness of the red bursts against a variation of the burst detection parameters. Most important, all coincidence fractions saturate at approximately the same value.
A converse change of the burst detection parameters (see Fig 5.16 and App. Fig. B.7) has the strongest impact on the coincidence fractions which reveals in different shapes of the coincidence fractions as a function of brightness threshold. For example, using a high IPL smoothing for the red channel and a low IPL smoothing for the blue channel leads to a shift towards higher red coincidence fractions and a faster saturation in comparison to the original thresholds. In contrast, the blue coincidence fraction starts at lower values and saturates at higher brightness thresholds. This can be understood as a preselection of bright red bursts and a detection of dim bursts in the blue channel. Again, the saturation values of the coincidence fractions are not remarkably affected by the burst detection parameters.

m_R / m_B	IPL_R / IPL_B	f^R_{coinc}	f^B_{coinc}
2 / 2	110 μs / 120 μs	0.945 ± 0.007	0.94 ± 0.01
0 / 4	110 μs / 120 μs	0.937 ± 0.006	0.94 ± 0.01
4 / 0	110 μs / 120 μs	0.953 ± 0.006	0.913 ± 0.009
2 / 2	55 μs / 180 μs	0.939 ± 0.005	0.94 ± 0.01
2 / 2	165 μs / 60 μs	0.939 ± 0.008	0.928 ± 0.009

Table 5.2: Robustness of coincidence fractions measured for the dsDNA reference (Alexa 488/Atto 647N) for varied burst detection parameters. First line shows the initial parameters. Relative changes of ±100 % of the smoothing value m (see Fig. 5.16) and ±50 % of the IPL threshold value (see App. Fig. B.7) are applied conversely for the red and blue channel. Remarkably, the coincidence fractions are extremely robust and agree mostly within the errors.

The burst detection parameters and the obtained coincidence values are summarized in Table 5.2. Although the burst detection parameters are varied beyond a reasonable range, the coincidence fractions are remarkably stable.

5.7.2 Dependency on Laser Power and Photobleaching

When a dual-labeled molecule, e. g. blue- and red-labeled, transverses the confocal volume there is a certain probability that one of the two fluorophores photobleaches, a fact that would bias the coincidence results. The BTCCD approach can potentially reduce the impact of photobleaching on the coincidence fractions to some extent. The probability that a fluorophore bleaches immediately after entering the confocal volume is low. In contrast, if bleaching occurs, it is likely to happen after the molecule traversed already some part of the confocal volume. It is thus also likely that it already emitted enough photons to be recognized by the burst detection threshold. Since BTCCD compares bright bursts in one channel with all burst in the other channel, the coincidence is still detected although one fluorophore bleached. However, this bleached molecule could reoccur in the confocal volume, now as physically single-labeled, and could be identified incorrectly. Assuming that both fluorophores have a similar photo-stability, there is an increased probability that the remaining fluorophore will also bleach and, hence, the burst will not enter the analysis because it is not bright.

The impact of the photo-stability of a fluorophore can be investigated by varying the excitation power of the corresponding laser. However, this will also affect the effective size and overlap of the confocal volumes (see Fig. 5.2). This effect can be visualized by changing only one excitation power and keeping the other one constant. This is shown for varying the red laser power in Figure 5.17 where a difference of the coincidence fraction due to differences in the confocal overlap can be observed for low brightness thresholds. This effect levels off for larger brightness threshold which proves the robustness of BTCCD.
Returning to the impact of photobleaching, both laser powers were varied simultaneously which should keep the relative overlap of the confocal volumes fairly constant. The coincidence fractions for various laser powers are shown in Figure 5.17 for the dsDNA (Alexa 488/Alexa 647) sample. The red coincidence fractions remain constant over the range of laser powers (red dotted line) indicating that the blue dye (Alexa 488) is not bleaching. The blue coincidence, however, shows a linear decreasing trend for increasing laser powers (indicated by blue dotted line) which is due to bleaching or long-lived dark states of the red dye (Alexa 647). The BTCCD characterization of the single dye-pair dsDNA references was performed using 500 a.u. for both lasers so that photobleaching should only have a minor effect.

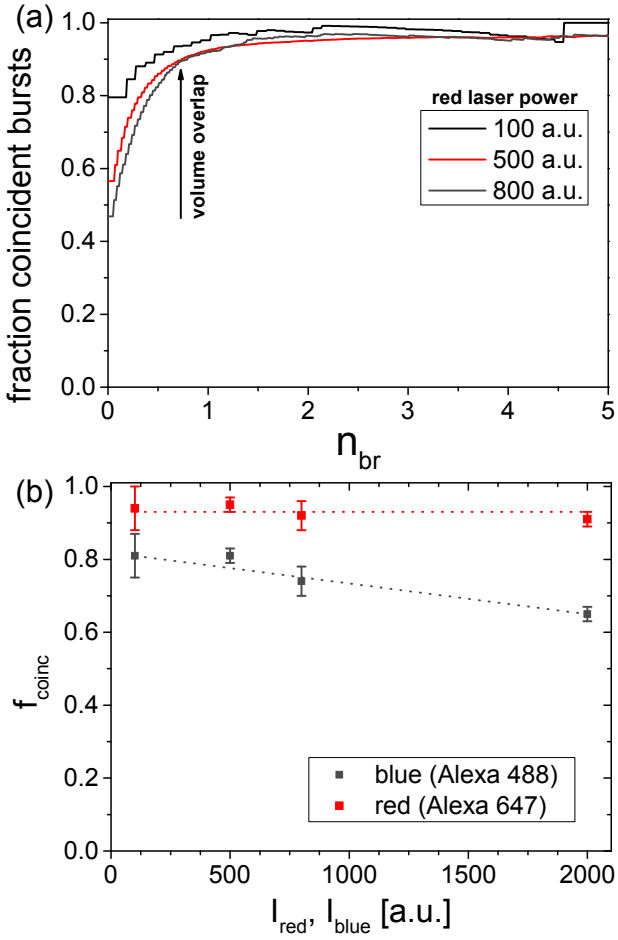

Figure 5.17: (a) Red coincidence fraction of dsDNA (Alexa 488/Alexa 647) reference for various red laser powers. Decreasing the laser power increases the overlap with the blue volume which causes larger starting coincidence fractions ($n_{br} = 0$). The saturating coincidence fraction (above $n_{br} \sim 0.8$) is rather similar for all laser powers which demonstrates that BTCCD is independent of the laser power (at moderate laser powers). (b) Photo-stability of same dsDNA reference. Blue and red laser powers are increased simultaneously. The red coincidence fractions remain constant and the blue coincidence shows a linear decreasing trend for increasing laser powers (indicated by dotted lines) which is due to moderate bleaching or long-lived dark states of the red dye (Alexa 647). Adopted from [140].

5.7.3 Minimal Measurement Time

In order to investigate how long a BTCCD measurement needs to last for a reliable quantification of the coincidence fractions, the data obtained for the dsDNA (Alexa 488/Atto 647N) was chopped into subsets that correspond to measuring times of 30 sec., 1 min., 2 min., 5 min., 20 min., 2 hrs., 4 hrs., and 8 hrs.. The average rate of detected bursts was 13.5 Hz. Each of these data sets was then individually analyzed with BTCCD.

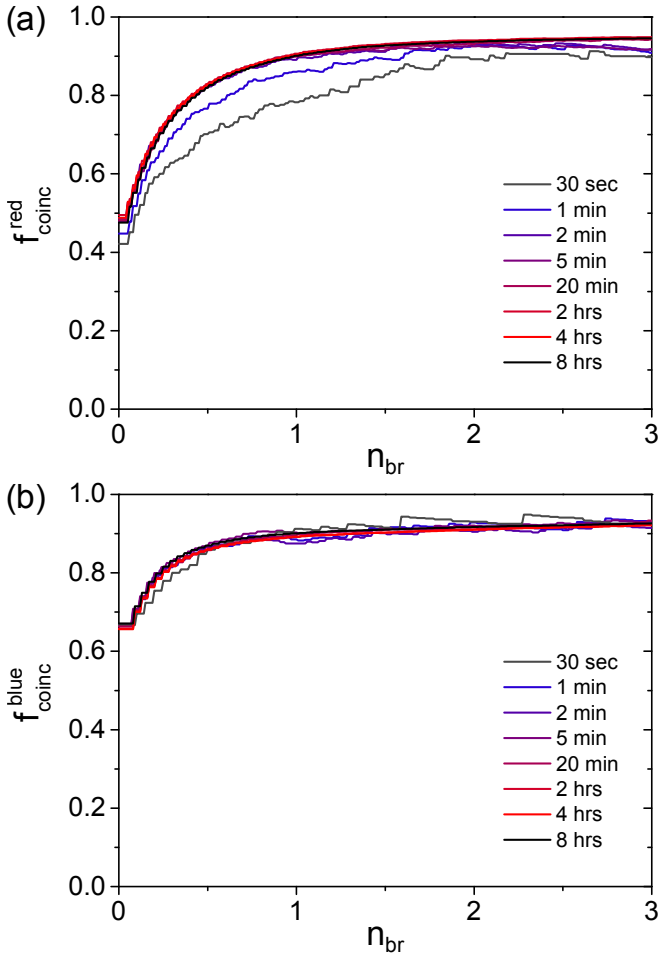

Figure 5.18: Coincidence fractions of dsDNA reference (Alexa 488/Atto 647N) for varying measuring times. Adopted from [140].

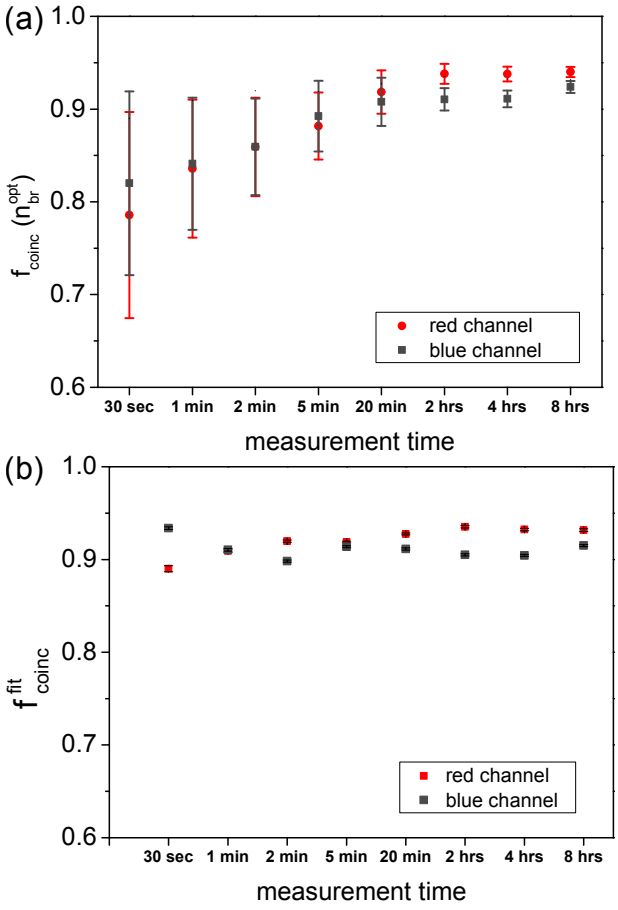

Figure 5.19: Determined coincidence fraction of Figure 5.18 applying (a) the algorithm to identify the optimal brightness threshold (see Sec. 5.4.1) or (b) the fitting approach (see Sec. 5.4.2). Adopted from [140].

Figure 5.18 shows the coincidence fractions as a function of brightness threshold for both channels. While the red coincidence fractions for 30 sec. and 1 min. are slightly lower than that of longer measuring times, all blue coincidence fractions are similar. For longer measuring times, the noise of the coincidence curves is obviously reduced and for measuring times exceeding 20 mins. the curves are almost identical. Applying the procedure to identify the optimal brightness threshold (see Sec. 5.4.1), one obtains the saturating coincidence fractions given in Figure 5.19. Two features can be observed: (i) the errors for short measuring times

are rather large due to the low number of bursts and (ii) the coincidence fractions are underestimated for short measuring times and increase for increasing measuring times until they reach a constant value for measuring times of 20 minutes and longer. The underestimation of the coincidence fractions for short measuring times results from the algorithm to find the optimal brightness threshold (see Sec. 5.4.1). If only a low number of bursts is available to calculate the coincidence fraction, the statistical error is high and the determined value of the optimal brightness threshold is at a position where the coincidence fraction did not yet saturate. This can also be seen by comparing the upper ends of the error bars for the low measuring times. They all agree with the saturating coincidence fractions for measuring times larger than 20 minutes. Based on that observation, the coincidence fractions curves were additionally fitted by the function given in Equation 5.5. The obtained f_{sat}-values for the different measuring times are given in the lower panel of Figure 5.19. Even for the shortest measuring times, the coincidence fractions are well determined, however, the errors are obviously underestimated. For measuring times of 20 minutes and larger, the fitted coincidence fractions agree well with that using the optimal brightness threshold (cf. upper and lower panel in Fig. 5.19).
In summary, for short measuring times (< 20 mins.) the coincidence fractions using the optimal brightness threshold are underestimated and the saturating coincidence fractions should be determined by eye or by fitting. Doing so, even a 1 minute BTCCD measurement can provide an accurate value of the coincidences, however, the error due to the low number of analyzed bursts is considerably high (low precision). How long a BTCCD measurement should take depends on the precision that one wants to achieve. A 20 minutes measurement can already provide a reasonable precision. Finally, the number of bursts determines the precision. For the presented dsDNA reference, ~ 16,000 bursts were detected in 20 minutes. If the investigated sample exhibits a longer diffusion time, less bursts are detected during the same time interval and the total measuring time needs to be adapted accordingly.

5.8 Impact of Chance Coincidence Events

The basis of a single-molecule experiment is that the probability for the presence of more than one molecule at a time in the detection volume is negligible. In a FRET experiment, multi-molecule events lead to a loss of the single-molecule information or even to a misinterpretation of the data [146]. In a TCCD experiment, multi-molecule events lead accordingly to an artificial increase of the coincidence fractions because chance coincidences of single-labeled molecules are interpreted as dual-labeled molecules. Obviously, the impact of chance coincidences is more pronounced if the true coincidence fractions are anyhow low.
As shown in Section 3.3.3, the probability of multi-molecule events is negligible if the average number of molecules in the detection volume is $N \leq 0.03$. However, multi-molecule events can become significant if a brightness gating is applied. This effect was reported for single-molecule FRET experiments in which a threshold for the donor and acceptor photon counts is applied [146]. For BTCCD the same effect is present. The probability of chance coincidences is increased for large brightness thresholds because bright bursts have also a longer dwell time and, consequently, it is more likely that during this increased dwell time another

molecule enters the detection volume. In the following, an expression for the probability of chance coincidences is derived for single-labeled molecules. The description is extended to dual-labeled molecules in the following section.

First, only one species of molecules is considered. The probability that during an observation time t a number of n single molecules enter the detection volume is given by a Poisson distribution [147]

$$p_n^e(t, \tau_d, N) = \frac{(Nt/\tau_d)^n}{n!} exp(-Nt/\tau_d), \tag{5.9}$$

where N is the average number of molecules in the detection volume and τ_d is the mean dwell time in the volume. With the definition of a mean time for entering the volume $\tau_e = \tau_d/N$, equation 5.9 simplifies to

$$p_n^e(t, \tau_e) = \frac{(t/\tau_e)^n}{n!} exp(-t/\tau_e). \tag{5.10}$$

The probabilities for no entry ($n = 0$) and one entry ($n = 1$) are consequently:

$$p_0^e(t, \tau_e) = exp(-t/\tau_e) \tag{5.11a}$$

$$p_1^e(t, \tau_e) = t/\tau_e \, exp(-t/\tau_e) \tag{5.11b}$$

Assuming a constant dwell time, the probability for the occurrence of a burst caused by n single molecules can be estimated based on the following idea. Several bursts caused by multiple molecules cannot be resolved if the molecules enter during a time which is faster than the dwell time. Consequently, the probability pm_n of a multi-molecule burst caused by n molecules is given by the product of the probabilities of $n-1$ molecules entering successively with a delay less than the dwell time τ_d and by the probability that before and after that sequence there is no molecule in the volume [148]:

$$\begin{aligned} pm_n(N) &= p_0^e(\tau_d, \tau_e) \left[\prod_{j=1}^{n-1} p_1^e(t_j < \tau_d, \tau_e) \right] p_0^e(\tau_d, \tau_e) \\ &= exp(-\tau_d/\tau_e) \left[\prod_{j=1}^{n-1} \int_0^{\tau_d} \frac{dt_j}{\tau_e} exp(-t_j/\tau_e) \right] exp(-\tau_d/\tau_e) \\ &= exp(-2N)(1 - exp(-N))^{n-1} \end{aligned} \tag{5.12}$$

Equation 5.12 shows that the probability of multi-molecules events depends only on the average number of molecules in the detection volume. The relevant probability for a chance coincidence event is $pm_{n=2}$ because the presence of two molecules at a time in the detection volume is the minimal requirement for a chance coincidence:

$$pm_{n=2}(N) = exp(-2N)(1 - exp(-N)) \tag{5.13}$$

All other probabilities $pm_{n>2}$ lead also to chance coincidences but their probabilities are smaller and can be neglected for $N \ll 1$. Finally, not the absolute probability to observe a

chance coincidence is of interest but the ratio to the probability to observe a single-molecule event:

$$f_{mm} = \frac{pm_{n=2}(N)}{pm_{n=1}(N)} = 1 - exp(-N) \tag{5.14}$$

Is there a threshold value for N above which multi-molecule events become considerable? The answer to this questions depends obviously on the error one want to tolerate. If a fraction of multi-molecules events of 1 % can be tolerated, a critical mean number of molecules N_c is given by

$$f_{mm} = 0.01 \iff 1 - exp(-N_c) = 0.01 \iff N_c = -ln(0.99) \approx 0.01\,. \tag{5.15}$$

5.8.1 Chance Coincidences in BTCCD

In BTCCD only cross-color multi-molecule events need to be considered. If a red-labeled molecule is located in the detection volume, a chance coincidence occurs when a blue-labeled molecule enters the volume during the dwell time of the red molecule. The probability for entering of a blue-labeled molecule during the dwell time of a red-labeled molecule can be calculated in analogy to Equation 5.11b and 5.12

$$p_e^{RB} = p_1^e(t < \tau_d^R, \tau_e^B) = 1 - exp\left(-\left(\tau_d^R/\tau_d^B\right) N_B\right)\,, \tag{5.16}$$

where τ_d^R and τ_d^B are the mean dwell times of the red-labeled and blue-labeled molecules, respectively, and N_B is the average number of blue-labeled molecules in the detection volume. Instead of entering after the red-labeled molecule, the blue-labeled molecule could also be located in the volume before the red-labeled molecule entered. Consequently, both probabilities, i. e. blue-labeled molecule already present or entering during dwell time of red molecule, have to be added and it needs to be considered that just red-only molecules lead to a false-positive event. Hence, the fraction of chance coincidence is given by

$$\begin{aligned} f_{chance}^{RB} &= (1 - f_{RB})\left[exp(-N_B)\left(1 - exp\left(-\left(\tau_d^R/\tau_d^B\right) N_B\right)\right) + 1 - exp(-N_B)\right] \\ &= (1 - f_{RB})\left[1 - exp\left(-N_B\left(\left(\tau_d^R/\tau_d^B\right) + 1\right)\right)\right] \end{aligned} \tag{5.17}$$

where f_{RB} is the fraction of dual-labeled red molecules.
An analogue expression can be derived for f_{chance}^{BR} if blue and red is interchanged in Equations 5.16 and 5.17:

$$f_{chance}^{BR} = (1 - f_{BR})\left[1 - exp\left(-N_R\left(\left(\tau_d^B/\tau_d^R\right) + 1\right)\right)\right] \tag{5.18}$$

Equations 5.17 and 5.18 show a few implications that arise for cross-color multi-molecule events: (i) The fraction of chance coincidences in the red channel depends on the ratio of the dwell times of the red and blue labeled molecules. The larger the red dwell time, the more probable it is that a blue molecule enters within that time and, accordingly, the lower the blue dwell time, the more frequently blue molecules will enter the detection volume. By applying the brightness threshold to the red channel, the red dwell time will increase whereas the blue dwell time stays constant. Consequently, the fraction of chance coincidences increases for increasing brightness thresholds. (ii) The fraction of chance coincidences in the red channel depends only on the mean number of blue molecules because red-red coincidences are not

considered. However, red-red coincidences lead to an apparent increase of the red dwell time which is neglected here. (iii) The impact of chance coincidences is less pronounced if the molecules have already a high fraction of dual labeling. A dual labeled molecule cannot be misinterpreted by a chance coincidence. Again, the same conclusions can be drawn for chance coincidences of the blue channel.
Equations 5.17 and 5.18 are only an approximation because a constant dwell time and a perfect overlap of the blue and red detection volumes were assumed. The fulfillment of the approximations is checked in the following section by comparing it to experimental data.

5.8.2 Experimental Characterization of Chance Coincidence

In order to estimate the amount of chance coincidences in a BTCCD experiment using Equations 5.17 and 5.18, the dwell times and the average number of molecules in the detection volume have to be known. While the mean dwell times are easily accessible from the experiment, the mean number of molecules is not directly measured. The expected number of molecules is based on the concentration obtained with FCS and the applied dilution factor. However, the mean number of molecules in the single-molecule analysis is usually lower as the expected value. This is mainly caused by the smoothing of the IPL time trace and the application of a burst identification threshold which both already exclude dim bursts. In addition, the blocking of the cover slip is not perfect which can also lead to a partial decrease of the concentration.
Luckily, one can estimate the number of molecules by comparing the total time of fluorescence, i. e. the sum of all dwell times, with the measurement time. The time of fluorescence t_F is given by the product of the probability to observe a burst with the measurement time t_{meas} and also by the product of the mean dwell time and the number of bursts B_{meas} [92]:

$$t_F = (1 - exp(-N))\, t_{meas} = B_{meas}\tau_d \tag{5.19}$$

By rearranging Equation 5.19, one can obtain the number of molecules from the experimental parameters

$$N = -ln(1 - B_{meas} \cdot \tau_d / t_{meas})\,. \tag{5.20}$$

Equation 5.20 can be utilized to independently estimate the mean number of blue and red labeled molecules in the confocal volume and calculate the chance coincidences according to Equation 5.17 and 5.18, respectively.

The impact of chance coincidence was investigated by mixing free Alexa 488 and Alexa 647 dye and performing a BTCCD analysis at various concentrations. The concentrations were chosen such that the number of molecules in the red and blue detection volume are equal. The results for the blue coincidence analysis are shown in Figure 5.20. It can be seen that the calculated fraction of chance coincidences (dashed lines) are in excellent agreement with the experimentally determined coincidence (solid lines). Just at large brightness threshold ($n_{br} > 5$), the measured coincidences stagnate and fluctuate strongly due to the low number of remaining bursts. The chance coincidences increase for increasing brightness thresholds because brighter red burst exhibit also longer dwell times. The offsets between the different concentrations and the different slopes are caused by different number of red molecules N_R.

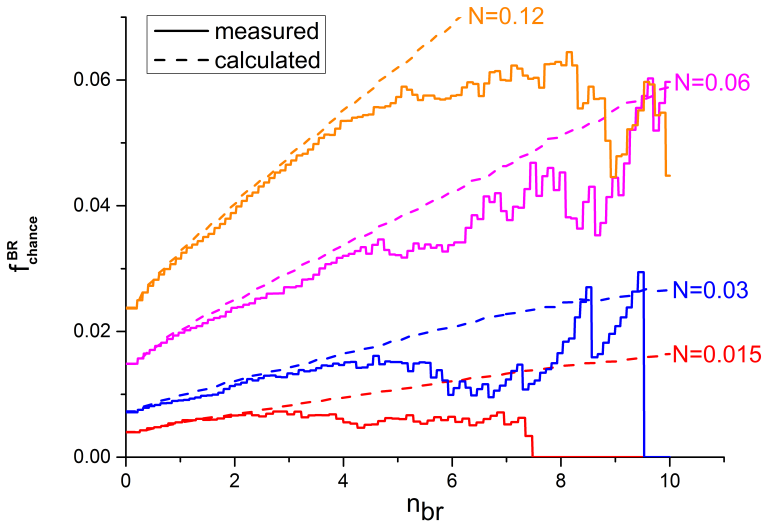

Figure 5.20: Chance coincidences of freely-diffusing Alexa 488 (B) and Alexa 647 (R) dyes. Concentration of dyes is adjusted to achieve same number of molecules in red and blue detection volume ($N_R = N_B = N/2$). BTCCD analysis (solid line) is compared to predicted fraction of blue chance coincidence according to Equation 5.18.

The measured chance coincidences of red bursts show a similar good agreement with the predicted chance coincidences (see App. Fig. B.8). The red chance coincidences show higher values because the red dwell time is longer than the blue one.
One can also experimentally verify another consequence of cross-color chance coincidences found in Section 5.8.1, i. e. chance coincidence for one color do only depend on the concentration of molecules of the other color. Indeed, a twofold increase of the red dye (Alexa 647) leads to similar red chance coincidence but a doubling of blue chance coincidences (cf. App. Figs. B.9 and B.10)

In summary, chance coincidences in the blue channel can be neglected in the relevant concentration regime of $N \leq 0.03$. Even in the presented 'worst case' of no physical coincidence, the fraction of chance coincidence is below 2 % which is in the range of the typical error of BTCCD. However, the chance coincidence fraction of the red channel exceeds 5 % which is no longer negligible. Also, if very low coincidence fractions should be characterized, chance coincidences have to be taken into account explicitly.

There are consequently two possibilities to deal with chance coincidences. Either one can avoid them by employing lower concentrations of $N \leq 0.01$ or they have to be taken into account. This is also the case if the buffer contains fluorescent impurities which sometimes cannot be avoided depending on the experimental conditions. The correction for chance coincidences can be realized in an iterative process as will be discussed in the following section.

5.8.3 Correction for Chance Coincidences

The measured coincidence fraction can be corrected for chance coincidence by subtraction of the chance coincidence fraction which can be easily followed by the example of the red coincidence fraction:

$$f_{RB}^{cor} = \frac{N_{RB}^{cor}}{N_R} = \frac{N_{RB} - N_{RB}^{chance}}{N_R} = \frac{N_{RB}}{N_R} - \frac{N_{RB}^{chance}}{N_R} = f_{RB} - f_{RB}^{chance} \tag{5.21}$$

However, the estimation of chance coincidences depends also on the true coincidence fraction (see Eq. 5.17)

$$f_{RB}^{cor} = f_{RB} - (1 - f_{RB}^{cor}) f_{RB,0}^{chance}, \tag{5.22}$$

where $f_{RB,0}^{chance}$ is the estimated chance coincidence if only single-labeled molecules are present. Equation 5.22 can be rearranged to calculate the corrected coincidence fraction:

$$f_{RB}^{cor} = \frac{f_{RB} - f_{RB,0}^{chance}}{1 - f_{RB,0}^{chance}} \tag{5.23}$$

The correction for chance coincidences of the blue channel follows in analogy:

$$f_{BR}^{cor} = \frac{f_{BR} - f_{BR,0}^{chance}}{1 - f_{BR,0}^{chance}} \tag{5.24}$$

As already mentioned, the impact of chance coincidences on the BTCCD results depends much on the value of the coincidence fraction. This is illustrated in Figure 5.21 where the corrected coincidence fractions are plotted as a function of the fraction of chance coincidences according to Equations 5.23 and 5.24 for various values of measured coincidence fractions. For very large coincidence fractions ($f = 0.95$) the corrections are very minor which is shown by the small slope of the corresponding line. In this case, even rather high chance coincidence fractions do not lead to a large correction. For example, if the chance coincidence fraction is 0.5 the measured coincidence fraction of 0.95 needs to be corrected just to 0.90. In contrast, the corrected coincidence fraction is very sensitive to small chance coincidence fraction if the coincidence fraction is rather low ($f = 0.25$). Here, even the presence of a chance coincidence fraction of 0.1 will reduce the coincidence fraction by approximately one half.

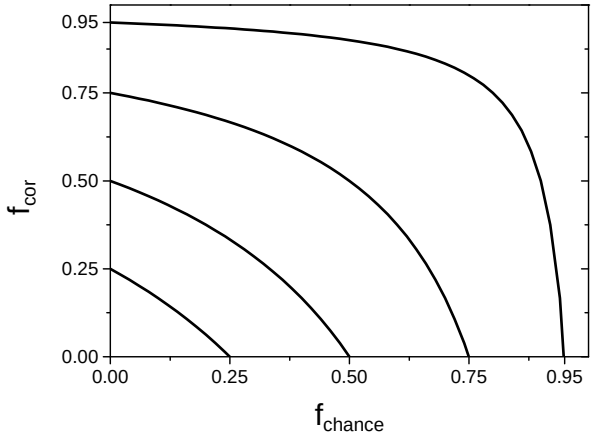

Figure 5.21: Impact of chance coincidence correction depends on the absolute value of the coincidence fraction. Visualization of Equations 5.23 and 5.24 for measured coincidence fractions (f_{RB} or f_{BR}) of 0.95, 0.75, 0.5, 0.25.

5.9 Coincidence Analysis of FRET-Based Biosensors

FRET-based biosensors were introduced in Chapter 4. The BTCCD approach can be used to determine the maturation efficiency of the donor and acceptor fluorescent proteins. Incomplete acceptor maturation leads to a donor-only fraction of sensor molecules which reduces the FRET signal in an ensemble measurement. It is thus important to determine the donor-only fraction in order to evaluate the absolute, potential signal of the sensor. Furthermore, a comparison between different sensor constructs, or different batches of the same construct, is only reasonable if the effect of varying donor-only fractions is known. If on the other hand the donor fluorophore is not completely matured an acceptor-only fraction is present. Although the acceptor-only fraction is not affecting how much FRET occurs, it reduces the overall intensity of the read-out signal. This can become critical if the overall expression is low, e. g. in an *in vivo* experiment. From an application-oriented point of view, donor-only and acceptor-only molecules are waste products and their fractions should be as low as possible.

The application of BTCCD to samples that exhibit FRET is possible and was already reported for conventional TCCD [149]. The detection scheme is modified so that the signal that senses the presence of the donor fluorophore is generated by adding up the donor (blue) and the acceptor (red) emission after exciting the donor. Red emission that occurs after the excitation of the donor fluorophore occurs either due to FRET from the donor to the acceptor fluorophore or due to spectral crosstalk of the donor emission into the red detection channel. In both cases the red signal originated from an excited donor fluorophore and is hence an

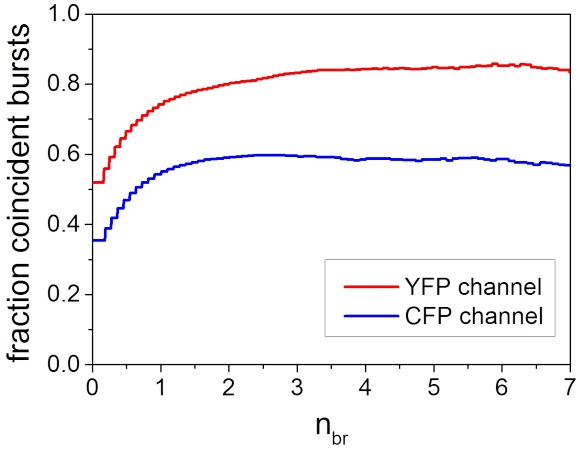

Figure 5.22: Coincidence fractions of glucose sensor no. 1 as a function of brightness threshold. Adopted from [140].

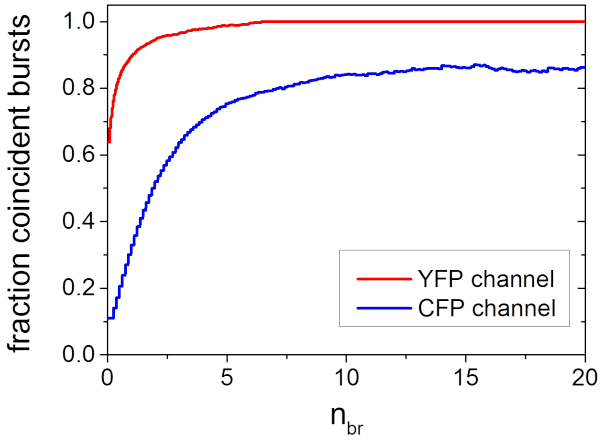

Figure 5.23: Coincidence fractions of crowding sensor GE as a function of brightness threshold. Adopted from [140].

indicator for its presence. This signal generation scheme is only valid if direct excitation of the acceptor fluorophore with the donor excitation laser can be neglected as is the case for

the FRET pair of cyan and yellow fluorescent protein (see App. Fig A.1). However, if direct acceptor excitation cannot be neglected, it should be subtracted beforehand.

Exemplarily, the coincidence fractions as a function of brightness threshold are shown in Figure 5.22 for the glucose sensor construct no. 1 and in Figure 5.23 for the crowding sensor GE. Both graphs show a similar behavior, i. e. the coincidence fractions increase steeply followed by a plateau for higher brightness thresholds. However, the plateau is reached at lower brightness thresholds for the glucose sensor whereas the coincidence fractions of the crowding sensor saturate at larger brightness threshold. This difference is attributed to the different variants of CFP and YFP which have different molecular brightnesses, triplet kinetics, and photo stabilities.

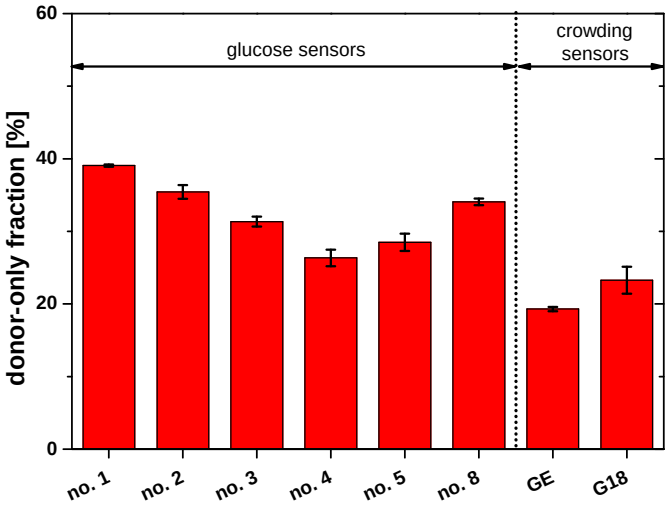

Figure 5.24: Donor-only fractions of FRET-based biosensors. Adopted from [37].

The donor-only fractions of all FRET sensor constructs are summarized in Figure 5.24 and vary between 20 % and 40 %. Within the glucose sensor constructs the variation is less but there is a tendency that the constructs without an acceptor linker (no. 1, 2, 3) exhibit the highest donor-only fractions. The donor-only fractions of the crowding sensor constructs are remarkably lower which is attributed to different fluorescent protein variants and a simpler structure of the sensing domain. The global stoichiometry analysis (see Fig. 5.25) yields a similar result; within the glucose sensor constructs the fractions of single- and dual-fluorescent molecules are rather similar. The crowding sensor constructs show both, a lower donor-only and a lower acceptor-only fraction and in consequence a larger dual-labeled fraction.

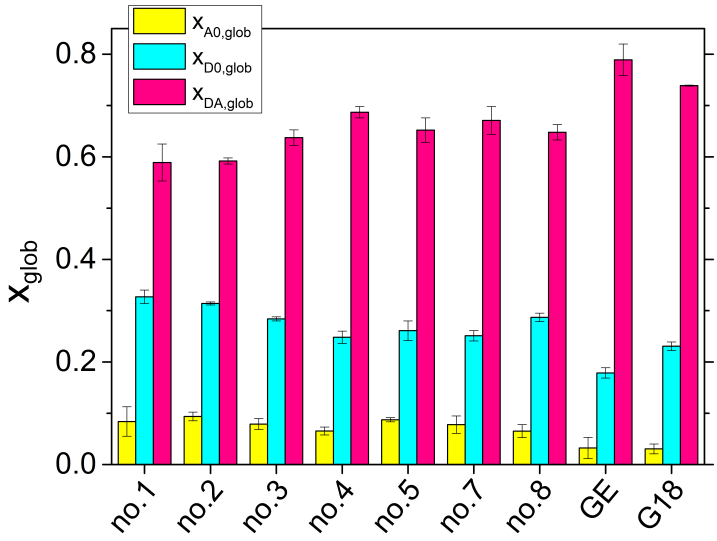

Figure 5.25: Global coincidence analysis of FRET-based biosensors.

In summary, the brightness-gated two-color coincidence detection is a valuable tool to characterize FRET-based biosensors. The reduction of the sensor sensitivity due to a donor-only species can be quantified as well as the global yield of dual-labeled molecules. Fortunately, the data comes for free from the single-molecule FRET experiment.

5.10 Investigation of Protein Translation

5.10.1 Ribosomes as the Center of Protein Synthesis

Proteins can be considered as the most important class of biomolecules as they are essential for almost any cellular processes including metabolism, signaling and regulation, and scaffolding the shape of the cell [131]. They are so to speak the 'working horses' of the cell. The general pathway for protein production was described by Crick in the central dogma of molecular biology [150]. It describes the transfer of information between the three classes of biopolymers: DNA, RNA, and proteins. DNA serves as the long-term storage of information. The information about a certain protein sequence is stored in a gene which is a segment of the DNA. During *transcription*, the sequence of DNA is transferred to a sequence of messenger RNA (mRNA). The *translation* of mRNA in a polypeptide sequence is carried out at the ribosome with the help of transfer RNA (tRNA). The central dogma also states that proteins are the 'dead ends' of information transfer which means that neither proteins can replicate

themselves nor they can serve as templates for RNA or DNA synthesis. This highlights the importance of ribosomes as the macromolecular machinery for protein synthesis.

In the following, only ribosomes from prokaryotic cells, i. e. cells without a cell nucleus, are considered. These ribosomes consist of a small (30S) and a large (50S) subunit that are both built from ribosomal RNA (rRNA) and various proteins. The translation process is a complex interplay between the subunits, the mRNA, tRNAs and various cofactors. However, it can be divided in three phases. In the *initiation* phase the ribosome is prepared for protein synthesis which includes the binding of the 30S and 50S subunit that form the functional 70S ribosome. During *elongation*, tRNAs sequentially transcribe the mRNA codons into amino acids. The nascent protein chain is leaving the ribosome through an exit tunnel. A stop codon encrypts the *termination* of synthesis and the protein is released [132].

Studying ribosomes in their natural environment, i. e. inside the cell, is challenging because specific fluorescent labeling without killing the cell is hard to accomplish. In addition, single-molecule measurements are complicated by auto fluorescence of the cell and high local concentrations of ribosomes. An alternative is to use a cell-free protein synthesis (CFPS) system which allows to fluorescently label ribosomes or their subunits and to modify the translation process. CFPS was already reported decades ago [151] and uses a minimal set of purified constituents to perform translation *in vitro*.

5.10.2 Stalling Efficiency and Activity

Before studying the functionality of the ribosome using a cell-free protein synthesis (CFPS) system, it is worth to study the (modified) CFPS system itself. A crucial parameter of ribosomal function in the CFPS system is the productivity which depends on the activity, i. e. the fraction of ribosomes that are actively synthesizing, and the number of production cycles they undertake. However, since each active ribosome can undergo multiple synthesis cycles the amount of synthesized protein cannot disentangle both contributions. A certain amount of protein could either be synthesized by a low fraction of active ribosomes that undergo multiple synthesis cycles or by a large fraction of ribosome that just undergo less cycles. A way to investigate the activity is to stall the synthesized protein at the ribosome. Naturally, a stop codon in the mRNA encodes that the protein sequence is complete and the protein is released. If a so-called arrest sequence is incorporated between the protein of interest and the stop codon, the release can be suppressed. The arrest sequence strongly interacts with the interior of the exit tunnel and therefore stalls the synthesized protein at the ribosome [152].

Next, the question arises which protein should be used as a representative for protein synthesis and how it should be labeled. A very elegant way is to let the ribosome synthesize a fluorescent protein because it will only fluoresce if it was completely synthesized and there is no need for subsequent labeling. If the synthesized protein is a GFP, it will show characteristic greenish fluorescence after correct folding and fluorophore maturation. If the ribosome is additionally labeled with a red dye, the coincidence of green and red fluorescence can be analyzed.

The concept of the described assay is shown in Figure 5.26. If a red-only burst is detected in the BTCCD experiment it represents an inactive ribosome. Active ribosomes with a stalled

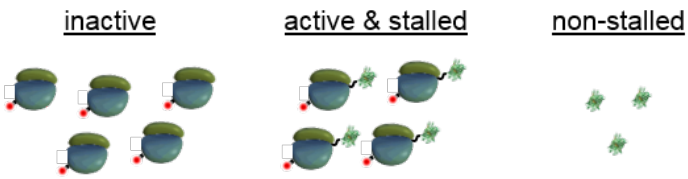

Figure 5.26: Assay for investigation of ribosome performance in CFPS systems.

GFP show a coincidence of red and green fluorescence. Non-stalled GFPs lead to a green-only event.
The stability of the 70S ribosome at the low concentrations needed for the single-molecule characterization (~ pM) were validated in a separate experiment (see App. Fig. B.11) which showed no dissociation of the 70S complex within one hour. Hence, each BTCCD measurement was performed for half an hour to exclude any effects of dissociation. Subsequently, a new dilution was prepared for the next measurement. The results of the BTCCD experiment are presented in Figure 5.27 and show clearly that the coincidence fractions of both channels are not generally equal because they access different biological questions. The fraction of coincident green bursts f_{GR} represents the fraction of stalled GFP molecules which is the stalling efficiency. In contrast, the fraction of coincident red bursts f_{RG} quantifies the fraction of active ribosomes.
The stalling efficiency shows the typical steep increase for increasing brightness thresholds followed by a plateau. The coincidence fraction at the optimal brightness threshold is $f_{GR}^{opt} = 0.94 \pm 0.06$ which means that virtually complete stalling is achieved. The red coincidence fraction however does not show a saturation. It shows a steep increase for small brightness thresholds and a continuous, gentle increase for higher brightness thresholds. Based on this observation, the coincidence fraction was fitted with a two component analogue of Equation 5.5

$$f_{RG}(n_{br}) = c + \Delta f_1 \left(1 - e^{-n_{br}/n_1}\right) + \Delta f_2 \left(1 - e^{-n_{br}/n_2}\right), \tag{5.25}$$

where c is the offset, Δf_1 and Δf_2 are the increases of component 1 and 2, respectively, and n_1 and n_2 are the half-value brightness thresholds of component 1 and 2, respectively.
The fitting parameters are given in Table 5.3. The fast increasing component (component 1) represents the usual exclusion of peripheral trajectories (cf. n_1 in Tab. 5.3 and half-value brightness threshold of reference samples in App. Tab. B.1). The second, slowly increasing component arises most probable due to a fraction of multimeric ribosomes. Hence, only the first component of the red coincidence is interpreted as the activity which can be quantified to be 0.244 ± 0.002.

Although this is a demonstrative example that BTCCD is also able to disentangle two population, i. e. monomeric from multimeric ribosomes, the interpretation of the data is still rather vague because both population cannot be completely separated. Yet, the results were

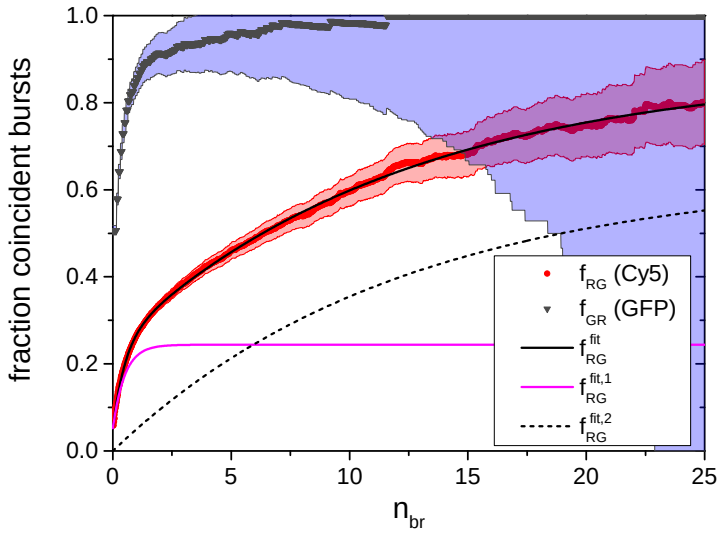

Figure 5.27: BTCCD analysis of CFPS system. Coincidence of GFP as a function of brightness threshold (red curve) is fitted with a two-component increase (Eq. 5.25). Shaded area represents statistical error of coincidence fractions and becomes considerable for GFP at large brightness thresholds due to the small number of remaining bursts.

confirmed by a biological independent BTCCD measurement which yielded similar results and by two-color colocalization microscopy of surface-tethered ribosomes [45].

5.10.3 Translation Initiation

After the performance characterization of ribosomes in a cell-free environment in the previous section, the CFPS system can now be used to study functional properties of the ribosome. More specifically, one can study how protein translation is initiated. The general accepted mode of initiation starts with the small 30S subunit which binds the cofactors and also the mRNA before this complex binds to the large 50S subunit [132]. A possibility of an alternative initiation mode was reported in refs. [153, 154] where mRNA translation was observed for 70S ribosomes that were tethered on a cover slide indicating that dissociation of the subunits is not required. This translation mode can directly start with the full 70S ribosome and is accordingly termed *70S initiation* in contrast to the previously mentioned *30S binding initiation*.

Δf_1	Δf_2	n_1	n_2	c
0.192 ± 0.001	0.634 ± 0.002	0.503 ± 0.002	12.20 ± 0.08	0.052 ± 0.001

Table 5.3: Fitting parameter (see Eq. 5.25) of red coincidence fraction in CFPS system (see Fig. 5.27).

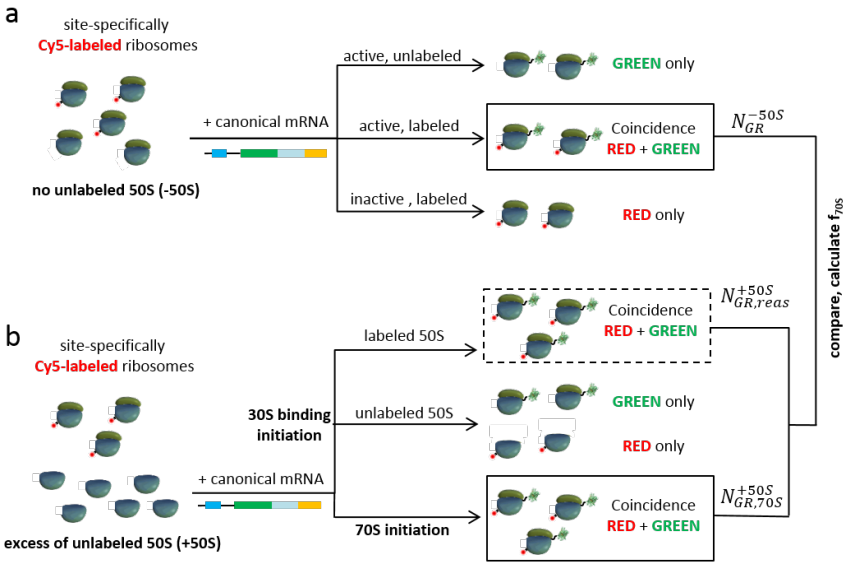

Figure 5.28: Concept of initiation investigation. Adopted from [140].

Now, BTCCD is utilized to quantify to which extend both initiation modes are present. The concept of the experiment is shown in Figure 5.28 and split into two separate measurements. First, the CFPS needs to be characterized (Figure 5.28a). The ribosomes were site-specifically labeled with a single dye at the 50S subunit by hybridizing a Cy5-labeled oligonucleotide to a ribosomal RNA loop [40]. After addition of mRNA that encodes for GFP, three outcomes are possible: (i) the ribosome actively synthesized GFP but it was unlabeled, (ii) the ribosome was active and also labeled or (iii) the ribosome was inactive but labeled. These three scenarios result in three different fluorescent signals that are distinguishable by BTCCD as a green-only molecule, a coincidence of green and red, or a red-only molecule, respectively. Non-labeled and inactive ribosomes are not visible in the experiment.
Second, the same reaction is repeated with an 5x excess of unlabeled 50S subunits (Figure 5.28b). Again, mRNA is added and translation takes place. Depending on the initiation mode, the fluorescence signals differ. In the case of 30S binding initiation, the 70S ribosome disso-

ciates and the 30S subunit binds to an unlabeled 50S subunit due to the excess. The products of the 30S binding initiation are hence a non-labeled 70S ribosome with a stalled GFP (green only) and a free, labeled 50S subunit (red only). In contrast, if the ribosome undergoes 70S initiation, Cy5 remains at the 70S ribosome and a coincident burst red and green fluorescence is observed. However, a second pathway for the occurrence of a coincident signal arises due to the finite excess of unlabeled 50S. If the ribosome follows the 30S binding initiation it dissociates which results in a free, labeled 50S subunit in solution. These labeled 50S subunits mix with the unlabeled 50S subunits. The experimental constrains did not allow a higher excess than 5-fold which results in a non-negligible probability that a dissociated 30S subunit will rebind a labeled 50S subunit. Hence, the 30S binding initiation will partially also lead to a coincident signal (dashed box in Figure 5.28b).
Finally, the coincidence of the control experiment is compared to that with the excess of 50S subunits. The measured fraction of 70S initiation will also have a contribution of reassociated labeled 30S subunits according to

$$f_{70S} = \frac{N_{GR,70S}^{+50S} + N_{GR,reas}^{+50S}}{N_{GR}^{-50S}} = \frac{N_{GR,70S}^{+50S}}{N_{GR}^{-50S}} + \frac{N_{GR,reas}^{+50S}}{N_{GR}^{-50S}} = p_{70S} + p_{reas}\,, \tag{5.26}$$

where $N_{GR,70S}^{+50S}$ and $N_{GR,reas}^{+50S}$ are the number of coincident events in the excess of unlabeled 50S subunits caused by 70S initiation or by reassociation with a labeled 50S, respectively, N_{GR}^{-50S} is the number of coincident events for the reference experiment, p_{70S} is the true probability for 70S initiation and p_{reas} is the probability of reassociation with a labeled 50S subunit during 30S binding initiation.
The probability of reassociation with a labeled 50S subunit is given by the product of the probability for 30S initiation p_{30S} and the probability to find a labeled 50S in solution

$$p_{reas} = p_{30S}\,\frac{p_{30S}\cdot c_{70S}}{p_{30S}\cdot c_{70S} + x\cdot c_{70S}} = \frac{p_{30S}^2}{p_{30S} + x}\,, \tag{5.27}$$

where c_{70S} is the concentration of 70S ribosomes and x is the excess of unlabeled 50S subunits. Inserting Equation 5.27 in Equation 5.26 with $p_{30S} = 1 - p_{70S}$ yields

$$f_{70S} = p_{70S} + \frac{(1-p_{70S})^2}{(1-p_{70S}) + x}\,. \tag{5.28}$$

The results of the BTCCD experiment are shown in Figure 5.29 for the GFP signal and in Figure 5.30 for the Cy5 signal. The concentration during the BTCCD experiment was unfortunately larger than what was expected based on the dilution factor. Chance coincidences had therefore to be taken into account and were subtracted as described in Section 5.8.3. The ratios of the coincidence in presence of 50S excess (dashed lines) with respect to the control experiment (dotted lines) are depicted by solid lines and correspond to the measured fraction of 70S initiation given by Equation 5.28. For the GFP signal, the corrected and uncorrected coincidence ratios level off at similar values. The average values for $n_{br} > 2.5$ are 0.34 ± 0.01 and 0.34 ± 0.03 for the uncorrected and corrected ratios, respectively.
The coincidence ratio of the Cy5 signal varies for the corrected and uncorrected coincidence

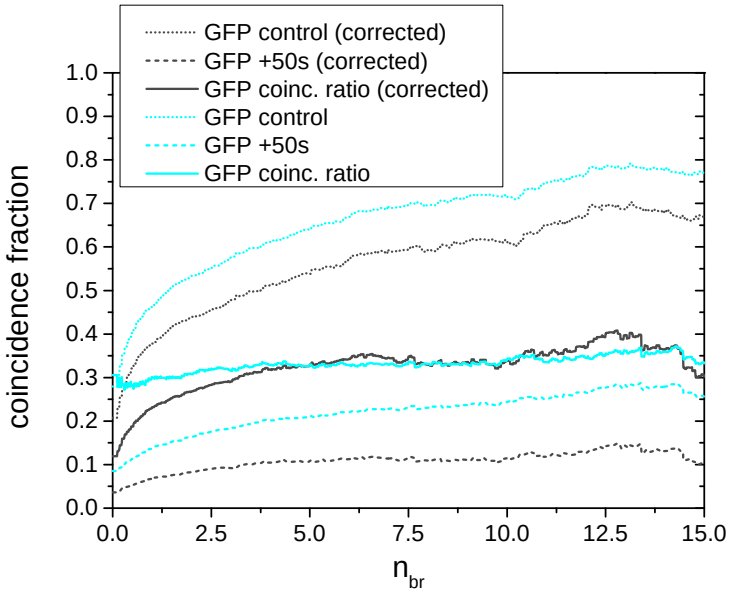

Figure 5.29: BTCCD results of GFP signal of initiation experiment.

fractions. The uncorrected ratio is 0.37 ± 0.02 and the corrected is 0.21 ± 0.02. Except the corrected Cy5 coincidence ratio, all other ratios are in good agreement which motivated to use a weighted mean to characterize the fraction of 70S initiation. Consequently, the experimentally determined 70S initiation is $f_{70S} = 0.31 \pm 0.04$. Comparing this value with Equation 5.28 reveals that f_{70S} is significantly larger than pure 30S reassociation would cause and can be best described by a probability for 70S initiation of $p_{70S} = 0.2$ (cf. blue and red line in Figure 5.31).

In summary, the results show clearly that 70S initiation is possible but rather rare. Several aspects of the experiment require certainly an improvement. First, the deviation between both corrected coincidence ratios indicate that the results should be considered preliminary. In a new experiment it should be paid attention that the concentration during the BTCCD is low enough to neglect chance coincidences. Second, it should be reconsidered if the experiment could be conducted with higher excesses of unlabeled 50S which would add more data points to Figure 5.31 and, hence, increase the reliability.

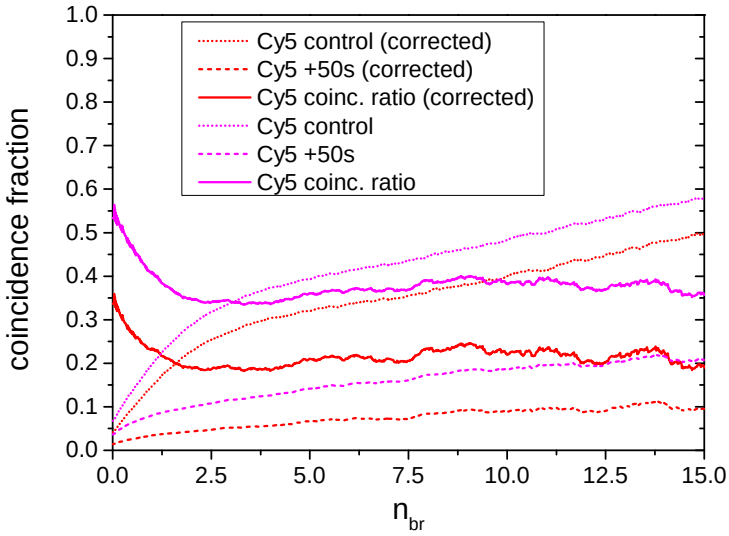

Figure 5.30: BTCCD results of Cy5 signal of initiation experiment.

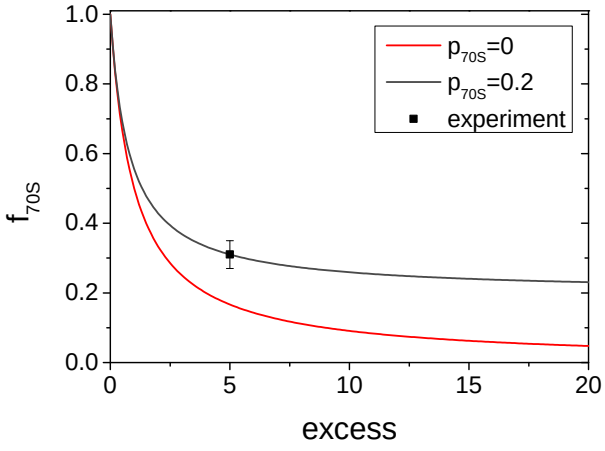

Figure 5.31: Measured fraction of 70S initiation f_{70S} (black point) is significantly larger than expected based on pure 30S binding initiation (red line) and agrees best with a probability of 70S initiation of 0.2 (blue line). Lines are given by Equation 5.28.

6 Conclusion and Outlook

6.1 Genetically-Encoded FRET-Based Biosensors

Summing up the findings, the single-molecule characterization of FRET-based biosensor that are equipped with a CFP/YFP FRET pair is challenging, but possible. The major challenge is the low signal of fluorescence intensity emitted by the fluorescent proteins. The utilization of a confocal microscope with a 437 nm/509 nm laser pair with suitable optical elements allowed to sufficiently exclude the background caused mainly by Raman scattering. The quantitative smFRET characterization relied further on a precise determination of correction factors. The capability of the single-molecule characterization was demonstrated by investigating a set of FRET-based biosensors for the determination of glucose concentration. The obtained smFRET efficiency histograms for various glucose concentrations show a reasonable counting statistics and allow for the first time a quantitative comparison of different sensor constructs on the single-molecule level.

In particular, the glucose sensors can be described by a two-state model which revealed in a low FRET and a high FRET population in the smFRET histograms. Each smFRET histogram displays a 'fingerprint' of the respective sensor construct and allows to identify multiple factors that determine the performance of the respective construct. In particular, the difference between the high and low FRET population specifies how well the sensor transduces the conformational change upon binding of glucose into a change in FRET. The fraction of sensor molecules that accumulate in the low FRET state in absence of glucose and transfer to the high FRET state at saturating glucose concentration quantifies how efficient the sensor utilizes the transduction mechanism. Finally, the donor-only fraction determines the reduction of the FRET signal in an ensemble measurement. The quality of the transduction and its utilization level showed a correlation, i. e. highly sensitive sensor constructs exhibit a large separation between the low and the high FRET state and upon glucose binding an almost full transfer from the low to the high FRET state takes place. In contrast, less sensitive sensor constructs showed a smaller difference of FRET between both states accompanied with an incomplete transfer upon glucose addition. The cause for the aforementioned correlation remains unclear. Without a deeper understanding of the molecular details it is consequently not possible to give a precise instruction for the sensors design, however, the detailed analysis of the individual parameters that contribute to the performance of each sensor construct facilitates a more systematic design of FRET-based biosensors.

It was furthermore possible to investigate the response to macromolecular crowding of the glucose sensor and two biosensors that were specifically designed to sense macromolecular crowding. Up on addition of the crowding agent PEG 6,000 up to concentrations of 20 w/w%, both types of sensors showed a similar response, i. e. a steady increase of the smFRET efficiencies. However, the crowding sensor constructs showed, in contrast to the glucose sensor,

only a single FRET population. The increase of FRET is interpreted as a compaction of the probe that is facilitated by the presence of fluorescent proteins because FRET did not change for a dye-labeled glucose binding protein under crowding conditions. New crowding sensors might even aim to utilize two (or more) states. Here, the smFRET characterization allows to test this design concept.
One can relate the response of the biosensors to the presence of glucose and crowding to two competing models of molecular recognition. Even in the absence of glucose, the glucose sensor exists in two distinct conformations (see e. g. Figure 4.16). When glucose is added, it can only bind to one of the sensor conformations and therefore energetically stabilizes this conformation. This model is referred to as 'conformational selection' [155]. Although the crowder molecules are actually not binding to the biosensor, the effect of crowding is comparable to another molecular recognition hypothesis, namely 'induced fit' [156]. In this model, the presence of a ligand induces a conformation that has not been present in the absence of the ligand.

The contribution of the distance change and the reorientation to the signal change of genetically-encoded FRET-based biosensors could not yet be disentangled. However, it was not possible to design an equally sensitive dye-labeled glucose sensor using the same glucose binding protein MglB. This already indicates that reorientations of the fluorescent proteins (FPs) at least contribute to the change in FRET. Another hint for the importance of reorientations is given by the design of the FP-equipped glucose sensor. The donor FP is internally fused to glucose/galactose-binding protein (MglB) in close proximity to the glucose binding pocket. Hence, an interaction of the MglB and the FP upon the conformational change of MglB is likely and might change the average orientation of the FP. A more consistent approach to quantify the distance change between the FPs would be to label each FP with a dye and perform a smFRET experiment. However, a few aspects have to be considered. First, the FPs need to be non-fluorescent in order not to interfere with the dye's fluorescence. This can be achieved either by previous photobleaching of the FPs or by utilization of non-fluorescent FP mutants. Second, the obtained inter-dye distance will not reflect the actual inter-chromophore distance of the FPs because the chromophore is buried in the β-barrel structure of the FPs and the dyes can only be attached to the FP surface. The dye attachment to the FP surface has also the drawback that reorientations could cause a change of the inter-dye distance although a rotation of the FPs alone will not change the distance between the FP fluorophores. Hence, the assignment of a distance change, that was measured by a FRET change of the dye-labeled FPs, to the distance change of the FP fluorophore could lead to wrong interpretations.

So far, the evaluation of the presented smFRET experiments of FP- equipped biosensor relied predominantly on FRET efficiency histograms. Future experiment can extent the detection to a full multiparameter fluorescence detection [157]. In such a four channel setup, the polarization of each photon is additionally analyzed which allows also analyses of the fluorescence anisotropy. A change of the anisotropy parameter allows in turn to monitor changes of the rotational mobility. However, ensemble measurements showed already that the timescale of overall tumbling of the sensor strongly interferes with that of a single FP rotation. A possibility to prevent the sensor from tumbling is potentially to immobilize it [158]. In such an experiment, the sensor would be anchored to a glass surface and the laser focus

would reside on the sensor's position. Yet, it is challenging to propose an anchoring mechanism that is suppressing the sensor tumbling and at the same time minimizes the interaction with the anchor molecule and the glass surface.

The major limitation of the single-molecule characterization of FRET-based biosensor is probably the extended measurement time. The usable burst rate is approximately 10 % of smFRET studies that utilize organic dyes. Hence, typical measurement times of 8-10 hours were necessary to reach reasonable counting statistics. Even if the necessary measurement time can be slightly reduced by a further improvement of the setup, the single-molecule characterization of FP-equipped FRET-based biosensors will obviously not become a standard technique for the sensor characterization. Yet, single-molecule experiments extend the toolbox of methods to investigate FRET-based biosensors. The most promising application of single-molecules experiments is to investigate certain aspects of the sensor properties using a suitable model system. In this respect, the presented study of the glucose sensor focused on the impact of the linker. Possible future studies could investigate the effect of the interchange of donor and acceptor FPs because it was reported that the interchange of the FPs can alter the signal of the sensor [159]. The single-molecule characterization could reveal if the different signal might be related to a variation of maturation efficiency depending on the insertion position of the FP. The single-molecule characterization of circular permuted sensors is also a fascinating research field because circular permutations can also remarkably change the sensor signal [160].

A further way to deal with the entanglement of distance and relative orientation for the origination of the FRET signal is to employ an additional research method that probes only the distance like small-angle X-ray scattering (SAXS) [161]. Briefly, the SAXS scattering curve can be used to obtain a low-resolution structural model of the biosensor [162]. Since the FPs are rather bulky, they can be potentially identified even in a low-resolution model. SAXS measurements have been performed by Mona Sarter with the glucose sensor constructs no. 2 and no. 4 in absence of glucose and at saturating glucose concentrations. While the scattering curves of sensor no. 4 are rather similar in absence and in presence of glucose, the scattering curves of sensor no. 2 exhibit clear differences between the absence and presence of glucose (personal communication with M. Sarter). Interestingly, the scattering curve in presence of glucose is best described by an ensemble of sensor conformations with two peaks that correspond to an expanded and a compact state. Going one step further, both sensor constructs were modeled using a coarse-grained molecular dynamics simulation presented recently by Reinartz et al. [163]. The structural models that were obtained from the simulation showed a broad conformational ensemble where the FPs were very flexible. Most of this conformations result in very low energy transfer efficiencies even in the presence of glucose. This is on the one hand caused by large FP separations. On the other hand, if the FPs are very mobile, more orientations result in a low κ^2 (see Fig. 4.2) which is also confirmed by detailed analyses [164, 165]. The discrepancy between the low transfer efficiencies obtained by the simulations and the high energy transfers from the smFRET characterization, especially for construct no. 2, reveal that there is probably a constraint/interaction that is not yet captured by the simulation. However, after the refinement of the simulation, the combination of smFRET, SAXS, and simulations is the most promising way to shed line on the biosensors'

functionality. A reliable simulation of biosensors would also enable to test and evaluate new sensor designs directly with the computer instead of doing extensive trial-and-error testing.

6.2 Brightness-Gated Two-Color Coincidence Detection

In this work, brightness-gating was presented as an improvement when the coincidence of two spectrally distinguishable fluorophores should be analyzed at the single-molecule level. Conventional two-color coincidence detection (TCCD) underestimates the coincidence because the molecular detection functions of both fluorophores differ in size and may be shifted with respect to each other. The capability of brightness-gated two-color coincidence detection (BTCCD) was demonstrated with the help of various completely dual-labeled reference samples. First, BTCCD of TetraSpeck beads yielded full coincidence. In an effort to approach more realistic sample dimensions, nano-beads were introduced as reference samples. The nano-beads were fabricated by DNA origami technology and have a diameter of 23 nm. A minimal labeling ratio of ~ 5 dye copies of each color ensured complete dual-labeling and, indeed, the BTCCD analysis showed full coincidence. Finally, BTCCD was applied to a reference sample, namely dsDNA, that was labeled with a single dye copy of each color. Here, the BTCCD analysis yielded coincidence fractions of ~ 95 %. The reason for the slight deviation from full coincidence remained unclear. Possible reasons might be incomplete labeling or photobleaching. The practically full coincidence for a single dye-pair demonstrates that BTCCD is also capable to tolerate the stochastic signal of single emitters including blinking due to triplet kinetics. A limit is reached when the timescale of blinking exceeds the observation time which was demonstrated by replacing the red dye of the dsDNA reference sample with Alexa 647, a dye that exhibits long-lived dark states up to seconds. Here, the coincidence fraction of blue bursts dropped to 82 %.
A comparison of the BTCCD results to those of conventional TCCD revealed that the coincidence fractions determined with TCCD would be underestimated by 20 – 30 %. BTCCD is very robust against variations of the burst detection parameter and shows only a slight sensitivity to photobleaching. Being a single-molecule method, BTCCD requires more experimental time than ensemble techniques. However, it was shown that reliable results can already be obtained in 20 minutes. It was also ensured that BTCCD is not overestimating the coincidence by accidentally evaluating chance coincidences of multi-molecule events. In summary, the algorithm of BTCCD is easy to implement and facilitates a quantitative coincidence analysis.

After the approval of BTCCD, it was applied to two biological system, i. e. FRET-based biosensors and cell-free protein synthesis (CFPS). The donor-only and acceptor-only fractions of FRET samples can in general be determined with BTCCD. The donor-only fraction reduces the ensemble FRET signal and was 20 – 40 % for the investigated biosensors. A global coincidence analysis can quantify the fraction of dual-fluorescent sensor molecules with respect to the whole ensemble. Since the acceptor-only fractions were generally rather small, the global fraction of the donor-acceptor population was 60 – 80 %.
In a CFPS system, ribosomes synthesize proteins *in vitro* with a minimal set of constituents. BTCCD was first applied to quantify the performance of the ribosomes in the CFPS system.

The ribosomes were labeled with a red dye and synthesized GFP that was stalled at the ribosome. The high stalling efficiency of 94 % was determined as the coincidence fraction of the GFP signal. The coincidence fraction of the red signal was 24 % and corresponds to the fraction of active ribosomes. In the next step, a previously unnoticed initiation mode was investigated. This 70S initiation mode does not require dissociated subunits which is in contrast to the widely accepted 30S initiation mode. By labeling only the 50S ribosomal subunit and offering an excess of unlabeled 50S subunits, the fraction of full 70S ribosomes that do not dissociate prior to protein translation could be quantified. Although the experimental design needs to be improved, the fraction of ribosomes that perform 70S initiation could be quantified to be ~ 20 %.
For further studies, different improvements of the CFPS assay should be implemented. First, the 50S subunits should be labeled covalently because the labeling by RNA hybridization appeared to be error-prone. Second, different excesses of unlabeled 50S would increase the reliability of the findings. Another cross-check would be to move the dye label from the 50S subunit to the 30S subunit to exclude any bias of the labels. After the implementation of a reliable CFPS assay it would be very interesting to repeat the experiment under different conditions to investigate whether certain parameter regulate the utilization of the different initiation modes. Up to now it is not clear if the 70S initiation has a biological relevance and if there are situation in which it becomes essential.

A major limitation of BTCCD is probably that it relies on single-molecule data and, hence, limits the maximum concentration to a few 10 pM. The concentration regime can be slightly increased by employing a smaller pinhole, e. g. with a diameter of $30\mu m$ instead of $75\mu m$. However, the BTCCD analysis of molecular interactions that are not stable at comparable concentrations is hampered. On the other hand, BTCCD can investigate very strong interactions that cannot be characterized with other techniques. As an example, the binding between biotin and streptavidin is considered to be the strongest non-covalent interaction of biomolecules. Other techniques such as isothermal titration calorimetry could only give an upper boundary for the dissociation constant of $K_D \approx 10^{-14}$ M of the biotin/streptavidin complex [166, 167]. BTCCD might be able to investigate the presence of the complex down to concentrations of fM or even below.
Coming back to less stable biological interactions, BTCCD could be used in combination with different approaches that aim to overcome the concentration barrier including nanophotonic devices, e. g. zero mode waveguides [168, 169].

The BTCCD analysis of complex biomolecular systems such as ribosomes revealed that brightness-gating works best for homogeneously labeled molecules. The purpose of the brightness gating is to sort molecules according to their trajectories. However, if there is a correlation between the brightness (number of labels) and the molecule's properties, e. g. in the case of oligomerization, BTCCD can lead to misinterpretations. BTCCD relies on the assumption that the subset of selected molecules represents the total ensemble of molecules which is impeded e. g. in the scenario of oligomerization. On the other hand, BTCCD provides an intrinsic check of the sample quality because deviations from homogeneous sample properties can be monitored by the absence of a single plateau of the coincidence fraction (see Fig. 5.27). For a higher reliability it might be beneficial to incorporate further gating parameters,

e. g. the dwell time, and check the consistency of the coincidence fractions obtained with the different gating parameters.

Inherent to most single-molecule analyses, BTCCD requires prolonged measuring times in order to acquire sufficient counting statistics. In return for the prolonged measuring time, BTCCD provides coincidence values with high accuracy of typically a few %. Similar to BTCCD, fluorescence cross-correlation spectroscopy (FCCS) can also provide information about the occurrence of a dual-labeled molecule (complex) but at faster measuring times. Due to the incomplete overlap of the confocal volumes, FCCS requires a calibration measurement with a dual-labeled sample in order to assign a cross-correlation amplitude to a concentration of the dual-labeled molecules. Usually, dual-labeled DNA oligonucleotides are used as FCCS calibration samples and 100 % dual-labeling is assumed [170]. The BTCCD results reveal that this is a reasonable assumption for some dye pairs but not for others (cf. Sec. 5.5.3 and 5.5.4). It should be mentioned that the dual-labeling of the same DNA strand is essential because potential dsDNA dissociation would otherwise reduce the coincidence. In general, BTCCD can serve as a tool to characterize the calibration samples for FCCS. Consequently, the choice of a calibration sample would not be limited to DNA oligonucleotides. Instead, calibration samples that are more similar to the later samples under study could be used. For example, if a molecular interaction should be characterized under different external parameters, it could be first measured under standard conditions with FCCS and BTCCD. Subsequently, FCCS experiments under different conditions can be carried out and evaluated quantitatively with the help of the BTCCD analysis of the reference.

Bibliography

[1] E. Hecht. Optik. Oldenbourg, München, 5. edition (2009). ISBN 9783486588613

[2] N. Menn. Practical optics. Elsevier Academic Press, Burlington, MA (2004). ISBN 978-0-12-490951-9

[3] S. Hogg. Essential microbiology. Wiley-Blackwell, Chichester, 2. edition (2013). ISBN 978-1-119-97891-6

[4] B. Huang, M. Bates, and X. Zhuang. Super-resolution fluorescence microscopy. *Annual Review of Biochemistry* **78**, 993–1016 (2009)

[5] B. O. Leung and K. C. Chou. Review of super-resolution fluorescence microscopy for biology. *Applied Spectroscopy* **65**, 967–980 (2011)

[6] E. Betzig et al. Imaging intracellular fluorescent proteins at nanometer resolution. *Science* **313**, 1642–1645 (2006)

[7] A. G. Godin, B. Lounis, and L. Cognet. Super-resolution microscopy approaches for live cell imaging. *Biophysical Journal* **107**, 1777–1784 (2014)

[8] P. Schwille and S. Diez. Synthetic biology of minimal systems. *Critical Reviews in Biochemistry and Molecular Biology* **44**, 223–242 (2009)

[9] P. Schwille et al. MaxSynBio: Avenues Towards Creating Cells from the Bottom Up. *Angewandte Chemie (International ed.)* **57**, 13382–13392 (2018)

[10] K. C. Neuman and A. Nagy. Single-molecule force spectroscopy: optical tweezers, magnetic tweezers and atomic force microscopy. *Nature Methods* **5**, 491–505 (2008)

[11] P. Hinterdorfer and A. Oijen (editors). Handbook of Single-Molecule Biophysics. Springer US, New York, NY (2009). ISBN 978-0-387-76496-2

[12] M. Orrit, T. Ha, and V. Sandoghdar. Single-molecule optical spectroscopy. *Chemical Society Reviews* **43**, 973–976 (2014)

[13] H. Höfig et al. Single-Molecule Studies on a FRET Biosensor: Lessons from a Comparison of Fluorescent Protein Equipped versus Dye-Labeled Species. *Molecules* **23**, 3105 (2018)

[14] S. Weiss. Fluorescence spectroscopy of single biomolecules. *Science* **283**, 1676–1683 (1999)

[15] B. Schuler, E. A. Lipman, and W. A. Eaton. Probing the free-energy surface for protein folding with single-molecule fluorescence spectroscopy. *Nature* **419**, 743–747 (2002)

[16] P. R. Banerjee and A. A. Deniz. Shedding light on protein folding landscapes by single-molecule fluorescence. *Chemical Society Reviews* **43**, 1172–1188 (2014)

[17] M. Dimura et al. Quantitative FRET studies and integrative modeling unravel the structure and dynamics of biomolecular systems. *Current Opinion in Structural Biology* **40**, 163–185 (2016)

[18] E. Lerner et al. Toward dynamic structural biology: Two decades of single-molecule Förster resonance energy transfer. *Science* **359** (2018)

[19] D. M. Chudakov et al. Fluorescent Proteins and Their Applications in Imaging Living Cells and Tissues. *Physiological Reviews* **90**, 1103–1163 (2010)

[20] A. Ibraheem and R. E. Campbell. Designs and applications of fluorescent protein-based biosensors. *Current Opinion in Chemical Biology* **14**, 30–36 (2010)

[21] L. Lindenburg and M. Merkx. Engineering Genetically Encoded FRET Sensors. *Sensors* **14**, 11691–11713 (2014)

[22] V. L. Kolossov et al. Engineering Redox-Sensitive Linkers for Genetically Encoded FRET-Based Biosensors. *Experimental Biology and Medicine* **233**, 238–248 (2008)

[23] B. Philipps, J. Hennecke, and R. Glockshuber. FRET-based in Vivo Screening for Protein Folding and Increased Protein Stability. *Journal of Molecular Biology* **327**, 239–249 (2003)

[24] S. Mukherjee et al. A novel biosensor to study cAMP dynamics in cilia and flagella. *eLife* **5** (2016)

[25] A. Miyawaki et al. Fluorescent indicators for Ca2+ based on green fluorescent proteins and calmodulin. *Nature* **388**, 882–887 (1997)

[26] M. Fehr et al. In vivo imaging of the dynamics of glucose uptake in the cytosol of COS-7 cells by fluorescent nanosensors. *Journal of Biological Chemistry* **278**, 19127–19133 (2003)

[27] S. M. Müller et al. Quantification of Förster resonance energy transfer by monitoring sensitized emission in living plant cells. *Frontiers in Plant Science* **4**, 413 (2013)

[28] N. Komatsu et al. Development of an optimized backbone of FRET biosensors for kinases and GTPases. *Molecular Biology of the Cell* **22**, 4647–4656 (2011)

[29] R. E. Campbell. Fluorescent-protein-based biosensors: modulation of energy transfer as a design principle. *Analytical Chemistry* **81**, 5972–5979 (2009)

[30] K. Deuschle et al. Construction and optimization of a family of genetically encoded metabolite sensors by semirational protein engineering. *Protein Science* **14**, 2304–2314 (2005)

[31] S. B. Zimmerman and A. P. Minton. Macromolecular crowding: biochemical, biophysical, and physiological consequences. *Annual Review of Biophysics and Biomolecular Structure* **22**, 27–65 (1993)

[32] R. Ellis. Macromolecular crowding: obvious but underappreciated. *Trends in Biochemical Sciences* **26**, 597–604 (2001)

[33] J. Ries et al. A comprehensive framework for fluorescence cross-correlation spectroscopy. *New Journal of Physics* **12**, 113009 (2010)

[34] A. Orte, R. Clarke, and D. Klenerman. Single-molecule two-colour coincidence detection to probe biomolecular associations. *Biochemical Society Transactions* **38**, 914–918 (2010)

[35] A. Katranidis and J. Fitter. Single-Molecule Techniques and Cell-Free Protein Synthesis: A Perfect Marriage. *Analytical Chemistry* **91**, 2570–2576 (2019)

[36] H. Höfig et al. Inter-Dye Distance Distributions Studied by a Combination of Single-Molecule FRET-Filtered Lifetime Measurements and a Weighted Accessible Volume (wAV) Algorithm. *Molecules* **19**, 19269–19291 (2014)

[37] H. Höfig et al. Genetically Encoded Förster Resonance Energy Transfer-Based Biosensors Studied on the Single-Molecule Level. *ACS Sensors* **3**, 1462–1470 (2018)

[38] B. Liu et al. Design and Properties of Genetically Encoded Probes for Sensing Macromolecular Crowding. *Biophysical Journal* **112**, 1929–1939 (2017)

[39] H. Ohashi et al. A Highly Controllable Reconstituted Cell-Free System -a Breakthrough in Protein Synthesis Research. *Current Pharmaceutical Biotechnology* **11**, 267–271 (2010)

[40] C. Remeş. Translation initiation with 70S ribosomes : a single molecule study. PhD thesis, RWTH Aachen University (2017)

[41] R. Y. Tsien. The green fluorescent protein. *Annual Review of Biochemistry* **67**, 509–544 (1998)

[42] F. Cymer et al. Exploration of the arrest peptide sequence space reveals arrest-enhanced variants. *Journal of Biological Chemistry* **290**, 10208–10215 (2015)

[43] N. Kempf et al. A Novel Method to Evaluate Ribosomal Performance in Cell-Free Protein Synthesis Systems. *Scientific Reports* **7**, 46753 (2017)

[44] C. E. Aitken, R. A. Marshall, and J. D. Puglisi. An oxygen scavenging system for improvement of dye stability in single-molecule fluorescence experiments. *Biophysical Journal* **94**, 1826–1835 (2008)

[45] R. Ledesch. Simultaneous dual-color imaging on singel-molecule level on a Widefield microscope and applications. PhD thesis, RWTH Aachen University (2018)

[46] G. Allodi. FMINUIT-A binding to Minuit for Matlab, Octave & Scilab (1996-2010)

[47] W. Humphrey, A. Dalke, and K. Schulten. VMD: Visual molecular dynamics. *Journal of Molecular Graphics* **14**, 33–38 (1996)

[48] Y. Engelborghs and A. J. Visser (editors). Fluorescence Spectroscopy and Microscopy. Methods in Molecular Biology. Humana Press, Totowa, NJ (2014). ISBN 978-1-62703-648-1

[49] J. R. Lakowicz. Principles of fluorescence spectroscopy. Springer, New York, 3rd edition (2006). ISBN 0-387-31278-1

[50] J. STARK. Ultra-violet Fluorescence of Benzene. *Nature* **75**, 295 (1907)

[51] M. Sauer, J. Hofkens, and J. Enderlein. Handbook of fluorescence spectroscopy and imaging: From ensemble to single molecules. Wiley-VCH, Weinheim (2008). ISBN 9783527316694

[52] J. Enderlein. Electrodynamics of Fluorescence: Tutorial, joerg-enderlein.de

[53] D. M. Jameson, J. C. Croney, and P. D. Moens. Fluorescence: Basic concepts, practical aspects, and some anecdotes. In G. Marriott and I. Parker (editors), Biophotonics, volume 360 of *Methods in Enzymology*, 1–43. Academic Press, Amsterdam and Boston (2003). ISBN 9780121822637

[54] M. Kasha. Characterization of electronic transitions in complex molecules. *Discussions of the Faraday Society* **9**, 14 (1950)

[55] B. Valeur and M. N. Berberan-Santos. Molecular fluorescence: Principles and applications. Wiley-VCH, Weinheim, 2. edition edition (2013). ISBN 9783527650019

[56] C. Gell, D. Brockwell, and D. A. Smith. Handbook of single molecule fluorescence spectroscopy. Oxford University Press, Oxford and New York (2013). ISBN 9780199673841

[57] J. Yguerabide. Nanosecond fluorescence spectroscopy of macromolecules. In Enzyme Structure, Part C, volume 26 of *Methods in Enzymology*, 498–578. Elsevier (1972). ISBN 9780121818890

[58] J. Vogelsang et al. A reducing and oxidizing system minimizes photobleaching and blinking of fluorescent dyes. *Angewandte Chemie (International ed.)* **47**, 5465–5469 (2008)

[59] W. E. Moerner. Single-molecule optical spectroscopy of autofluorescent proteins. *Journal of Chemical Physics* **117**, 10925 (2002)

[60] L. A. Campos et al. A photoprotection strategy for microsecond-resolution single-molecule fluorescence spectroscopy. *Nature Methods* **8**, 143–147 (2011)

[61] T. Förster. Zwischenmolekulare Energiewanderung und Fluoreszenz. *Annalen der Physik* **437**, 55–75 (1948)

[62] I. Z. Steinberg. Long-range nonradiative transfer of electronic excitation energy in proteins and polypeptides. *Annual Review of Biochemistry* **40**, 83–114 (1971)

[63] L. Stryer. Fluorescence Energy Transfer as a Spectroscopic Ruler. *Annual Review of Biochemistry* **47**, 819–846 (1978)

[64] O. Shimomura, F. H. Johnson, and Y. Saiga. Extraction, Purification and Properties of Aequorin, a Bioluminescent Protein from the Luminous Hydromedusan,Aequorea. *Journal of Cellular and Comparative Physiology* **59**, 223–239 (1962)

[65] D. C. Prasher et al. Primary structure of the Aequorea victoria green-fluorescent protein. *Gene* **111**, 229–233 (1992)

[66] NobelPrize.org. The Nobel Prize in Chemistry 2008 (2008)

[67] C. W. Cody et al. Chemical structure of the hexapeptide chromophore of the Aequorea green-fluorescent protein. *Biochemistry* **32**, 1212–1218 (1993)

[68] T. D. Craggs. Green fluorescent protein: structure, folding and chromophore maturation. *Chemical Society Reviews* **38**, 2865–2875 (2009)

[69] S. G. Olenych et al. The fluorescent protein color palette. *Current Protocols in Cell Biology* **21**, 1–34 (2007)

[70] N. Naredi-Rainer et al. Confocal Microscopy. In U. Kubitscheck (editor), Fluorescence microscopy, 165–202. Wiley-VCH, Weinheim (2017). ISBN 9783527338375

[71] J. W. Dobrucki and U. Kubitscheck. Fluorescence Microscopy. In U. Kubitscheck (editor), Fluorescence microscopy, 85–132. Wiley-VCH, Weinheim (2017). ISBN 9783527338375

[72] M. Wahl. Time-Correlated Single Photon Counting: Technical Note, PicoQuant GmbH, Berlin (2014)

[73] L. Novotny and B. Hecht. Principles of nano-optics. Cambridge University Press, Cambridge, 2. edition (2012). ISBN 9781107005464

[74] R. Rigler et al. Fluorescence correlation spectroscopy with high count rate and low background: analysis of translational diffusion. *European Biophysics Journal* **22**, 169–175 (1993)

[75] F. Pampaloni and J. Enderlein. Gaussian, Hermite-Gaussian, and Laguerre-Gaussian beams: A primer, https://arxiv.org/abs/physics/0410021

[76] S. T. Hess and W. W. Webb. Focal volume optics and experimental artifacts in confocal fluorescence correlation spectroscopy. *Biophysical Journal* **83**, 2300–2317 (2002)

[77] J. Enderlein and C. Zander. Theoretical Foundations in Single Molecule Detection in Solution. In C. Zander, J. Enderlein, and R. A. Keller (editors), Single molecule detection in solution, 21–68. Wiley-VCH, Berlin (2002). ISBN 3527403108

[78] J. Enderlein. Theoretical study of detection of a dipole emitter through an objective with high numerical aperture. *Optics Letters* **25**, 634–636 (2000)

[79] V. Buschmann et al. Quantitative FCS: Determination of the Confocal Volume by FCS and Bead Scanning with the MicroTime 200: Application Note

[80] W. Becker. The bh TCSPC Handbook. Becker & Hickl GmbH, Berlin (2017)

[81] N. Boens, M. Ameloot, and B. Valeur. Practical Time-Resolved Fluorescence Spectroscopy: Avoiding Artifacts and Using Lifetime Standards. In U. Resch-Genger (editor), Standardization and quality assurance in fluorescence measurements I, volume 5 of *Springer series on fluorescence*, 215–232. Springer, Berlin and London (2008). ISBN 978-3-540-75206-6

[82] M. Wahl and S. Orthaus-Müller. Time Tagged Time-Resolved Fluorescence Data Collection in Life Sciences: Technical Note. PicoQuant GmbH, Berlin (2014)

[83] B. K. Müller et al. Pulsed Interleaved Excitation. *Biophysical Journal* **89**, 3508–3522 (2005)

[84] E. Haustein and P. Schwille. Fluorescence Correlation Spectroscopy: Novel Variations of an Established Technique. *Annual Review of Biophysics and Biomolecular Structure* **36**, 151–169 (2007)

[85] P. Schwille and E. Haustein. Fluorescence Correlation Spectroscopy: An Introduction to its Concepts and Applications, uni-goettingen.de/de/499370.html

[86] G. Grosso and G. Pastori Parravicini. Solid state physics. Elsevier, Amsterdam, 2. edition (2014). ISBN 978-0-12-385030-0

[87] J. G. Sinaj. Introduction to ergodic theory, volume 18 of *Mathematical notes*. Princeton Univ. Press, Princeton (1977). ISBN 0691081824

[88] J. Widengren and Ü. Mets. Conceptual Basis of Fluorescence Correlation Spectroscopy and Related Techniques as Tools in Bioscience. In C. Zander, J. Enderlein, and R. A. Keller (editors), Single molecule detection in solution, 69–120. Wiley-VCH, Berlin (2002). ISBN 3527403108

[89] F. L. H. Brown. Generating Functions for Single-Molecule Statistics. In E. Barkai et al. (editors), Theory and evaluation of single-molecule signals, 61–92. World Scientific, New Jersey (2008). ISBN 9812793488

[90] C. Eggeling et al. Data registration and selective single-molecule analysis using multiparameter fluorescence detection. *Journal of Biotechnology* **86**, 163–180 (2001)

[91] R. W. Clarke, A. Orte, and D. Klenerman. Optimized Threshold Selection for Single-Molecule Two-Color Fluorescence Coincidence Spectroscopy. *Analytical Chemistry* **79**, 2771–2777 (2007)

[92] J. R. Fries et al. Quantitative Identification of Different Single Molecules by Selective Time-Resolved Confocal Fluorescence Spectroscopy. *Journal of Physical Chemistry A* **102**, 6601–6613 (1998)

[93] M. Eigen and R. Rigler. Sorting single molecules: Application to diagnostics and evolutionary biotechnology. *Proceedings of the National Academy of Sciences* **91**, 5740–5747 (1994)

[94] E. Nir et al. Shot-noise limited single-molecule FRET histograms: comparison between theory and experiments. *Journal of Physical Chemistry B* **110**, 22103–22124 (2006)

[95] B. Nagel, H. Dellweg, and L. M. Gierasch. Glossary for chemists of terms used in biotechnology: (IUPAC Recommendations 1992). *Pure and Applied Chemistry* **64**, 143–168 (1992)

[96] D. R. Thévenot et al. Electrochemical biosensors: recommended definitions and classification. *Biosensors and Bioelectronics* **16**, 121–131 (2001)

[97] F.-G. Bănică. Chemical sensors and biosensors: Fundamentals and applications. Wiley, Hoboken, NJ and Chichester (2012). ISBN 9780470710661

[98] L. C. Clark and C. Lyons. Electrode systems for continous monitoring in cardiovascular surgery. *Annals of the New York Academy of Sciences* 29–45 (1962)

[99] H. J. Carlson and R. E. Campbell. Genetically encoded FRET-based biosensors for multiparameter fluorescence imaging. *Current Opinion in Biotechnology* **20**, 19–27 (2009)

[100] S. Zadran et al. Fluorescence resonance energy transfer (FRET)-based biosensors: visualizing cellular dynamics and bioenergetics. *Applied Microbiology and Biotechnology* **96**, 895–902 (2012)

[101] A. Volkmer et al. One- and Two-Photon Excited Fluorescence Lifetimes and Anisotropy Decays of Green Fluorescent Proteins. *Biophysical Journal* **78**, 1589–1598 (2000)

[102] T. Ansbacher et al. Calculation of transition dipole moment in fluorescent proteins–towards efficient energy transfer. *Physical Chemistry Chemical Physics* **14**, 4109–4117 (2012)

[103] S. Okada, K. Ota, and T. Ito. Circular permutation of ligand-binding module improves dynamic range of genetically encoded FRET-based nanosensor. *Protein Science* **18**, 2518–2527 (2009)

[104] J. Otten et al. A FRET-based biosensor for the quantification of glucose in culture supernatants of mL scale microbial cultivations. *Microbial Cell Factories* **18**, 143 (2019)

[105] V. Steffen et al. A Toolbox of Genetically Encoded FRET-Based Biosensors for Rapid l-Lysine Analysis. *Sensors* **16** (2016)

[106] R. Moussa et al. An evaluation of genetically encoded FRET-based biosensors for quantitative metabolite analyses in vivo. *Journal of Biotechnology* **191**, 250–259 (2014)

[107] S. B. Zimmerman and S. O. Trach. Estimation of macromolecule concentrations and excluded volume effects for the cytoplasm of Escherichia coli. *Journal of Molecular Biology* **222**, 599–620 (1991)

[108] A. J. Boersma, I. S. Zuhorn, and B. Poolman. A sensor for quantification of macromolecular crowding in living cells. *Nature Methods* **12**, 227–229 (2015)

[109] G. Faccio et al. Encapsulation of FRET-based glucose and maltose biosensors to develop functionalized silica nanoparticles. *The Analyst* **141**, 3982–3984 (2016)

[110] N. O. Junker et al. Impact of Molecular Crowding on Translational Mobility and Conformational Properties of Biological Macromolecules. *Journal of Physical Chemistry B* **123**, 4477–4486 (2019)

[111] J. Groen et al. Associative Interactions in Crowded Solutions of Biopolymers Counteract Depletion Effects. *Journal of the American Chemical Society* **137**, 13041–13048 (2015)

[112] S. Brasselet et al. Single-Molecule Fluorescence Resonant Energy Transfer in Calcium Concentration Dependent Cameleon. *Journal of Physical Chemistry B* **104**, 3676–3682 (2000)

[113] I. König et al. Single-molecule spectroscopy of protein conformational dynamics in live eukaryotic cells. *Nature Methods* **12**, 773–779 (2015)

[114] D. Sinnecker et al. Reversible photobleaching of enhanced green fluorescent proteins. *Biochemistry* **44**, 7085–7094 (2005)

[115] P. J. Cranfill et al. Quantitative assessment of fluorescent proteins. *Nature Methods* **13**, 557–563 (2016)

[116] D. M. Carey and G. M. Korenowski. Measurement of the Raman spectrum of liquid water. *The Journal of Chemical Physics* **108**, 2669–2675 (1998)

[117] J. van Rheenen, M. Langeslag, and K. Jalink. Correcting Confocal Acquisition to Optimize Imaging of Fluorescence Resonance Energy Transfer by Sensitized Emission. *Biophysical Journal* **86**, 2517–2529 (2004)

[118] J. Hohlbein, T. D. Craggs, and T. Cordes. Alternating-laser excitation: single-molecule FRET and beyond. *Chemical Society Reviews* **43**, 1156 (2014)

[119] V. Kudryavtsev et al. Combining MFD and PIE for Accurate Single-Pair Förster Resonance Energy Transfer Measurements. *ChemPhysChem* **13**, 1060–1078 (2012)

[120] M. L. Markwardt et al. An improved cerulean fluorescent protein with enhanced brightness and reduced reversible photoswitching. *PLoS ONE* **6**, e17896 (2011)

[121] O. Griesbeck et al. Reducing the Environmental Sensitivity of Yellow Fluorescent Protein. *Journal of Biological Chemistry* **276**, 29188–29194 (2001)

[122] D. Kempe et al. Accurate Fluorescence Quantum Yield Determination by Fluorescence Correlation Spectroscopy. *Journal of Physical Chemistry B* **119**, 4668–4672 (2015)

[123] S. Kalinin et al. On the Origin of Broadening of Single-Molecule FRET Efficiency Distributions beyond Shot Noise Limits. *Journal of Physical Chemistry B* **114**, 6197–6206 (2010)

[124] A. Kyrychenko et al. Joint refinement of FRET measurements using spectroscopic and computational tools. *Analytical Biochemistry* **522**, 1–9 (2017)

[125] I. V. Gopich and A. Szabo. Single-Molecule FRET with Diffusion and Conformational Dynamics. *Journal of Physical Chemistry B* **111**, 12925–12932 (2007)

[126] T. Torres and M. Levitus. Measuring conformational dynamics: a new FCS-FRET approach. *Journal of Physical Chemistry B* **111**, 7392–7400 (2007)

[127] S. Sindbert et al. Accurate Distance Determination of Nucleic Acids via Förster Resonance Energy Transfer: Implications of Dye Linker Length and Rigidity. *Journal of the American Chemical Society* **133**, 2463–2480 (2011)

[128] S. Kalinin et al. A toolkit and benchmark study for FRET-restrained high-precision structural modeling. *Nature Methods* **9**, 1218–1225 (2012)

[129] T. J. Amiss et al. Engineering and rapid selection of a low-affinity glucose/galactose-binding protein for a glucose biosensor. *Protein Science* **16**, 2350–2359 (2007)

[130] R. M. de Lorimier et al. Construction of a fluorescent biosensor family. *Protein Science* **11**, 2655–2675 (2002)

[131] J. Kuriyan, B. Konforti, and D. Wemmer. The molecules of life: Physical and chemical principles. GS Garland Science, New York, NY (2013). ISBN 978-0-8153-4188-8

[132] T. D. Pollard, W. C. Earnshaw, and J. Lippincott-Schwartz. Cell biology. Saunders/Elsevier, Philadelphia, 2. edition (2008). ISBN 9781416022558

[133] E. Kinoshita, E. Kinoshita-Kikuta, and T. Koike. The Cutting Edge of Affinity Electrophoresis Technology. *Proteomes* **3**, 42–55 (2015)

[134] S. Zeng et al. Nanomaterials enhanced surface plasmon resonance for biological and chemical sensing applications. *Chemical Society Reviews* **43**, 3426–3452 (2014)

[135] M. W. Freyer and E. A. Lewis. Isothermal Titration Calorimetry: Experimental Design, Data Analysis, and Probing Macromolecule/Ligand Binding and Kinetic Interactions. In Biophysical Tools for Biologists, Volume One: In Vitro Techniques, volume 84 of *Methods in Cell Biology*, 79–113. Elsevier (2008). ISBN 9780123725202

[136] C. Eliscovich, S. M. Shenoy, and R. H. Singer. Imaging mRNA and protein interactions within neurons. *Proceedings of the National Academy of Sciences* **114**, E1875–E1884 (2017)

[137] J. D. Larson, M. L. Rodgers, and A. A. Hoskins. Visualizing cellular machines with colocalization single molecule microscopy. *Chemical Society Reviews* **43**, 1189–1200 (2014)

[138] P. Schwille, F. J. Meyer-Almes, and R. Rigler. Dual-color fluorescence cross-correlation spectroscopy for multicomponent diffusional analysis in solution. *Biophysical Journal* **72**, 1878–1886 (1997)

[139] H. S. Rye. Application of fluorescence resonance energy transfer to the GroEL-GroES chaperonin reaction. *Methods* **24**, 278–288 (2001)

[140] H. Höfig et al. Brightness-gated two-color coincidence detection unravels two distinct mechanisms in bacterial protein translation initiation. *Communications Biology* **2**, 459 (2019)

[141] P. Wang et al. The Beauty and Utility of DNA Origami. *Chem* **2**, 359–382 (2017)

[142] J. J. Schmied et al. Fluorescence and super-resolution standards based on DNA origami. *Nature Methods* **9**, 1133–1134 (2012)

[143] I. Yahiatène et al. Correlation-Matrix Analysis of Two-Color Coincidence Events in Single-Molecule Fluorescence Experiments. *Analytical Chemistry* **84**, 2729–2736 (2012)

[144] N. Vandenberk et al. Evaluation of Blue and Far-Red Dye Pairs in Single-Molecule Förster Resonance Energy Transfer Experiments. *Journal of Physical Chemistry B* **122**, 4249–4266 (2018)

[145] T. Ha and P. Tinnefeld. Photophysics of Fluorescence Probes for Single Molecule Biophysics and Super-Resolution Imaging. *Annual Review of Physical Chemistry* **63**, 595–617 (2012)

[146] I. V. Gopich. Concentration Effects in "Single-Molecule" Spectroscopy. *Journal of Physical Chemistry B* **112**, 6214–6220 (2008)

[147] L. Edman, U. Mets, and R. Rigler. Conformational transitions monitored for single molecules in solution. *Proceedings of the National Academy of Sciences* **93**, 6710–6715 (1996)

[148] J. Enderlein et al. Molecular Shot Noise, Burst Size Distribution, and Single-Molecule Detection in Fluid Flow: Effects of Multiple Occupancy. *Journal of Physical Chemistry A* **102**, 6089–6094 (1998)

[149] A. Orte, R. W. Clarke, and D. Klenerman. Fluorescence Coincidence Spectroscopy for Single-Molecule Fluorescence Resonance Energy-Transfer Measurements. *Analytical Chemistry* **80**, 8389–8397 (2008)

[150] F. Crick. Central dogma of molecular biology. *Nature* **227**, 561–563 (1970)

[151] M. W. Nirenberg and J. H. Matthaei. The dependence of cell-free protein synthesis in E. coli upon naturally occurring or synthetic polyribonucleotides. *Proceedings of the National Academy of Sciences* **47**, 1588–1602 (1961)

[152] M. S. Evans et al. Homogeneous stalled ribosome nascent chain complexes produced in vivo or in vitro. *Nature Methods* **2**, 757–762 (2005)

[153] S. Uemura et al. Single-molecule imaging of full protein synthesis by immobilized ribosomes. *Nucleic Acids Research* **36**, e70 (2008)

[154] A. Katranidis et al. Fast biosynthesis of GFP molecules: a single-molecule fluorescence study. *Angewandte Chemie (International ed.)* **48**, 1758–1761 (2009)

[155] D. D. Boehr, R. Nussinov, and P. E. Wright. The role of dynamic conformational ensembles in biomolecular recognition. *Nature Chemical Biology* **5**, 1–8 (2009)

[156] D. E. Koshland. Application of a Theory of Enzyme Specificity to Protein Synthesis. *Proceedings of the National Academy of Sciences* **44**, 98–104 (1958)

[157] E. Sisamakis et al. Accurate Single-Molecule FRET Studies Using Multiparameter Fluorescence Detection. *Methods in Enzymology* **475**, 455–514 (2010)

[158] T. Ha et al. Initiation and re-initiation of DNA unwinding by the Escherichia coli Rep helicase. *Nature* **419**, 638–641 (2002)

[159] Y. Ohta et al. Nontrivial Effect of the Color-Exchange of a Donor/Acceptor Pair in the Engineering of Förster Resonance Energy Transfer (FRET)-Based Indicators. *ACS Chemical Biology* **11**, 1816–1822 (2016)

[160] T. Nagai et al. Expanded dynamic range of fluorescent indicators for Ca(2+) by circularly permuted yellow fluorescent proteins. *Proceedings of the National Academy of Sciences* **101**, 10554–10559 (2004)

[161] H. D. Mertens et al. Conformational Analysis of a Genetically Encoded FRET Biosensor by SAXS. *Biophysical Journal* **102**, 2866–2875 (2012)

[162] G. Faccio and S. Salentinig. Enzyme-Triggered Dissociation of a FRET-Based Protein Biosensor Monitored by Synchrotron SAXS. *Biophysical Journal* **113**, 1731–1737 (2017)

[163] I. Reinartz et al. Simulation of FRET dyes allows quantitative comparison against experimental data. *The Journal of Chemical Physics* **148**, 123321 (2018)

[164] S. S. Vogel, B. W. van der Meer, and P. S. Blank. Estimating the distance separating fluorescent protein FRET pairs. *Methods* **66**, 131–138 (2014)

[165] B. W. van der Meer, D. M. van der Meer, and S. S. Vogel. Optimizing the Orientation Factor Kappa-Squared for More Accurate FRET Measurements. In I. Medintz and N. Hildebrandt (editors), FRET - Förster resonance energy transfer, volume 127, 63–104. Wiley-VCH, Weinheim (2014). ISBN 9783527656028

[166] N. M. Green. Avidin. In C. Anfinsen, J. T. Edsall, and F. M. Richards (editors), Advances in Protein Chemistry, volume 29, 85–133. Academic Press (1975). ISBN 0065-3233

[167] N. Michael Green. Avidin and streptavidin. In M. Wilchek and E. A. Bayer (editors), Avidin-Biotin Technology, volume 184 of *Methods in Enzymology*, 51–67. Academic Press (1990)

[168] P. Tinnefeld. Single-molecule detection: Breaking the concentration barrier. *Nature Nanotechnology* **8**, 480–482 (2013)

[169] P. Holzmeister et al. Breaking the concentration limit of optical single-molecule detection. *Chemical Society Reviews* **43**, 1014–1028 (2014)

[170] K. Bacia and P. Schwille. Practical guidelines for dual-color fluorescence cross-correlation spectroscopy. *Nature Protocols* **2**, 2842–2856 (2007)

A Appendix: FRET-Based Biosensors

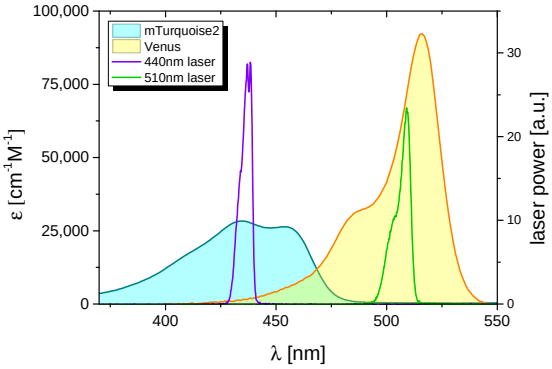

Figure A.1: Absorption spectra of mTurqouise2 (CFP) and Citrtine (YFP) together with emission spectra of 440 nm (40 Mhz, 85 % of maximum power) and 510 nm (40 Mhz, 64 % of maximum power) laser (provided by manufacturer).

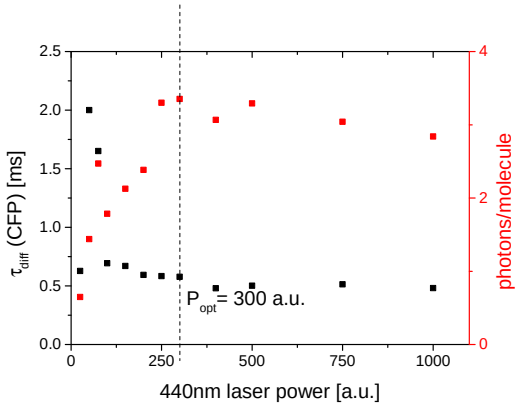

Figure A.2: Average CFP dwell time and sum of CFP and YFP photons emitted per molecule.

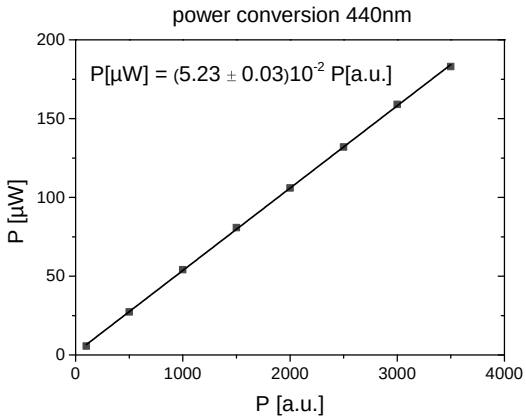

Figure A.3: Conversion of power readings obtained by power diode (*a.u.*) to real power (μW). Power was measured at the objective position using a power meter.

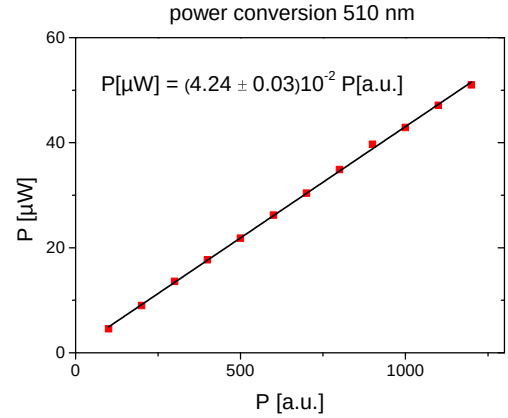

Figure A.4: Conversion of power readings obtained by power diode (*a.u.*) to real power (μW). Power was measured at the objective position using a power meter.

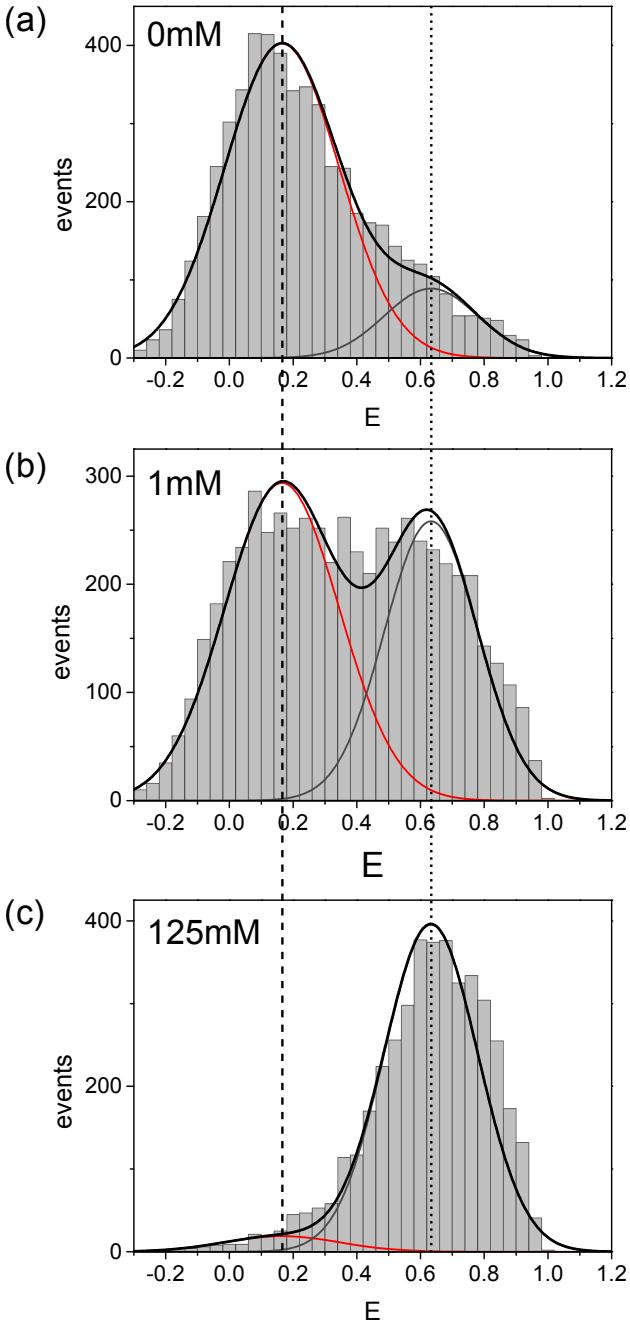

Figure A.5: smFRET histograms of glucose sensor construct no. 3 (a) without glucose, (b) at glucose concentration equal to K_D and (c) at saturating glucose concentration of 125 mM. Adopted from [37].

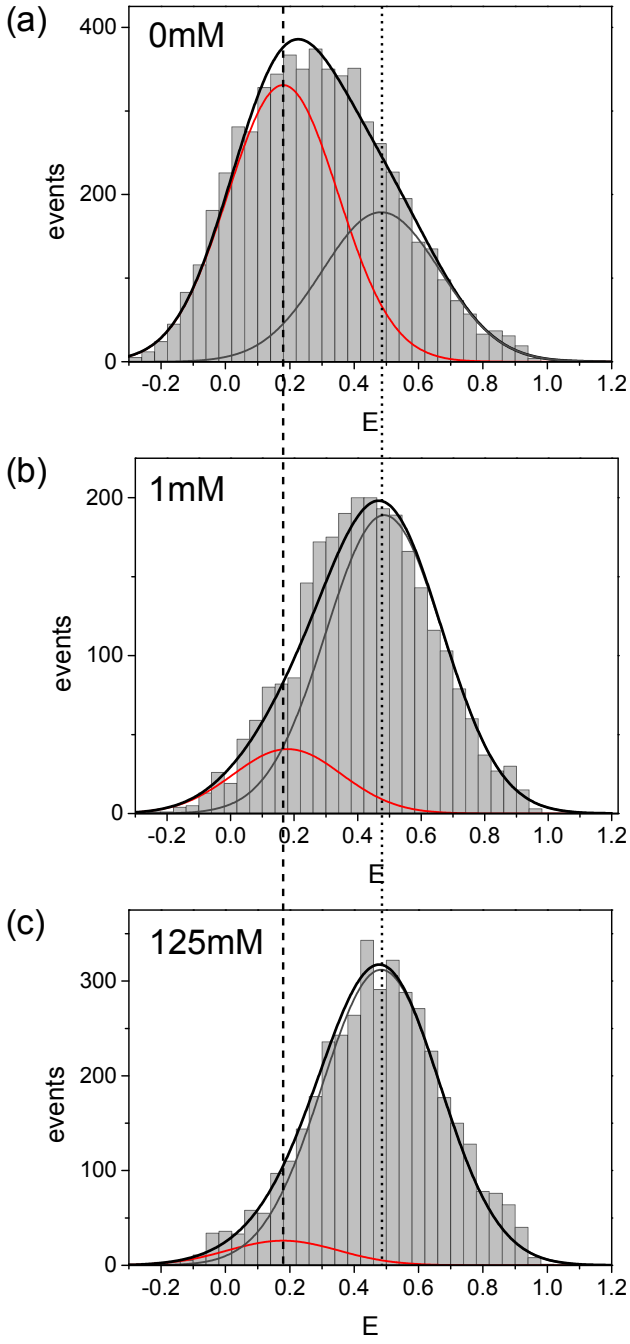

Figure A.6: smFRET histograms of glucose sensor construct no. 4 (a) without glucose, (b) at glucose concentration equal to K_D and (c) at saturating glucose concentration of 125 mM. Adopted from [37].

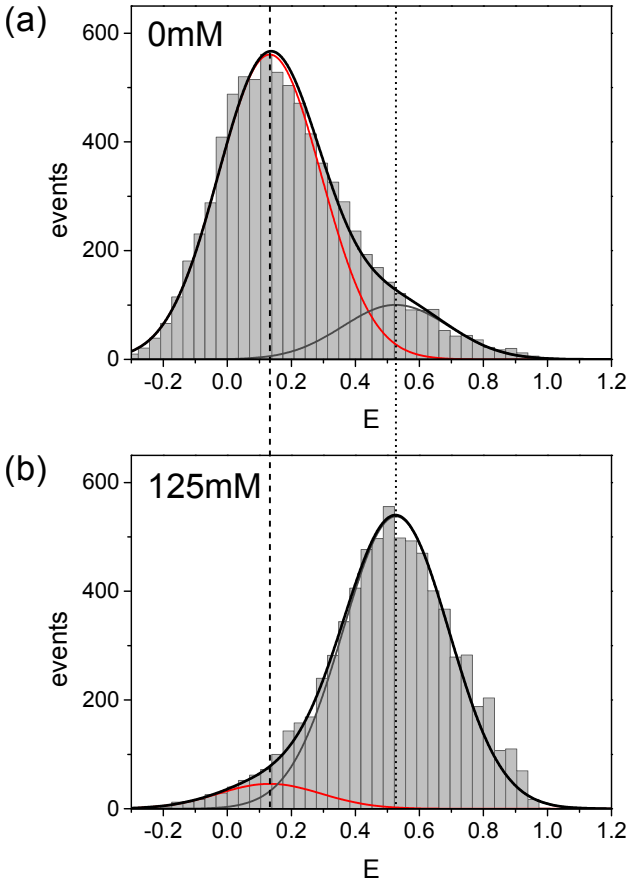

Figure A.7: smFRET histograms of glucose sensor construct no. 5 (a) without glucose, (b) at glucose concentration equal to K_D and (c) at saturating glucose concentration of 125 mM. Adopted from [37].

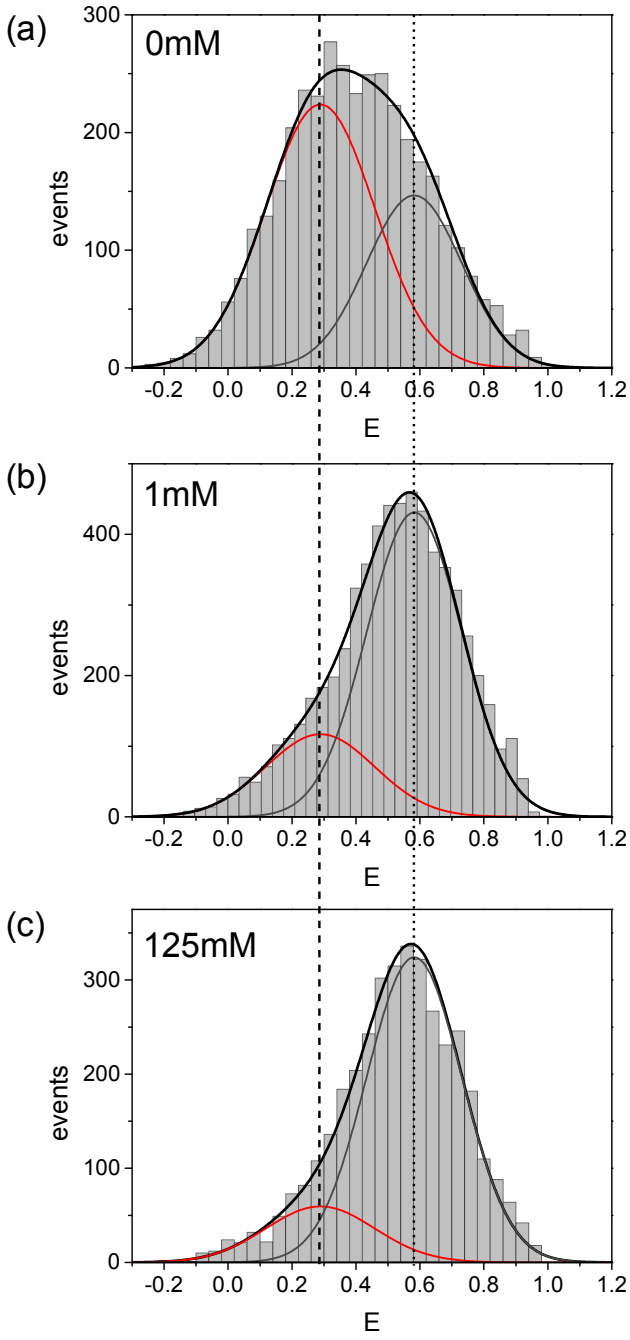

Figure A.8: smFRET histograms of glucose sensor construct no. 8 (a) without glucose, (b) at glucose concentration equal to K_D and (c) at saturating glucose concentration of 125 mM. Adopted from [37].

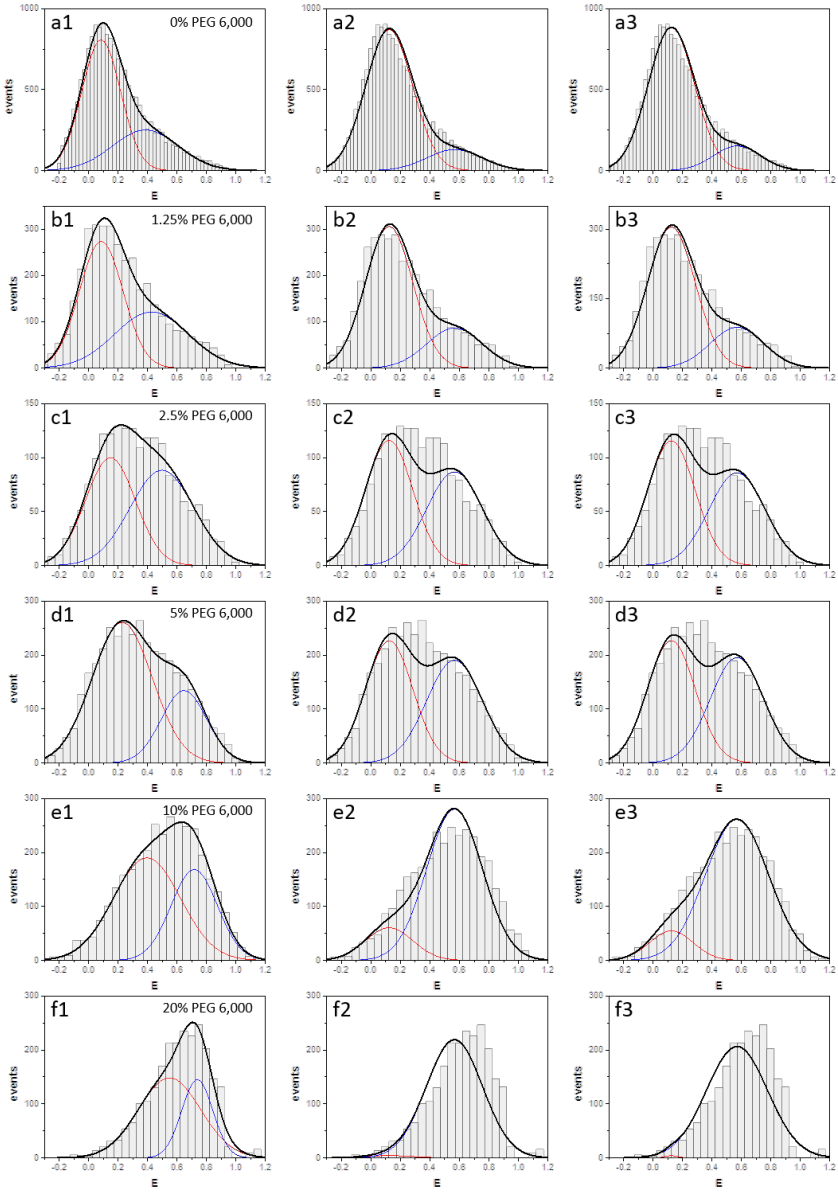

Figure A.9: smFRET histograms of glucose sensor no. 2 in various concentrations of PEG 6,000. Each row contains 3 replica of the same histogram fitted withthe sum of two Gaussian distributions. In the left column each histogram was fitted individually, whereas the histograms were fitted globally with fixed center positions and widths (middel column) or only with fixed center positions (right column). The full data set is only reasonably described by individual fits which is most apparent for the highest PEG concentration. Adopted from [37].

B Appendix: Two-Color Coincidence Detection

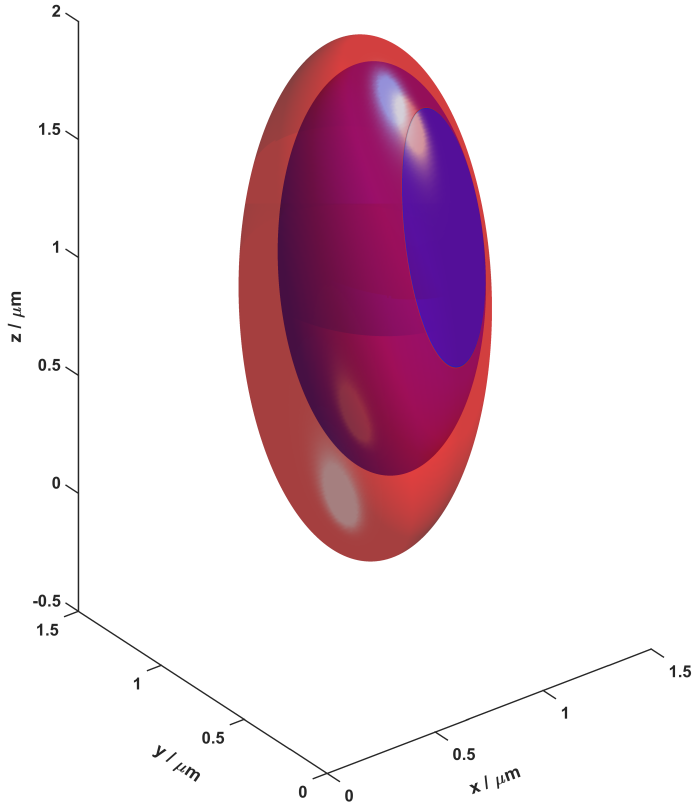

Figure B.1: Reconstruction of blue and red confocal volume based on x-y, x-z, and y-z raster scan of TetraSpeck bead deposited on cover slip. Adopted from [140].

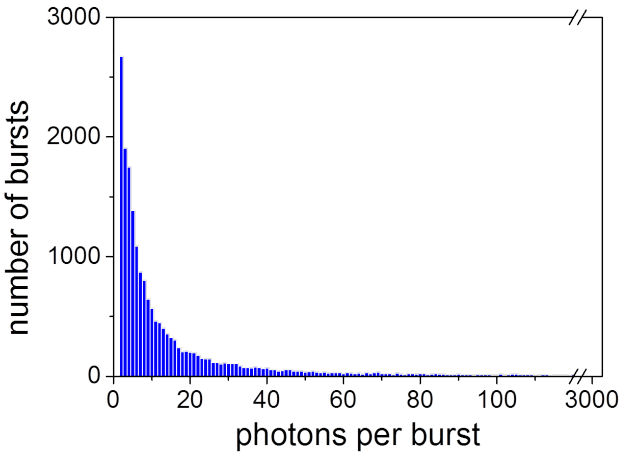

Figure B.2: Distribution of burst brightness of blue channel for nano-bead reference. Adopted from [140].

reference	f_{sat}	Δf	$n_{1/2}$
TetraSpeck beads	1 ± 0.0001	0.4481 ± 0.0005	0.0472 ± 0.0001
nano-beads	1 ± 0.0002	0.6431 ± 0.0006	0.1418 ± 0.0004
dsDNA Alexa 488 / Atto 647N	0.9409 ± 0.0006	0.494 ± 0.001	0.351 ± 0.002
dsDNA Alexa 488 / Alexa 647	0.9549 ± 0.0006	0.421 ± 0.001	0.345 ± 0.002

Table B.1: Fitting parameters of red coincidence fraction as a function of brightness threshold (see Eq. 5.5).

reference	f_{sat}	Δf	$n_{1/2}$
TetraSpeck beads	1 ± 0.0003	0.496$pm0.001	0.0457 ± 0.0004
nano-beads	0.9995 ± 0.0001	0.4609$pm0.0005	0.1149 ± 0.0003
dsDNA Alexa 488 / Atto 647N	0.9264 ± 0.0006	0.275$pm0.001	0.307 ± 0.003
dsDNA Alexa 488 / Alexa 647	0.8056 ± 0.0007	0.344$pm0.001	0.342 ± 0.003

Table B.2: Fitting parameters of blue coincidence fraction as a function of brightness threshold (see Eq. 5.5).

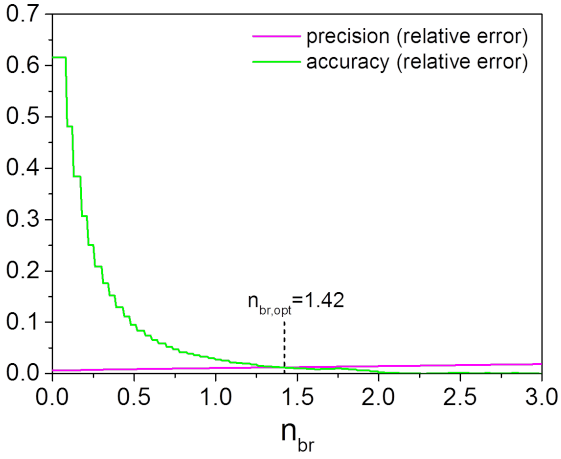

Figure B.3: Determination of optimal brightness threshold as intersection of relative precision and accuracy. Data shown for blue channel of nano-bead reference.

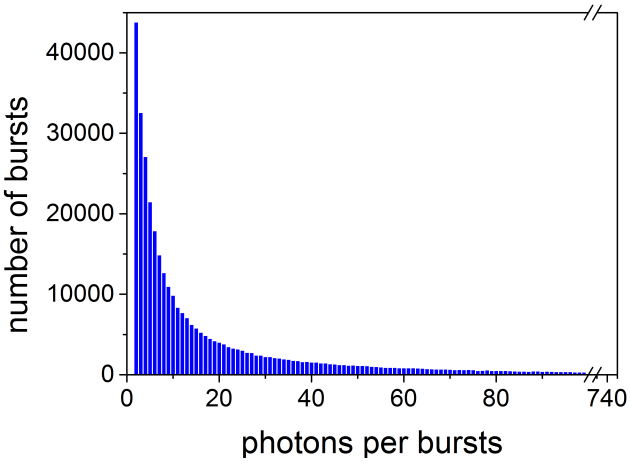

Figure B.4: Distribution of burst brightness of blue channel for dsDNA (Alexa488/Atto647N) reference. Adopted from [140].

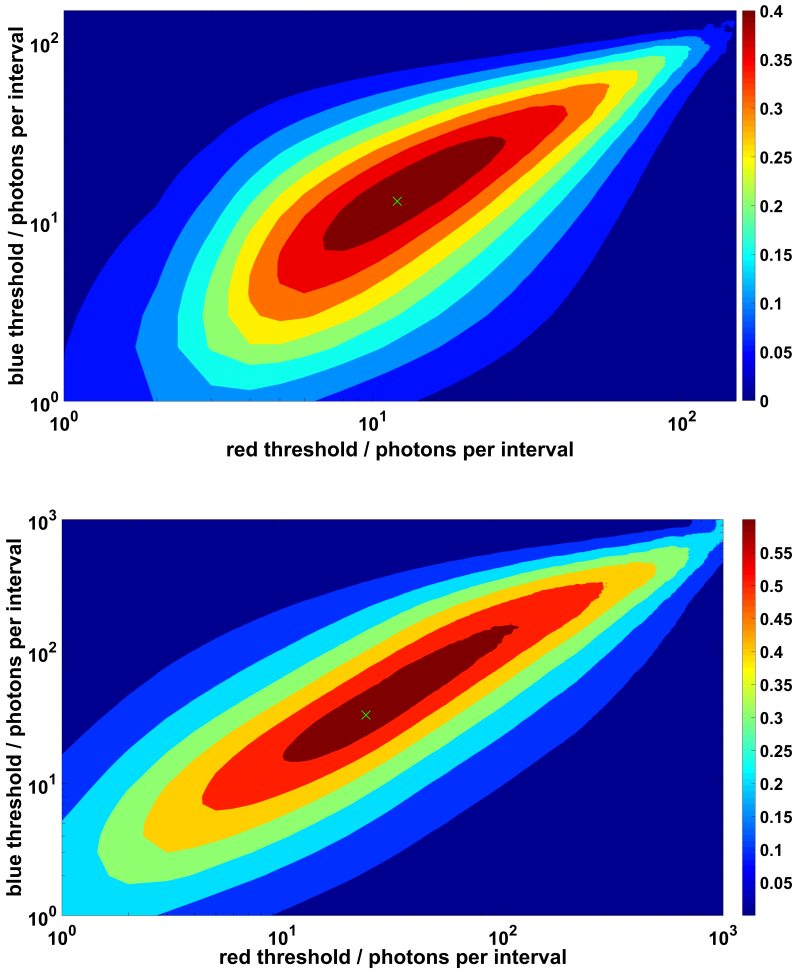

Figure B.5: Association quotient (see Eq. 5.6) of conventional two-color coincidence detection plotted in color code depending on the brightness thresholds of the blue and red channel. Maximum value is marked with green cross. Data shown for dsDNA (Alexa 488/Alexa 647) in upper panel and nano-bead reference in lower panel. Adopted from [140].

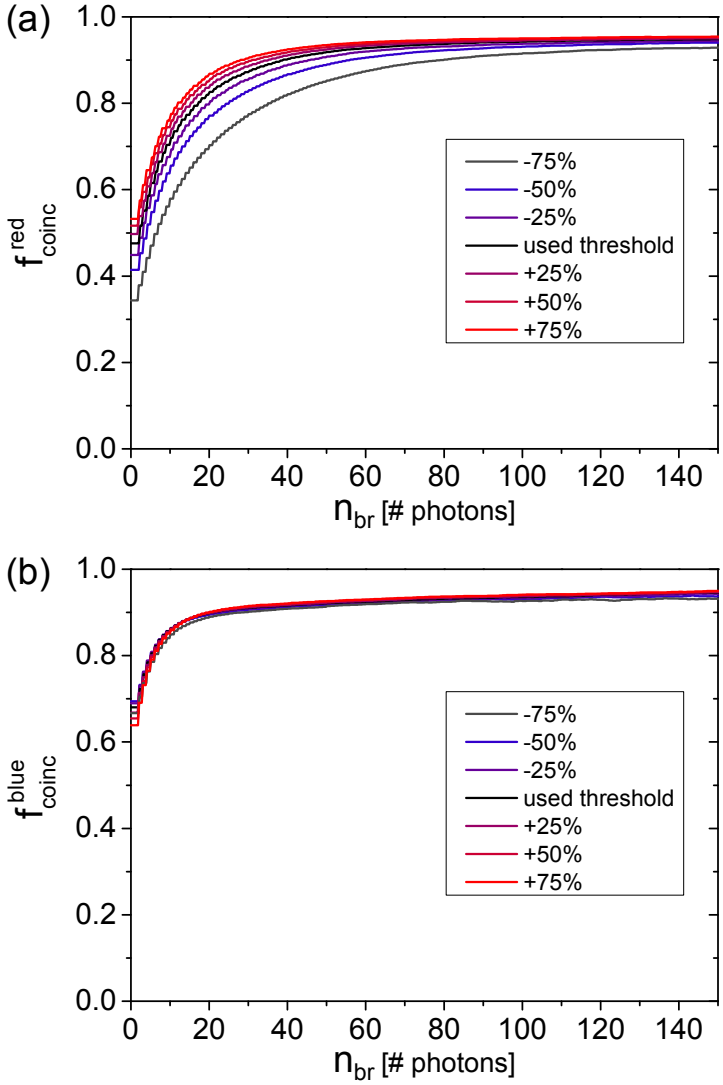

Figure B.6: Fraction of coincident (a) red and (b) blue bursts as a function of brightness threshold for dsDNA reference (Alexa 488/Atto 647N). The IPL burst threshold is varied simultaneously for both channels from the used threshold (black lines) by the relative changes given in the legend. Note, that smaller IPL thresholds correspond to bursts with higher photon counts. The red coincidence fraction shows generally a stronger dependency on the IPL thresholds, however, all coincidence fractions saturate at approximately the same value. Adopted from [140].

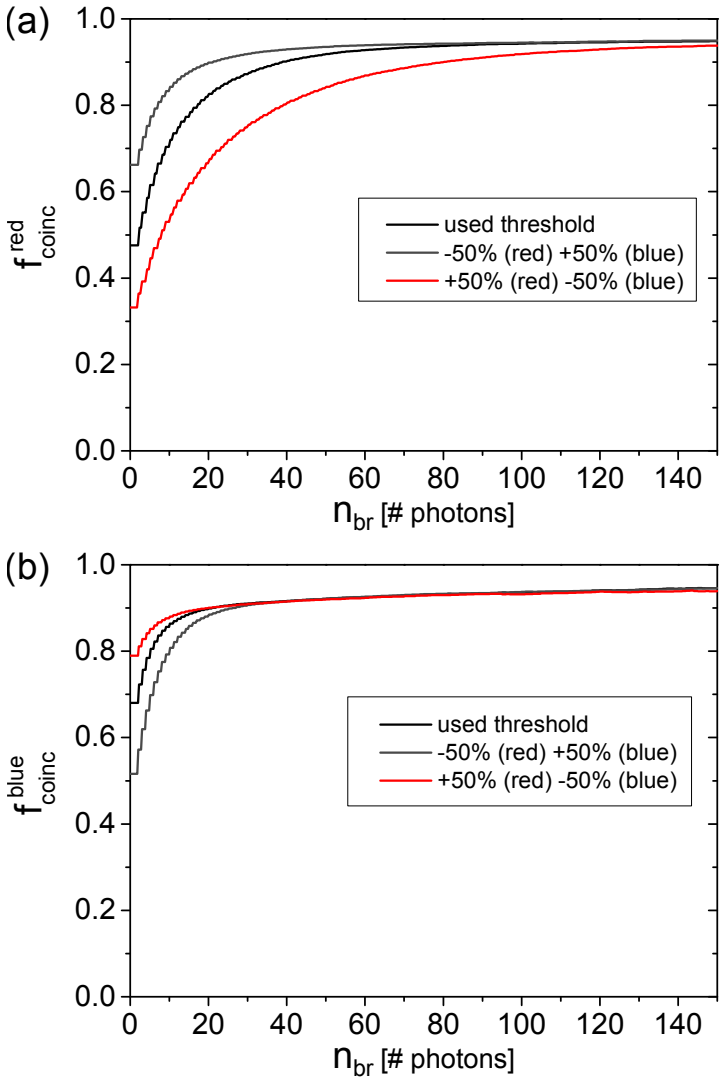

Figure B.7: Fraction of coincident (a) red and (b) blue bursts as a function of brightness threshold for dsDNA reference (Alexa 488/Atto 647N). The IPL burst threshold is varied from the used threshold (black lines) conversely for both channels by a relative change of ±50 %. The red and blue coincidence fractions show an opposite dependency on the threshold combinations because a reduction of the IPL thresholds leads to a preselection of bright bursts in the respective channel and, hence, to higher coincidence fraction and a saturation at smaller brightness thresholds. Adopted from [140].

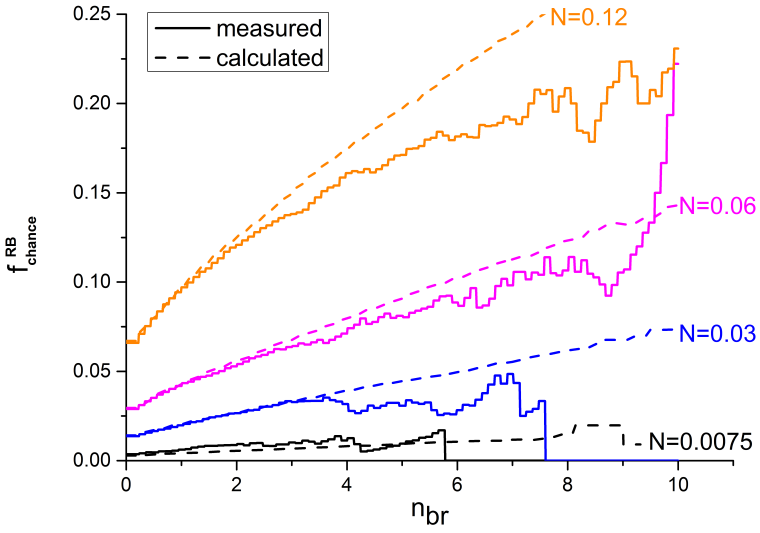

Figure B.8: Chance coincidences of freely diffusing Alexa 488 (B) and Alexa 647 (R) dyes. Concentration of dyes is adjusted to achieve same number of molecules in red and blue detection volume ($N_R = N_B = N/2$). BTCCD analysis (solid line) is compared to predicted fraction of red chance coincidence according to Equation 5.17.

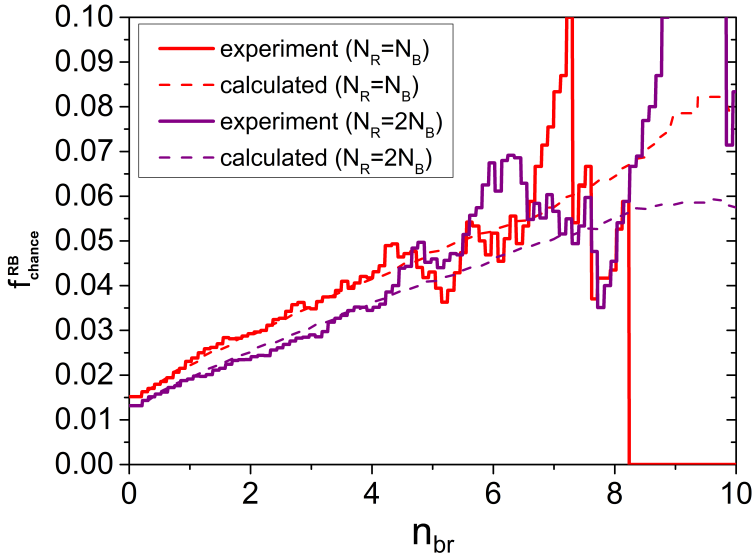

Figure B.9: Chance coincidences of red bursts obtained for freely diffusing Alexa 488 (B) and Alexa 647 (R) dyes with equal N (red lines) or twofold N of Alexa 647 (purple lines) as a function of red brightness threshold. BTCCD analysis (solid lines) is compared to predicted fraction of chance coincidence (dashed lines). Coincidences are almost equal because the red chance coincidences depend only on the number of blue dye N_B.

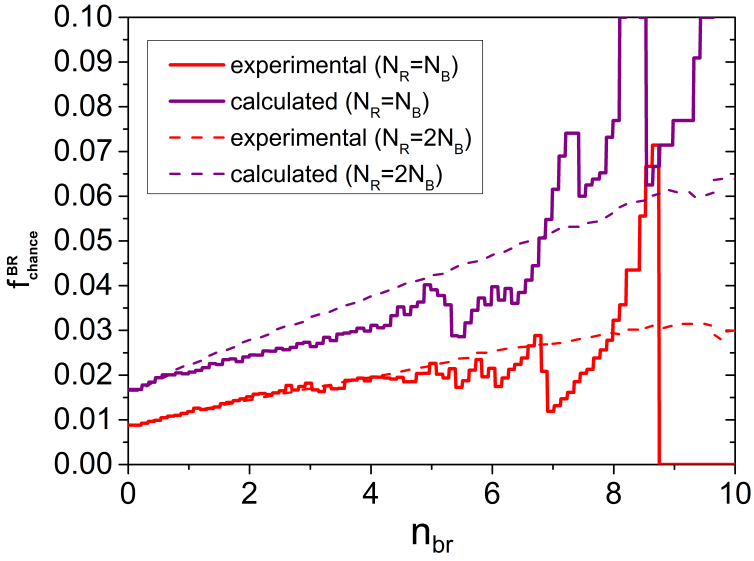

Figure B.10: Chance coincidences of blue bursts obtained for freely diffusing Alexa 488 (B) and Alexa 647 (R) dyes with equal N (red lines) or twofold N of Alexa 647 (purple lines) as a function of blue brightness threshold. BTCCD analysis (solid lines) is compared to predicted fraction of chance coincidence (dashed lines). Coincidences of twofold Alexa 647 are approximately twice as high according to Equation 5.18.

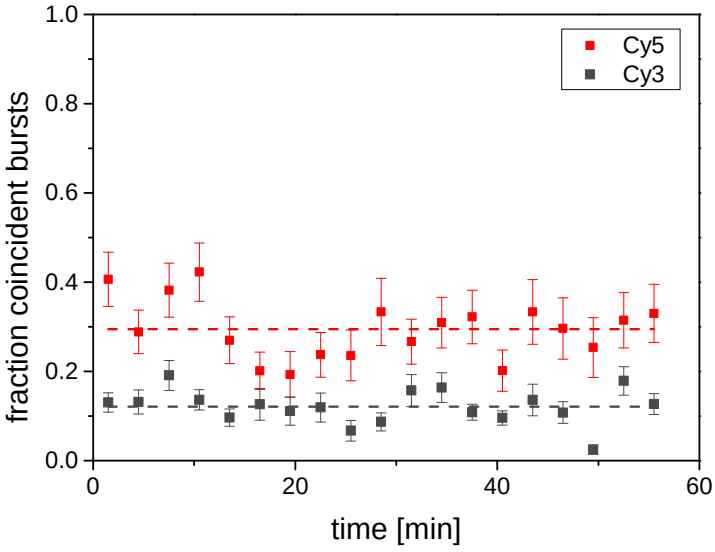

Figure B.11: Stability of 70S ribosomes at low concentrations (~ pM) is investigated with Cy5 labeled 50S subunits and Cy3 labeled 30S subunits. Consecutive three minutes coincidence measurements are performed over one hour. Coincidence fractions are stable for one hour (fluctuating around dashed lines) and, hence, no dissociation of 70S complex due to the low concentration is occurring during that time window.

Acknowledgment

Zunächst möchte ich meinem Doktorvater Prof. Jörg Fitter für die Möglichkeit danken, meine Promotion in seiner Arbeitsgruppe durchführen zu können. Ich habe es auch ihm zu verdanken, dass ich mein Interesse für die Biophysik entdeckt habe als ich zufällig beim Blättern durch die Mastervorlesungen auf seine Vorlesung gestoßen bin. Prof. Fitters Faszination an biologischen Fragestellungen ist immer wieder ansteckend und er versteht es die Biologie “physikergerecht" zu erklären. Ich möchte mich auch für die Arbeitsatmosphäre in der Gruppe bedanken, die geprägt war von gegenseitiger Wertschätzung und Vertrauen.

Ich danke außerdem ganz herzlich Prof. Dominik Wöll für die Bereitschaft meine Dissertation als Zweitgutachter zu betreuen.

Des weiteren danke ich der gesamten AG Biophysik für die Unterstützung über die Jahre. Besonders möchte ich mich bei Dr. Daryan Kempe bedanken, der mich schon während der Masterarbeit in alle experimentellen Techniken eingearbeitet hat und während meiner Promotion immer für hilfreiche Diskussionen bereitstand. Vielen Dank an Julia Walter für das Aufrechterhalten eines benutzbaren Labors. Further I would like to thank all former and actual PhD student in the biophysics group: Dr. Alyazan Albargash, Farzaneh Vaghefikia and Olessya Yuknovets. I enjoyed the discussion with you, also out of the scientific context.
Ich möchte nicht vergessen, mich bei allen Bachelor- und Masterstudenten unserer Arbeitsgruppe zu bedanken.

I would like to thank all (former) employes of ICS-5 for their constant support. Dr. Matteo Gabba supported especially at the beginning of my PhD study and arranged the collaboration with the University of Groningen. Dr. Michele Cerminara helped me with the confocal setup at ICS-5. Special thanks go to Dr. Alexandros Katranidis, Dr. Noémie Kempf, Dr. Cristina Remes, Dr. Antonie Schöne and Ilona Ritter for their support and efforts in producing biological samples.

I would like to thank my collaborators Prof. Martina Pohl, Dr. Victoria Steffen, and Dr. Julia Otten at IBG-1 (Forschungszentrum Jülich) and Dr. Arnold Boersma (University of Groningen) for supporting me with their biosensors and for lots of insightful discussions.

I kindly acknowledge financial support by the International Helmholtz Research School of Biophysics and Soft Matter “BioSoft" and thank Dr. Thorsten Auth for his efforts in the organization of the school.

Finally, I thank my family for supporting me and having a lot of patience.

Band / Volume 212
First-principles study of collective spin excitations in noncollinear magnets
F.J. dos Santos (2020), 270 pp
ISBN: 978-3-95806-459-1

Band / Volume 213
Direct measurement of anisotropic resistivity in thin films using a 4-probe STM
T. Flatten (2020), viii, 129 pp
ISBN: 978-3-95806-460-7

Band / Volume 214
The guided self-assembly of magnetic nanoparticles into two- and three- dimensional nanostructures using patterned substrates
W. Ji (2020), VI, 140 pp
ISBN: 978-3-95806-462-1

Band / Volume 215
Molecular layer deposition and protein interface patterning for guided cell growth
M. Glass (2020), iv, 81 pp
ISBN: 978-3-95806-463-8

Band / Volume 216
Development of a surface acoustic wave sensor for in situ detection of molecules
D. Finck (2020), 63 pp
ISBN: 978-3-95806-464-5

Band / Volume 217
Detection and Statistical Evaluation of Spike Patterns in Parallel Electrophysiological Recordings
P. Quaglio (2020), 128 pp
ISBN: 978-3-95806-468-3

Band / Volume 218
Automatic Analysis of Cortical Areas in Whole Brain Histological Sections using Convolutional Neural Networks
H. Spitzer (2020), xii, 162 pp
ISBN: 978-3-95806-469-0

Band / Volume 219
Postnatale Ontogenesestudie (Altersstudie) hinsichtlich der Zyto- und Rezeptorarchitektonik im visuellen Kortex bei der grünen Meerkatze
D. Stibane (2020), 135 pp
ISBN: 978-3-95806-473-7

Band / Volume 220
Inspection Games over Time: Fundamental Models and Approaches
R. Avenhaus und T. Krieger (2020), VIII, 455 pp
ISBN: 978-3-95806-475-1

Band / Volume 221
High spatial resolution and three-dimensional measurement of charge density and electric field in nanoscale materials using off-axis electron holography
F. Zheng (2020), xix, 182 pp
ISBN: 978-3-95806-476-8

Band / Volume 222
Tools and Workflows for Data & Metadata Management of Complex Experiments
Building a Foundation for Reproducible & Collaborative Analysis in the Neurosciences
J. Sprenger (2020), X, 168 pp
ISBN: 978-3-95806-478-2

Band / Volume 223
Engineering of *Corynebacterium glutamicum* towards increased malonyl-CoA availability for polyketide synthesis
L. Milke (2020), IX, 117 pp
ISBN: 978-3-95806-480-5

Band / Volume 224
Morphology and electronic structure of graphene supported by metallic thin films
M. Jugovac (2020), xi, 151 pp
ISBN: 978-3-95806-498-0

Band / Volume 225
Single-Molecule Characterization of FRET-based Biosensors and Development of Two-Color Coincidence Detection
H. Höfig (2020), XVIII, 160 pp
ISBN: 978-3-95806-502-4

Weitere ***Schriften des Verlags im Forschungszentrum Jülich*** unter
http://wwwzb1.fz-juelich.de/verlagextern1/index.asp

Schlüsseltechnologien / Key Technologies
Band / Volume 225
ISBN 978-3-95806-502-4

Mitglied der Helmholtz-Gemeinschaft

JÜLICH
Forschungszentrum